8-2016

Two-particle correlation studies in heavy ion collisions at the Large Hadron Collider

Lingshan Xu
Purdue University

Graduate School Form
30 Updated 12/26/2015

PURDUE UNIVERSITY
GRADUATE SCHOOL
Thesis/Dissertation Acceptance

This is to certify that the thesis/dissertation prepared

By Lingshan Xu

Entitled

TWO-PARTICLE CORRELATION STUDIES IN HEAVY ION COLLISIONS AT THE LARGE HADRON COLLIDER

For the degree of Doctor of Philosophy

Is approved by the final examining committee:

Fuqiang Wang Chair	Rafael F. Lang
Denes Molnar	Wei Xie

To the best of my knowledge and as understood by the student in the Thesis/Dissertation Agreement, Publication Delay, and Certification Disclaimer (Graduate School Form 32), this thesis/dissertation adheres to the provisions of Purdue University's "Policy of Integrity in Research" and the use of copyright material.

Approved by Major Professor(s): Fuqiang Wang

Approved by: John P. Finley 7/7/2016

Head of the Departmental Graduate Program Date

TWO-PARTICLE CORRELATION STUDIES IN HEAVY ION COLLISIONS AT THE LARGE HADRON COLLIDER

A Dissertation

Submitted to the Faculty

of

Purdue University

by

Lingshan Xu

In Partial Fulfillment of the

Requirements for the Degree

of

Doctor of Philosophy

August 2016

Purdue University

West Lafayette, Indiana

ACKNOWLEDGMENTS

Throughout my PhD journey at Purdue, I have been helped and blessed by many individuls, totaling more than can be listed here.

First and foremost, I would like to thank my major advisor Fuqiang Wang, who always encourged me in my research, inspired me with his ideas, and taught me more than the research methodology. This thesis would not be possible without the help and guidance from him. I would like to express my appreciation towards my commitee members, Prof. Wei Xie, Prof. Denes Molnar and Prof. Rafael Lang for their help to my thesis work. Also I would like to thank Prof. Andrew Hirsch, Prof. Rolf Scharenberg and Prof. Brijish Srivastava, for their advice and discussions during group meetings.

I had a great time with my fellow graduate students in heavy ion group; we helped each other, especially during difficult times. Josh Konzer and Quan Wang devoted their time to answer my questions when I just joined the group. Kurt Jung and I made many trips to CERN and overcame some difficulties together. For two years Kun Jiang and I shared the office and encouraged each other towards the graduation. Liang He, Jian Sun and David Garand always had time for me to chat and discuss. In addition, I would like to thank other graduate students, Tyler Browning, Liang He, Xin Li, Michael Skoby and Deke Sun. Last but not least, I would like to express my special appreciation to Li Yi for the time we shared together, both during the research and outside the research.

I would like to thank my CMS collaborators for their help. Wei Li, Shengquan Tuo and Dragos Velicanu taught me a lot when I just joined CMS. I also obtained a lot help to my analysis work from Julia Velkovska, Steve Sanders, Yen-Jie Lee and many other collaborators.

I also would like to thank my friend Fa Wang for her accompany during the time we spent together preparing for our gradution.

Finally I would like to thank my parents and my boyfriend Siyi Shao for their understanding and support through all these years.

TABLE OF CONTENTS

Page

LIST OF TABLES vi

LIST OF FIGURES vii

SYMBOLS xvi

ABBREVIATIONS xvii

ABSTRACT xviii

1 Introduction 1
- 1.1 Fundamental forces and particles 1
- 1.2 Quark model and Strong interaction 2
- 1.3 QCD under extreme condition 3
- 1.4 Heavy ion collisions and Quark Gluon Plasma 5
  - 1.4.1 Jet as a probe 8
  - 1.4.2 Anisotropic flow 9
- 1.5 Small collision system 12
- 1.6 Two particle $\Delta\eta$-$\Delta\phi$ correlation method 14
  - 1.6.1 Two particle correlation technique 14
  - 1.6.2 Azimuthal anisotropy from dihadron correlation 15
  - 1.6.3 Long range near-side ridge analysis 16
  - 1.6.4 Away side jet measurement 21

2 Experiemnt setup 25
- 2.1 Large Hadron Collider (LHC) 25
- 2.2 Compact Muon Solenoid 26
  - 2.2.1 Inner Tracking System 28
  - 2.2.2 Calorimeters 30
  - 2.2.3 Data Sample 31

3 Two-particle correlation analysis 33
- 3.1 Event selection 33
  - 3.1.1 L1 and HLT trigger system 33
  - 3.1.2 Offline event cuts 34
- 3.2 Track Selection and Multiplicity definition 34
  - 3.2.1 Track Quality cuts 34
  - 3.2.2 Multiplicity Definition 35
  - 3.2.3 Tracking correction 37

Page

3.3 Pseudorapidity dependence of azimuthal anisotropy 38
3.3.1 ZYAM normalization 38
3.3.2 Fit the near-side jet and ridge 46
3.3.3 η-dependence of the azimuthal anisotropy 48
3.4 Systematics and Cross Checks 51
3.4.1 Systematics on vertex position dependence 53
3.4.2 High Multiplicity HLT trigger bias 57
3.4.3 Systematics on track quality cuts 60
3.4.4 Systematic study pileup effects 65
3.4.5 Systematic uncertainties from near-side jet ratio 68
3.4.6 Study of beam direction systematics 74
3.4.7 Cross check of efficiency correction of trigger particles 77
3.4.8 Cross check of V_2 calculation method 77
3.4.9 Comparison to cumulant method 78
3.4.10 Closure test with HIJING 79
3.4.11 Cross check of ZYAM method 81
3.5 Results 85
3.6 Conclusion 89

4 Away side jet correlation shape analysis 91
4.1 Data sample and event selection 91
4.2 Analysis technique 92
4.2.1 Centrality definition 92
4.2.2 P_{x} event selection method 93
4.2.3 Corrections 94
4.2.4 Two-particle correlation function and away-side jet extraction 95
4.3 systematic study and cross check 98
4.3.1 P_{x} selection systematic study 99
4.3.2 Track quality cuts systematic study 99
4.3.3 Jet fit method systematic study 100
4.4 Results 101
4.5 Discussion and future direction 102

5 Summary 105

LIST OF REFERENCES 106

VITA 112

LIST OF TABLES

Table Page

3.1 Summary of each HLT trigger used for each $N_{trk}^{offline}$ range in pPb collisions. 35

3.2 Summary of fit parameters for low- and high-$N_{trk}^{offline}$ ranges in pPb collisions. 49

3.3 Summary of relative systematic uncertainties on second and third harmonics azimuthal anisotropy in pPb collisions at $\sqrt{s_{NN}}$=5.02 TeV. "low-mult sub" stands for low-multiplicity subtracted results, while "no sub" stands for no subtraction results. 52

3.4 Jet ratio systematic study 70

3.5 ZYAM systematic study 70

3.6 Comparison of fitted parameters between those for default background (ZYAM) and background built from $\Delta\eta_{rand}$ in pPb collisions (labeled as "$\Delta\eta_{rand}$ background"). 83

4.1 Summary of systematic uncertainties of away-side jet width in PbPb collisions at $\sqrt{s_{NN}}$=2.76 TeV. 99

LIST OF FIGURES

Figure Page

1.1 A schematic of quark generations and force carriers. 2

1.2 A schematic phase diagram. The solid lines show the phase boundaries for the indicated phases. The solid circle depicts the critical point. Possible trajectories for systems created in the QGP phase at different accelerator facilities are also shown. [8] 4

1.3 A sketch of space-time evolution. [14] 7

1.4 Measurements of the nuclear modification factor R_{AA} in central heavy-ion collisions at three different center-of-mass energies, as a function of p_{T}, for neutral pions (π^0), and charged hadrons ($h^{\pm}$), compared to several theoretical predictions. [19] 9

1.5 Initial geometry of heavy ion collisions. The smooth initial geometry (a) and the initial geometry with fluctuations (b). 10

1.6 Measurements of the nuclear modification factor R_{AA} in pPb collisions at $\sqrt{s} = 5.02TeV$ and compared to central (0-5%) and peripheral PbPb (70-80%) collisions at $\sqrt{s} = 2.76TeV$. [34] 13

1.7 The 2D two-particle correlation functions for (a) 2.76 TeV PbPb and (b) 5.02 TeV pPb for pairs of charged particles with $1 < p_T < 3$ GeV/c within $220 \leq N_{trk}^{offline} 260$ multiplicity bin. [35] 17

1.8 Top: The $v_2\{2, |\Delta\eta| > 2\}$ (circles) and $v_2\{4\}$ (squares) values as a function of $N_{trk}^{offline}$ for 2.76TeV PbPb (left) and 5.02 TeV pPb (right) for pairs of charged particles with $1 < p_T < 3$ GeV/c. Bottom: upper limits on the relative v_2 fluctuation estimated from $v_2\{2\}$ and $v_2\{4\}$ in 2.76TeV PbPb (left) and 5.02 TeV pPb (right). [35] 18

1.9 The $v_3\{2, |\Delta\eta| > 2\}$ values as a function of $N_{trk}^{offline}$ for 2.76TeV PbPb (left) and 5.02 TeV pPb (right) for pairs of charged particles with $1 < p_T <$ 3 GeV/c. d $v_2\{4\}$ in 2.76TeV PbPb (left) and 5.02 TeV pPb (right). [35] 19

1.10 Top: The $v_2\{2, |\Delta\eta| > 2\}$ (circles) and $v_2\{4\}$ (squares) values as a function of $N_{trk}^{offline}$ for 2.76TeV PbPb (left) and 5.02 TeV pPb (right) for pairs of charged particles with $1 < p_T < 3$ GeV/c. Bottom: upper limits on the relative v_2 fluctuation estimated from $v_2\{2\}$ and $v_2\{4\}$ in 2.76TeV PbPb (left) and 5.02 TeV pPb (right). [35] 20

Figure Page

1.11 The $v_3\{2, |\Delta\eta| > 2\}$ values as a function of $N_{trk}^{offline}$ for 2.76TeV PbPb (left) and 5.02 TeV pPb (right) for pairs of charged particles with $1 < p_T < 3$ GeV/c. d $v_2\{4\}$ in 2.76TeV PbPb (left) and 5.02 TeV pPb (right). [35] 20

1.12 A dijet event detected by CMS detector. [58] 21

1.13 Two particle angular correlation from pp and AuAu collision events from STAR data and the Hadron String Dynamic(HSD) transport model calculation. Associated particles are $2 < p_{\mathrm{T}} < 4$ GeV/c and trigger particles are $p_{\mathrm{T}} > 4$ GeV/c. [63] 22

1.14 Upper: Azimuthal distributions of associated particles for trigger particles in-plane(squares) and out-of-plane(triangles) for AuAu collisions at centrality 20-60%. Open symbols are reflections of solid symbols around $\Delta\phi = 0$ and $\Delta\phi = \pi$. Elliptic flow contribution is shown by dashed lines. Lower: Distribution after subtracting elliptic flow, and the corresponding measurement in pp collisions. [66] 24

2.1 Sketch of LHC complex. The pre-accelerator, the LHC storage ring and the 4 main experiments are shown. [67] 26

2.2 CMS detector cross section. From the innermost: pixel tracker, silicon strip tracker, electromagnetic (ECAL) and hadron calorimeter (HCAL), the superconducting solenoid and the muon system. [70] 27

2.3 Schematic of longitudinal view of CMS detector. The dashed line indicates the limitation of different subdetectors acceptance. [71] 28

2.4 Schematic of the CMS silicon tracker cross section. Each line represents a detector module. Double lines indicates back-to-back modules which deliver stero hits. [72] 29

2.5 Schematic of the cross section of CMS detector and how different species of particles are absorbed in the detector. 31

3.1 Projection of the tracking efficiency as a function of N_{TP} (the total number of simulated tracks in each event) for $0.1 < p_T < 2.0$ GeV/c (blue) and $2.0 < p_T < 6.0$ (red) with $|\eta| < 1.2$. [35] 36

3.2 Tracking efficiency 2D plot vs η and p_T (left) and the projection on η. The efficiency is obtained from PYTHIA (tune Z2) [73] pp simulation. . . . 37

3.3 Charged particle distribution (within $1 < p_T < 3$ GeV/c) before and after efficiency correction for 5.02 TeV pPb collisions. Two multiplicity bins are shown: $N_{trk}^{offline} < 35$ (left) and $120 \leq noff < 150$ (right). 37

Figure Page

3.4 2D correlated yield with $2.0 < \eta_{trig} < 2.4$ (left panel) and $-2.4 < \eta_{trig} < -2.0$ (right panel) for low-multiplicity $2 \leq N_{trk}^{offline} < 20$ (upper panels) and high-multiplicity $220 \leq N_{trk}^{offline} < 260$ (lower panels) pPb collisions at 5.02 TeV. The p_{T} ranges are $0.3 < p_{\mathrm{T}}^{\mathrm{trig}}, p_{\mathrm{T}}^{\mathrm{assoc}} < 3$ GeV/c. The data are efficiency corrected. 39

3.5 $\Delta\phi$ projection of each $\Delta\eta$ bin of 2D correlated yield with $-2.4 < \eta_{trig} < -2.0$ for high-multiplicity $N_{trk}^{offline} < 20$ pPb collisions at 5.02 TeV. The p_{T} ranges are $0.3 < p_{\mathrm{T}}^{\mathrm{trig}}, p_{\mathrm{T}}^{\mathrm{assoc}} < 3$ GeV/c. The data are efficiency corrected. 40

3.6 $\Delta\phi$ projection of each $\Delta\eta$ bin of 2D correlated yield with $2.0 < \eta_{trig} < 2.4$ for high-multiplicity $N_{trk}^{offline} < 20$ pPb collisions at 5.02 TeV. The p_{T} ranges are $0.3 < p_{\mathrm{T}}^{\mathrm{trig}}, p_{\mathrm{T}}^{\mathrm{assoc}} < 3$ GeV/c. The data are efficiency corrected. 41

3.7 $\Delta\phi$ projection of each $\Delta\eta$ bin of 2D correlated yield with $-2.4 < \eta_{trig} < -2.0$ for high-multiplicity $220 \leq N_{trk}^{offline} < 260$ pPb collisions at 5.02 TeV. The p_{T} ranges are $0.3 < p_{\mathrm{T}}^{\mathrm{trig}}, p_{\mathrm{T}}^{\mathrm{assoc}} < 3$ GeV/c. The data are efficiency corrected. 42

3.8 $\Delta\phi$ projection of each $\Delta\eta$ bin of 2D correlated yield with $2.0 < \eta_{trig} < 2.4$ for high-multiplicity $220 \leq N_{trk}^{offline} < 260$ pPb collisions at 5.02 TeV. The p_{T} ranges are $0.3 < p_{\mathrm{T}}^{\mathrm{trig}}, p_{\mathrm{T}}^{\mathrm{assoc}} < 3$ GeV/c. The data are efficiency corrected. 43

3.9 Correlated yields for different $|\Delta\phi|$ ranges of correlated yields for Pb-side ($-2.4 < \eta_{trig} < -2.0$, left) and p-side ($2.0 < \eta_{trig} < 2.4$, right) in pPb collisions at 5.02 TeV. The p_{T} ranges are $0.3 < p_{\mathrm{T}}^{\mathrm{trig}}, p_{\mathrm{T}}^{\mathrm{assoc}} < 3.0$ GeV/c. Upper panels are low-multiplicity collisions and lower panels are high-multiplicity collisions. 44

3.10 Distributions of associated yields after ZYAM subtraction for both low-multiplicity ($2 \leq N_{trk}^{offline} < 20$, red points) and high-multiplicity ($220 \leq N_{trk}^{offline} < 260$, blue points), pPb collisions at 5.02 TeV. The results for Pb-side (left panels) and p-side (right panels) trigger particles are both shown; two $\Delta\eta$ bins are shown: small $\Delta\eta$ in the upper panels and large $\Delta\eta$ in the lower panels. The trigger and associated particle p_{T} ranges are both $0.3 < p_{\mathrm{T}} < 3$ GeV/c. 45

Figure Page

3.11 Near-side correlated yield after ZYAM subtraction for low-multiplicity $2 \leq N_{trk}^{offline} < 20$ (upper panels) and high-multiplicity $220 \leq N_{trk}^{offline} < 260$ (lower panels). The correlated yields are fit by Eq.(3.3) for low-multiplicity data and by Eq.(3.2) for high-multiplicity data. Data are 5.02 TeV pPb collisions for pairs of charged particles with $0.3 < p_{\mathrm{T}}^{\mathrm{trig}}, p_{\mathrm{T}}^{\mathrm{assoc}} < 3$ GeV/c, and trigger particle η windows of Pb-side ($-2.4 < \eta_{trig} < -2.0$, left) and p-side ($2.0 < \eta_{trig} < 2.4$, right). 47

3.12 Top: Comparison of V_2 in pPb at 5.02 TeV for $3 < |z_{vtx}| < 7.5$ cm and $|z_{vtx}| < 3$ cm vertex range. High- and low- multiplicity events are from the same vertex range, respectively. Left is the Pb-side trigger, right is p-side trigger. V_n is compared for both before and after low multiplicity subtraction. Trigger and associated particle p_{T} are both $0.3 < p_{\mathrm{T}} < 3$ GeV/c. High multiplicity collisions are defined by $220 \leq N_{trk}^{offline} < 260$ and low multiplicity collisions by $2 \leq N_{trk}^{offline} < 20$. Second row: The ratio of $3 < |z_{vtx}| < 7.5$ cm to $|z_{vtx}| < 3$ cm result, before low multiplicity subtraction. Bottom two rows: $(Ratio - 1)/E_{stat}$ distribution of low multiplicity subtraction and no subtraction. 55

3.13 Top: Comparison of V_3 in pPb at 5.02 TeV for $3 < |z_{vtx}| < 7.5$ cm and $|z_{vtx}| < 3$ cm vertex range. High- and low- multiplicity events are from the same vertex range, respectively. Left is the Pb-side trigger, right is p-side trigger. V_n is compared for both before and after low multiplicity subtraction. Trigger and associated particle p_{T} are both $0.3 < p_{\mathrm{T}} < 3$ GeV/c. High multiplicity collisions are defined by $220 \leq N_{trk}^{offline} < 260$ and low multiplicity collisions by $2 \leq N_{trk}^{offline} < 20$. Second row: The ratio of $3 < |z_{vtx}| < 7.5$ cm to $|z_{vtx}| < 3$ cm result, before low multiplicity subtraction. Bottom two rows: $(Ratio - 1)/E_{stat}$ distribution of low multiplicity subtraction and no subtraction. 56

3.16 Top: Comparison V_2 in pPb collision at 5.02 TeV for loose cuts and tight cuts with low multiplicity subtraction. Left is the Pb-side trigger, right is p-side trigger. V_2 is compared for both before and after low multiplicity subtraction. Trigger and associated particle p_{T} values are both $0.3 < p_{\mathrm{T}} < 3$ GeV/c. High multiplicity collisions are defined by $220 \leq N_{trk}^{offline} < 260$ and low multiplicity collisions by $2 \leq N_{trk}^{offline} < 20$. Bottom: Ratios of loose cuts to default and tight cuts to default, with low multiplicity subtraction. 61

Figure Page

3.17 Top: Comparison V_2 in pPb collision at 5.02 TeV for loose cuts and tight cuts without low multiplicity subtraction. Left is the Pb-side trigger, right is p-side trigger. V_2 is compared for both before and after low multiplicity subtraction. Trigger and associated particle p_{T} values are both $0.3 < p_{\mathrm{T}} < 3$ GeV/c. High multiplicity collisions are defined by $220 \leq N_{trk}^{offline} < 260$. Bottom: Ratios of loose cuts to default and tight cuts to default, without low multiplicity subtraction. 62

3.18 Top: Comparison of V_3 in pPb collision at 5.02 TeV for loose cuts and tight cuts with low multiplicity subtraction. Left is the Pb-side trigger, right is p-side trigger. V_2 is compared for both before and after low multiplicity subtraction. Trigger and associated particle p_{T} values are both $0.3 < p_{\mathrm{T}} < 3$ GeV/c. High multiplicity collisions are defined by $220 \leq N_{trk}^{offline} < 260$ and low multiplicity collisions by $2 \leq N_{trk}^{offline} < 20$. Bottom: Ratios of loose cuts to default and tight cuts to default, with low multiplicity subtraction. 63

3.19 Top: Comparison of V_3 in pPb collision at 5.02 TeV for loose cuts and tight cuts without low multiplicity subtraction. Left is the Pb-side trigger, right is p-side trigger. V_2 is compared for both before and after low multiplicity subtraction. Trigger and associated particle p_{T} values are both $0.3 < p_{\mathrm{T}} < 3$ GeV/c. High multiplicity collisions are defined by $220 \leq N_{trk}^{offline} < 260$. Bottom: Ratios of loose cuts to default and tight cuts to default, without low multiplicity subtraction. 64

3.21 Top: Comparison of V_3 in pPb collision at 5.02 TeV for 1 events and multi-vertex events. Left is the Pb-side trigger, right is p-side trigger. V_n is compared for both before and after low multiplicity subtraction. Trigger and associated particle p_{T} are both $0.3 < p_{\mathrm{T}} < 3$ GeV/c. High multiplicity collisions are defined by $220 \leq N_{trk}^{offline} < 260$ and low multiplicity collisions by $2 \leq N_{trk}^{offline} < 20$. Second row: The ratio of V_3 of single-vertex events to V_3 of multiple-vertex events, without low multiplicity subtraction. Bottom: $(Ratio-1)/E_{stat}$ distribution of low multiplicity subtraction and no subtraction. 67

3.22 Gaussian plus linear function scaled ZYAM fit functions of near-side jet plus ridge with the fit parameters on the plots. 68

3.23 Fit p-side and Pb-side together with generalized Gaussian plus linear function scaled ZYAM, with the fit parameters on the plots. 69

Figure Page

3.24 Top: Comparison of V_2 in pPb collisions without low multiplicity subtraction at 5.02 TeV extracted using low and high value of jet ratio (α) systematic error. *Left* is the Pb-side trigger, *right* is p-side trigger. V_n is compared for both before and after low multiplicity subtraction. Trigger and associated particle p_{T} are both $0.3 < p_{\mathrm{T}} < 3$ GeV/c. High multiplicity collisions are defined by $220 \leq N_{trk}^{offline} < 260$ and low multiplicity collisions by $2 \leq N_{trk}^{offline} < 20$. Bottom: The ratio of lowest jet ratio and highest jet ratio result to the default, with low multiplicity subtraction. 72

3.25 Top: Comparison of V_3 in pPb collisions without low multiplicity subtraction at 5.02 TeV extracted using low and high value of jet ratio (α) systematic error. *Left* is the Pb-side trigger, *right* is p-side trigger. V_n is compared for both before and after low multiplicity subtraction. Trigger and associated particle p_{T} are both $0.3 < p_{\mathrm{T}} < 3$ GeV/c. High multiplicity collisions are defined by $220 \leq N_{trk}^{offline} < 260$ and low multiplicity collisions by $2 \leq N_{trk}^{offline} < 20$. Bottom: The ratio of lowest jet ratio and highest jet ratio result to the default, with low multiplicity subtraction. 73

3.26 Top: Comparison V_2 of pPb default direction collisions events and reversed direction events at 5.02 TeV. V_2 result before low multiplicity subtraction (blue) and after subtraction (red) are shown with both Pb-side trigger (left) and p-side trigger(Right). Trigger and associated particle p_{T} are both $0.3 < p_{\mathrm{T}} < 3$ GeV/c. High multiplicity collisions are defined by $220 \leq N_{trk}^{offline} < 260$ and low multiplicity collisions by $2 \leq N_{trk}^{offline} < 20$. Second row: V_2 Ratio of reversed beam direction to the default direction. Bottom: $(Ratio-1)/E_{stat}$ distribution of low multiplicity subtraction and no subtraction. 75

3.27 Top: Comparison V_3 of pPb default direction collisions events and reversed direction events at 5.02 TeV. V_2 result before low multiplicity subtraction (Blue) and after subtraction (Red) are shown with both Pb-side trigger(Left) and p-side trigger(Right). Trigger and associated particle p_{T} are both $0.3 < p_{\mathrm{T}} < 3$ GeV/c. High multiplicity collisions are defined by $220 \leq N_{trk}^{offline} < 260$ and low multiplicity collisions by $2 \leq N_{trk}^{offline} < 20$. subtraction. Second row: V_3 Ratio of reversed beam direction to the default direction. Bottom: $(Ratio-1)/E_{stat}$ distribution of low multiplicity subtraction and no subtraction. 76

3.28 Comparison V_2 in pPb collisions at 5.02 TeV for trigger efficiency corrected events (blue) and not corrected (red) events. Trigger and associated particle p_{T} are both $0.3 < p_{\mathrm{T}} < 3$ GeV/c. High multiplicity collisions are defined by $220 \leq N_{trk}^{offline} < 260$. 77

Figure Page

3.29 Comparison of V_2 results obtained by two methods as labeled, for p-side trigger (left) and Pb-side (right). Trigger and associated particle $p_{\rm T}$ are both $0.3 < p_{\rm T} < 3$ GeV/c. High multiplicity collisions are defined by $220 \leq N_{trk}^{offline} < 260$ and low multiplicity collisions by $2 \leq N_{trk}^{offline} < 20$. 78

3.30 (Left)Comparison of η dependence v_2 results obtained by cumulant method and two-particle correlation method as labeled. (Right) Ratio of cumulant method v_2 to two-particle correlation method single particle v_2. Trigger and associated particle $p_{\rm T}$ are both $0.3 < p_{\rm T} < 3$ GeV/c. High multiplicity collisions are defined by $220 \leq N_{trk}^{offline} < 260$ and low multiplicity collisions by $2 \leq N_{trk}^{offline} < 20$. Cumulant method is using $220 \leq N_{trk}^{offline} < 240$ multiplicity bin. 79

3.31 $\Delta\phi$ distribution of high multiplicity 2-particle correlation and scaled low multiplicity correlation. The scale is from jet yield ratio times associate particle per trigger ratio of p-side trigger(Top) and Pb-side trigger (Bottom) for HIJING only, $0.3 < p_{\rm T}^{\rm trig} < 3$ GeV/c. 80

3.32 $\Delta\phi$ distribution of high multiplicity 2-particle correlation and scaled low multiplicity correlation. The scale is from jet yield ratio times associate particle per trigger ratio of p-side trigger (Top) and Pb-side trigger, for HIJING +flow with input $v_2 = 0.05$, $0.3 < p_{\rm T}^{\rm trig} < 3$ GeV/c. 81

3.33 The extracted V_2 from high multiplicity 2-particle correlation and with subtraction of scaled low multiplicity correlation. The scale is from jet yield ratio times associate particle per trigger ratio of p-side trigger(Left) and Pb-side trigger (Right), with HIJING (Top) and HIJING+flow(Bottom) with input $v_2 = 0.05$, $0.3 < p_{\rm T}^{\rm trig} < 3$ GeV/c. The black line in top plots is at $V_2 = 0$, in the bottom plots is at $V_2 = 0.0025$. 82

3.34 Near-side correlated yield after $B(\Delta\eta)$ background subtraction for high-multiplicity $220 \leq N_{trk}^{offline} < 260$. The correlated yields are fit by Eq. 3.2. Data are 5.02 TeV pPb collisions for pairs of charged particles with $0.3 < p_{\rm T}^{\rm trig}, p_{\rm T}^{\rm assoc} < 3$ GeV/c, and trigger particle η windows of Pb-side ($-2.4 < \eta_{\rm lab}^{\rm trig} < -2.0$, left) and p-side ($2.0 < \eta_{\rm lab}^{\rm trig} < 2.4$, right.) 84

3.35 Fourier coefficients, V_2 (upper) and V_3 (lower), of two-particle azimuthal correlations in high-multiplicity collisions ($220 \leq N_{trk}^{offline} < 260$) with and without subtraction of low-multiplicity data, as a function of $\eta_{\rm lab}$. Left panel shows data for Pb-side trigger particles and the right panel for the p-side. Statistical uncertainties are mostly smaller than point size; systematic uncertainties are 3.9% and 10% for V_2 and V_3 without low-multiplicity subtraction, 5.8% and 15% for V_2 and V_3 with low-multiplicity subtraction, respectively. The systematic uncertainties are shown by the shaded bands. 86

Figure Page

3.36 Self-normalized anisotropy parameters, $v_2(\eta_{\rm lab})/v_2(\eta_{\rm lab}=0)$ (left panel) and $v_3(\eta_{\rm lab})/v_3(\eta_{\rm lab}=0)$ (right panel), as a function of $\eta_{\rm lab}$. Data points (curves) are results with (without) low-multiplicity data subtraction; filled circles and solid line are from the Pb-side trigger. Open circles and dashed line are from the p-side trigger. The bands show systematic uncertainties of $\pm 5.7\%$ and $\pm 14\%$ for $v_2(\eta_{\rm lab})/v_2(\eta_{\rm lab}=0)$ and $v_3(\eta_{\rm lab})/v_3(\eta_{\rm lab}=0)$, respectively. The systematic uncertainties in $v_n(\eta_{\rm lab})/v_n(\eta_{\rm lab}=0)$ without subtraction are similar. Error bars indicate statistical uncertainties only. 87

3.37 $v_2(\eta_{\rm cm})/v_2(-\eta_{\rm cm})$, as a function of $\eta_{\rm cm}$ in the center-of-mass frame. The data points are results from $V_n^{\rm sub}$ with low-multiplicity data subtracted. The bands show the systematic uncertainty of $\pm 5.7\%$. Error bars indicate statistical uncertainties only. 88

3.38 Self-normalized $v_2(\eta_{\rm cm})/v_2(\eta_{\rm cm}=-0.465)$ distribution with low-multiplicity subtraction from Pb-side (filled circles) and p-side (open circles) triggers, and $\langle p_{\rm T}\rangle(\eta_{\rm cm})/\langle p_{\rm T}\rangle(\eta_{\rm cm}=0)$ of $0<p_{\rm T}<6$ GeV/c range from minimum-bias events (solid line) and $0.3<p_{\rm T}<3$ GeV/c range from high-multiplicity ($220\le N_{trk}^{offline}<260$) events (dotted line) as functions of $\eta_{\rm cm}$. Dashed curve is the hydrodynamic prediction [77] for $\langle p_{\rm T}\rangle(\eta_{\rm cm})/\langle p_{\rm T}\rangle(\eta_{\rm cm}=0)$ distribution. 89

4.1 A sketch of one event that most part of away-side jet is at the large η region. Different η ranges (close-, far- and out-regions) are shown on the sketch. 93

4.2 The $P_{\rm x}$ distribution of PbPb collision at $\sqrt{s_{_{NN}}}=2.76GeV$. Left: $150<N_{\rm trk}^{|\eta|<1.2}<200$. Right: $950<N_{\rm trk}^{|\eta|<1.2}<1000$. 94

4.3 The $dN/d\eta$ distribution of different Z-vtx range for 1 GeV/c $<p_{\rm T}<$ 1.5 GeV/c and $150<N_{\rm trk}^{|\eta|<1.2}<200$. Left: $|z_{vtx}|<1$ cm before and after symmetrization. Right: The $dN/d\eta$ distribution of -15 cm $<z_{vtx}<$ -13 cm and 13 cm $<z_{vtx}<15$ cm. 95

4.4 The η and Z-vtx correction example for centrality $200<N_{\rm trk}^{|\eta|<1.2}<250$ and 1 GeV/c $<p_{\rm T}<1.5$ GeV/c. 96

4.7 The correlation function of close - far region for 0.4 GeV/c $<pt<$ 1.0 GeV/c of PbPb collision at $\sqrt{s_{_{NN}}}=2.76GeV$. Left: $0<N_{\rm trk}^{|\eta|<1.2}<250$. Right: $750<N_{\rm trk}^{|\eta|<1.2}<1000$. 98

4.8 The jet width result of other $P_{\rm x}$ cuts (2.5% and 10%) to the default $P_{\rm x}$ cut (5%) ratio. The RMS of this ratio distribution is considered as the systematic uncertainty. 100

Figure Page

4.9 The jet width result of other P_{x} cuts (2.5% and 10%) to the default P_{x} cut (5%) ratio. The RMS of this ratio distribution is considered as the systematic uncertainty. 101

4.10 The jet width result of tight and loose cuts to the default track cut ratio. The RMS of this ratio distribution is considered as the systematic uncertainty. 102

4.11 The jet width result as a function of $N_{\mathrm{trk}}^{|\eta|<1.2}$ with systematic uncertainty of PbPb collision at $\sqrt{s_{_{NN}}}$=2.76 TeV. 103

SYMBOLS

p_T	transverse momentum
η	pseudorapidity
ϕ	azimuthal angle
v_2	elliptic flow
v_3	triangular flow

ABBREVIATIONS

LHC	Large Hadron Collider
CMS	Compact Muon Solenoid
HF	Hadronic Foward
ECAL	Electromagnetic Calorimeter
HCAL	Hadronic Calorimeter
EP	Event Plane
RP	Reaction Plane
L1	Level 1 (experimental trigger level)
HLT	High Level Trigger
ZYAM	Zero Yield At Minimum

ABSTRACT

Xu, Lingshan PhD, Purdue University, August 2016. Two-particle correlation studies in heavy ion collisions at the Large Hadron Collider . Major Professor: Fuqiang Wang.

Results on two-particle angular correlations in pPb at $\sqrt{s_{NN}}$=5.02 TeV and PbPb collisions at $\sqrt{s_{NN}}$=2.76 TeV are reported. The long-range correlations in pseudorapidity ("ridge") has been seen in various systems, including PbPb, pPb and pp systems. In this thesis, two-particle correlations in pPb collisions at nucleon-nucleon center-of-mass energy of 5.02 TeV are studied as a function of the pseudorapidity separation ($\Delta\eta$) of the particle pair at small azimuthal angle separation ($|\Delta\phi| < \pi/3$). The correlations are decomposed into a jet component that dominates the short-range correlations ($|\Delta\eta| < 1$), and a component that persists at large $\Delta\eta$, which is the ridge. The ridge may be associated with collective behavior of the produced system, well described by hydrodynamics. The azimuthal correlations, after subtraction of the jet component, are characterized by the V_2 and V_3 coefficient. The single-particle anisotropy parameters v_2 and v_3 are extracted and normalized by their mid-rapidity value. The normalized $v_2(\eta_{\rm cm})/v_2(\eta_{\rm cm} = -0.465)$ distribution as a function of the center-of-mass pseudorapidity $\eta_{\rm cm}$ is found to be asymmetric about $\eta_{\rm cm} = 0$, with smaller values observed at forward proton direction pseudorapidity, and smaller value at backward Pb direction, but the decreasing trend towards the two sides is different. The normalized $v_3(\eta_{\rm cm})/v_3(\eta_{\rm cm} = -0.465)$ distribution has no significant pseudorapidity dependence within the statistical uncertainties. The underlying physics for the η dependence of the v_2 parameter is under extensive research at the time of this thesis writing.

The two-particle correlation method is widely used also in jet-like correlation studies. The jet axis direction can be identified effectively by a high $p_{\rm T}$ particle.

The away-side partner jet is quenched in heavy ion collisions due to medium interactions. The biggest challenge in jet correlation studies is the subtraction of the large underlying anisotropy flow backgroud. In previous studies, the flow background is calculated from the measured Fourier coefficients, which results in large uncertainties. In this thesis, the away-side jet shape of PbPb collisions at $\sqrt{s_{_{NN}}}$=2.76 TeV is studied utilizing a novel method of subtracting flow background using the data itself. The away-side is enhanced by a relatively large recoil transverse momentum in a given η range. The two-particle correlation function is constructed from different η regions, one is close and the other far away from the away-side jet. These two η regions are symmetric about $\eta = 0$, so the flow background is the same. The correlation function difference between these two regions, therefore, measures the away-side jet shape. The jet width is studied as a function of multiplicity and p_{T}. It is found that the jet width increases with multiplicity, indicating jet broadening in medium.

1. Introduction

1.1 Fundamental forces and particles

"What is the constitute of the universe?" This is a question that physicists have pursued for a long time. As we know today, there are four basic forces in the universe: gravitational force that is responsible for Newton's falling apple; electromagnetic force that contributes to most phenomena in our daily life, such as the repulsion of like charges; strong interaction that binds the neutron and proton together to form a nucleus and contributes to the interaction between hadrons; and the weak interaction that governs the change of the quark flavors.

In the standard model, the leptons and quarks are the basic building blocks of the universe. They carry 1/2 spin and are grouped into three generations [1]. For each particle, there is a corresponding anti-particle with the same mass and opposite quantum numbers. Quarks have six different flavors: up, down, charm, strange, top and bottom. Quarks possess three different colors, usually denoted as "blue", "red", and "green" which cause them to engage in strong interactions. Oppositely, leptons participant in weak interactions and do not carry color charge. The quark cannot appear freely; they group together and form hadrons. Experimentally, all the observed particles are "white" (i.e. colorless). The interactions between particles are mediated by the gauge bosons. Photons are responsible for electromagnetic force between charged particles, which are described by quantum electrodynamics (QED). The $W^{\pm}$ and Z^0 bosons carry the weak interaction, which are described by the electroweak theory. The strong interaction between hadrons is mediated by gluons, which are described by quantum chromodynamics (QCD). The three groups of quarks and the force carriers are shown in Fig. 1.1.

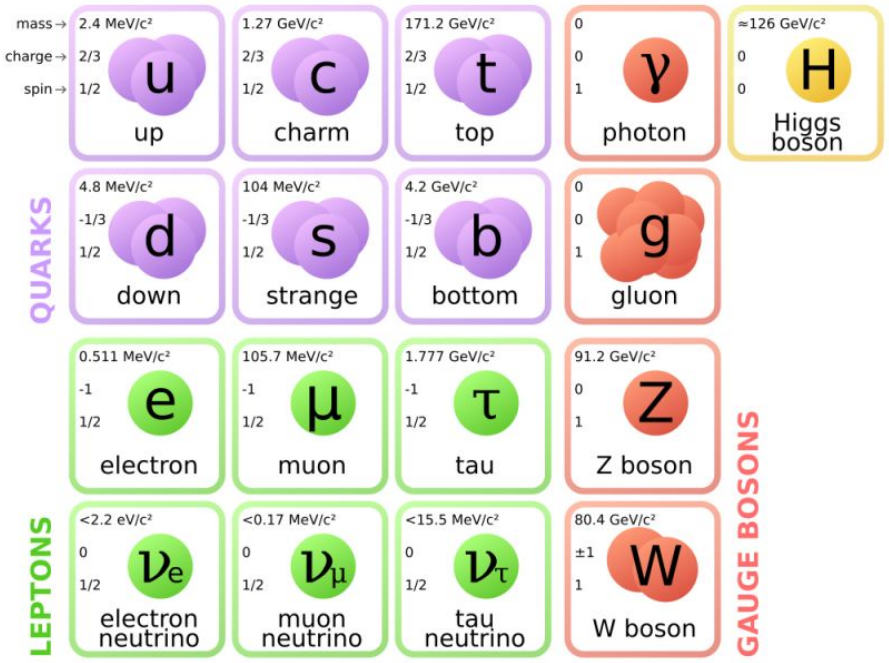

Figure 1.1. A schematic of quark generations and force carriers.

1.2 Quark model and Strong interaction

From the 1950s, with the new experimental techniques as well as cosmic ray studies, many kinds of resonance particles have been discovered (Kaons, Pions, Lambdas etc.), which are called as hadrons. Hadrons are the bound states of their valence quarks and antiquarks. There are two subsets of hadrons: baryons are made of three quarks which result in with half-integer spins, and mesons, which are made of $q\bar{q}$ with integer spins. The arrangement of how hadrons are bound can be described by SU(3) symmetry group, or the "eightford way". This quark model was independently proposed by Murray Gell-Mann [2] and George Zweig [3] in 1964. In the quark model, quarks and antiquarks carry quantum numbers, which give rise to the quantum number of hadrons. These quantum numbers include baryon number, isospin, strangeness and etc. More experimental evidence of the existence of the quark was discovered later in 1968; researchers found that proton also contains internal structure, which was later known as quarks [4].

The strong interaction force is carried out by gluons with color charge exchange. The color charge in strong interaction plays a similar role as the charge in electromagnetic force. The strong interaction is described by QCD (Quantum Chromodynamics) theory, which is a non-abelian theory with symmetry group SU(3). Distinct from the force carrier photon in electromagnetic fields, gluons carry color charge and interact with themselves, thus it brings more complexity to the QCD theory. The screening in QCD is similar to the Debye screening of QED plasma. In dense plasma, the electric charge is surrounded by other charge ions and electrons. As a result, the effective Columb potential of charges at some distance away is decreased because of the decreasing of net charge: The effective potential decreases with increasing density. While in QCD, the quark is usually surrounded by a gluon cloud, the color charge it carries tends to leak into the color cloud via gluon-gluon interaction. So when a test quark passes the gluon cloud, the closer it gets to this quark, the fewer color charges it feels. It is actually an anti-screening effect. This result in the fact that coupling constant α_s of strong interaction monotonically decreases as the momentum scale of the measurement increases. As a consequence, in small distances, the color charges behave like free particles, which is referred to the asymptotic freedom [5]. As a result, the partons (quarks and gluons) are confined within certain distance in hadrons [6], and they can move freely within the hadrons. This confinement is the reason that no free quarks has been experimentally observed. But when two color charges are pulled apart, the effective color charge increases with distance. In this condition, a color flux tube is created and the potential increases with the distance.

1.3 QCD under extreme condition

The QCD theory predicts a phase transition at high temperature or high chemical potential. During a phase transition a confined system could become a deconfined medium, in which quarks and gluons can move freely. The phase diagram is usually a type of charts showing conditions and how different phases occur and coexist at

equilibrium. A QCD phase diagram provides a knowledge of understanding of a wide range of phenomena in the space of thermodynamic parameters, such as temperature and chemical potential. A overview of the QCD phase diagram can be found in Ref. [7].

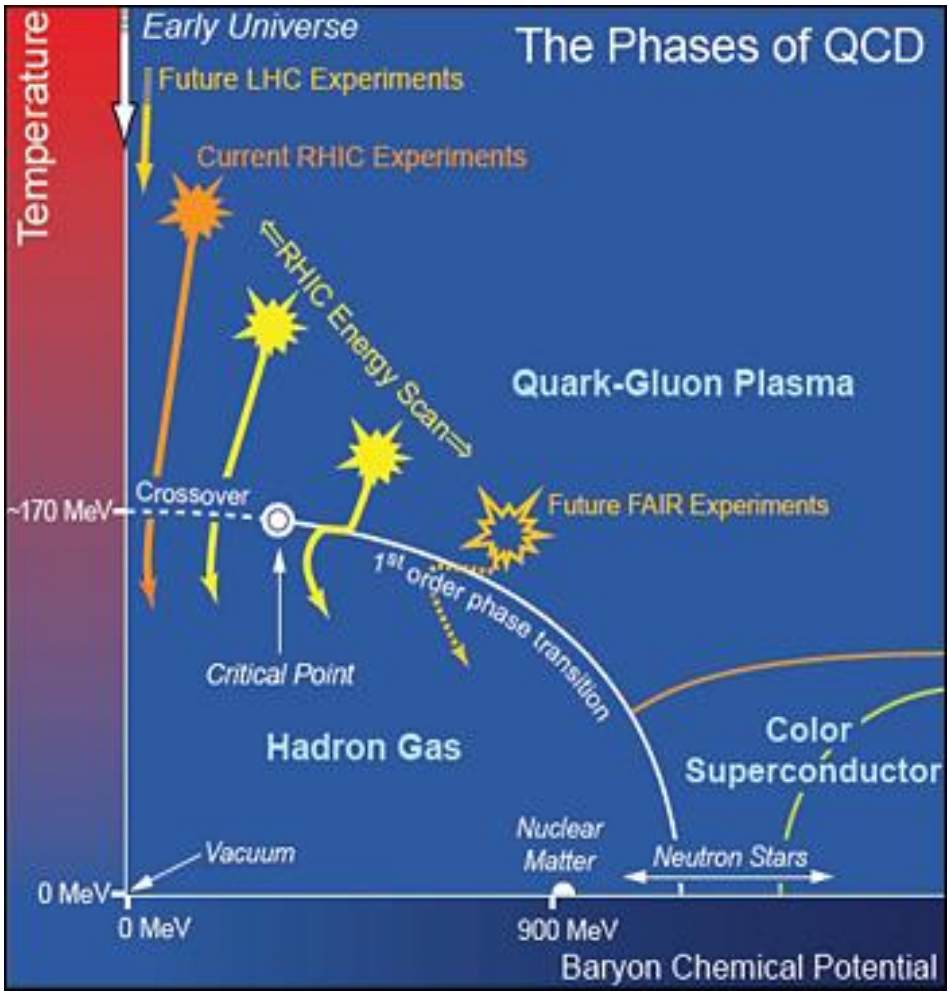

Figure 1.2. A schematic phase diagram. The solid lines show the phase boundaries for the indicated phases. The solid circle depicts the critical point. Possible trajectories for systems created in the QGP phase at different accelerator facilities are also shown. [8]

Figure 1.2 is an example of phase diagram, which shows rich structure with distinct phases of the QCD matter. Starting from baryon chemical potential (μ_B) around the

mass of nucleon ($\approx$ 940 MeV), quarks and gluons are bound inside the nucleon with the hadron size around 1 fm and the QCD energy scale $\Lambda_{QCD} \approx 200$MeV. This is our normal environment. As the μ_B going towards the lower value, or at the temperature above the nuclear binding energy ($\approx$ 10 MeV), the nuclear matter evaporates to gaseous phase hadrons, similar to the liquid-gas transition in the molecular matter [9]. The high temperature and low chemical potential, or high chemical potential and low temperature, the quark matter could go through a phase transition. When the nuclear matter is squeezed towards high μ_B at a low temperature, a first order phase transition will be expected and the system turns into a weakly interacting Fermi liquid of quarks [10,11]. A new condensate of "color superconductivity" could develop, with tendency to break color symmetry.

Another extreme condition can be achieved when the system is heated to very high temperature with low μ_B. As the temperature increases, since hadrons have similar sizes, they start to overlap with each other at a certain critical temperature T_c. Above T_c, the quarks and gluons are deconfined, and the broken chiral symmetry is restored. The system turns into weakly interacting gas with free quarks and gluons, namely the Quark Gluon Plasma (QGP) [12]. The thermodynamic properties can be calculated via Lattice Gauge Theory at $\mu_B = 0$ at a predicted critical temperature $T_c = 170$ MeV. Critical point specifies end point of a phase boundary, beyond with the two phases become indistinguishable. This transition is more like a smooth crossover from hadron phase, which is different from the liquid-gas transition.

1.4 Heavy ion collisions and Quark Gluon Plasma

To study the property of QCD at extremely high temperature and the deconfined QGP matter, an effective experimental method is to accelerate bunches of nuclei to a very high speed so that a huge amount of energy is transferred from initial state energy and can be deposited within a small yet sizable space during a short time. It is currently the only experimental technique that provides the opportunity to create

QGP [13]. The QGP is postulated to have a viscosity that is very close to the lowest possible value predicted by the quantum mechanics uncertainty principle. Because of that, QGP is often referred to 'the perfect liquid'.

High energy heavy ion collision experiments are conducted at the Relativistic Heavy Ion Collider (RHIC) from 2000 with $\mathrm{d}+Au$, $Au+Au$ and $Cu+Cu$ collisions at $\sqrt{s_{NN}} = 200$ GeV. RHIC also provides pp (proton-proton) collisions. From 2009 Large Hadron Collider (LHC) began its operation and has provided PbPb and pPb collisions at energy of 2.76 TeV and 5.02 TeV, it also provides pp collision up to 14 TeV collision energy.

In heavy ion collisions, a large fraction of energy is deposited in a small volume, of size similar to that of the nuclei, generating a system with very high energy density. This hot and dense condition is similar as a few milliseconds after the big bang of the Universe. Once created, the matter undergoes a transition into a form of matter where quarks and gluons are the relevant degree of freedom, called the quark gluon plasma.

Fig. 1.3 is one schematic diagram of the space-time revolution of heavy ion collisions. In the "pre-equilibrium" stage, parton-parton hard scattering may occur in the overlap region. The initial temperature is larger than the critical temperature. During approximately 1 fm/c time after the collision, the fireball is created in the QGP phase, depositing a large amount of energy in the medium. As the fireball expands, the plasma cools down and passes the color confinement transition. At the same time the temperature and energy density decrease because of the expansion. When the temperature reaches the critical temperature, the hot medium is under the transition to color confinement phase, in which quarks and gluons are being confined again. It was commonly believed this phase transition is first order transition, until several years ago, a realistic EOS was used in cosmological calculation. In this EOS the phase transition is a crossover [15]. This hadronization process happens at 10 fm/c after the collision. After hadronization, the system enters hadron gas stage, in which the inelastic scattering happens and the particle species change in the hadron level. As

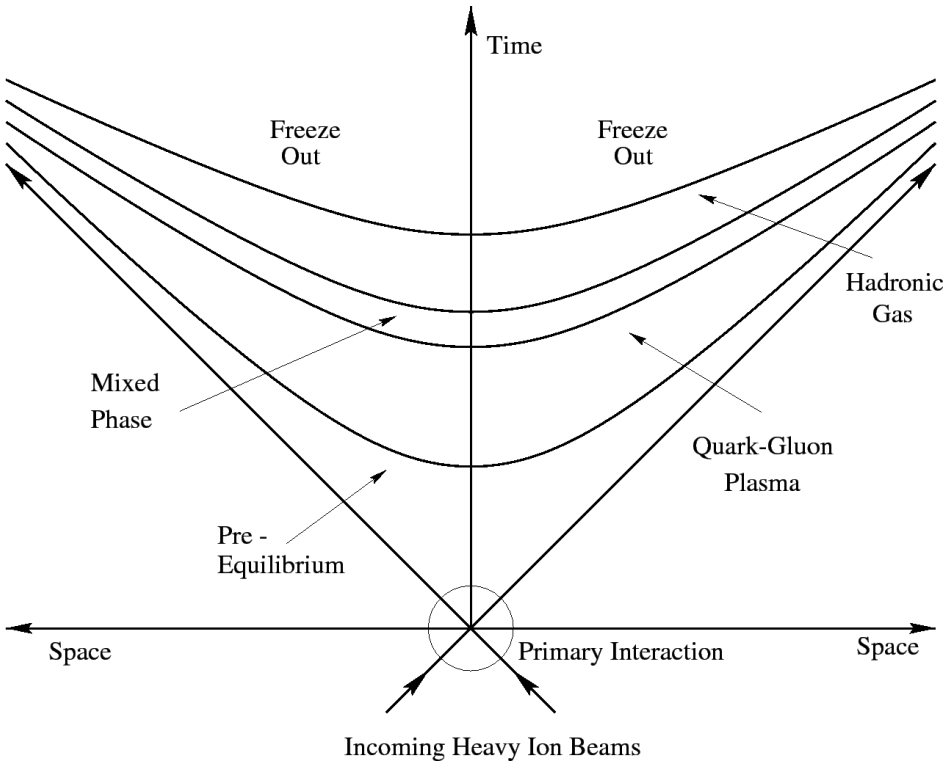

Figure 1.3. A sketch of space-time evolution. [14]

time goes on, the particle ratio becomes fixed, and only elastic scattering happen in the system. This stage is the chemical freeze out. Finally the elastic scattering stops and the system reaches a certain size and temperature. This is generally the end of collective expansion, and the hadrons freely stream out to the detector. These final state particles give a clue of what happened in the initial state collision. Although the direct measurement of QGP cannot be processed in heavy ion experiment, there are pieces of evidences from experimental observations strongly indicating that thermal QGP was created in heavy ion collisions.

1.4.1 Jet as a probe

There are many measurements to investigate the initial state information and the final-state medium interactions. Among those measurements, jet and heavy flavor production as hard probes and particle correlations as soft probes could provide connection to the dynamics of QGP. Some properties of QGP could be estimated via these probes, such as the equation of state and the transport properties [16].

In a hard scattering process between energetic partons, quarks and/or gluons are scattered into large angles. The parton will radiate gluons which then split into quarks, anti-quarks and/or other gluons. This process is known as jet fragmentation and emerges as a collimated spray of detectable hadrons. There are several reasons that jets are essential in QGP study. First, these natural high energy parton probes are produced in hard scattering processes of QCD with a large momentum transfer, thus they can be calculated via perturbative QCD (pQCD). Second, jets are created on a short time scale after the collision, as a consequence, jets have enough time to interact with the QGP, they can also interact with the system before it is thermalized. Thus by studying the jet medium interaction, the QGP medium can be explored [17].

By studying how the jet production changes during this process, we can learn more about energy loss in this hot and dense medium. A common way is to compare the charged hadron spectrum in heavy ion collision (QCD medium) to that for small system, i.e. pp collisions (QCD vacuum), with a smaller energy loss. In this way the relative energy loss can be studied. To quantify this modification, the commonly used measurement is called nuclear modification factor, which is defined as the ratio of particle yield in nucleus-nucleus collisions to the yield in nucleon-nucleon collisions normalized by the appropriate number of equivalent pp collisions. The definition is [18]:

$$R_{AA} = \frac{\sigma_{pp}^{inel}}{\langle N_{coll} \rangle} \frac{d^2 N_{AA}/dp_T d\eta}{d^2 \sigma_{pp}/dp_T d\eta}, \tag{1.1}$$

Where $d^2 N_{AA}/dp_T d\eta$ is the differential yield in nucleus-nucleus collisions, $d^2\sigma_{pp}/dp_T d\eta$ is the differential cross section in proton-proton collision, σ_{pp}^{inel} is the number of binary nucleon-nucleon collisions calculated from a Glauber model of the nuclear collision

geometry, and σ_{pp}^{inel} is the inelastic nucleon-nucleon cross section. A nuclear modification factor smaller than 1 means that the particle p_T spectrum at high p_{T} is shifted to the lower value. This illustrates medium effect in AA collisions where jets lose energy due to interactions with QGP. This suppression phenomenon is often referred to as jet quenching. This is an important piece of evidence that the hot and dense medium is created during the heavy ion collisions. The compact muon collider (CMS) experiment has measured charged particle R_{AA} in PbPb collisions. Fig. 1.4 is a summary of R_{AA} for charged hadrons and neutral pions. The spectra of the observed hadrons are found to be strongly suppressed at high p_{T}.

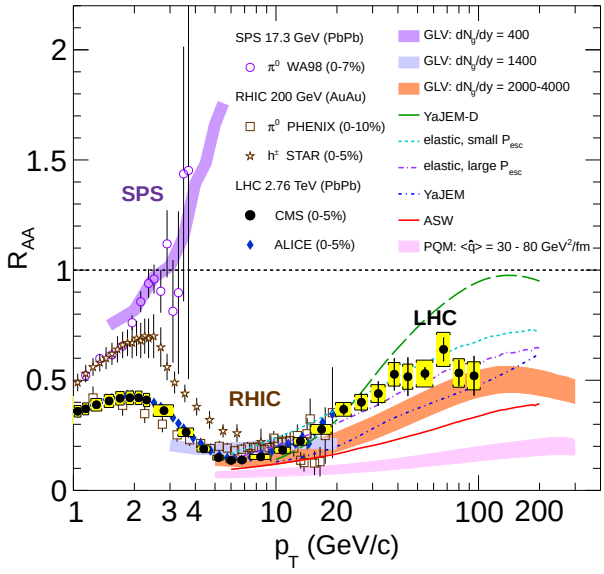

Figure 1.4. Measurements of the nuclear modification factor R_{AA} in central heavy-ion collisions at three different center-of-mass energies, as a function of p_{T}, for neutral pions (π^0), and charged hadrons ($h^{\pm}$), compared to several theoretical predictions. [19]

1.4.2 Anisotropic flow

Another measurement to study collective expansion in the system is collective flow [20, 21], which is regarded as one of the soft probes [22]. In search for the

evidence of QGP, one important issue to address is whether the system reaches local equilibrium. In heavy ion collisions, large number of particles are created. These particles carry information from initial geometry. Typically in a non-central collisions, the overlap region is almond shape. A sketch of the initial geometry is shown in Fig. 1.5.

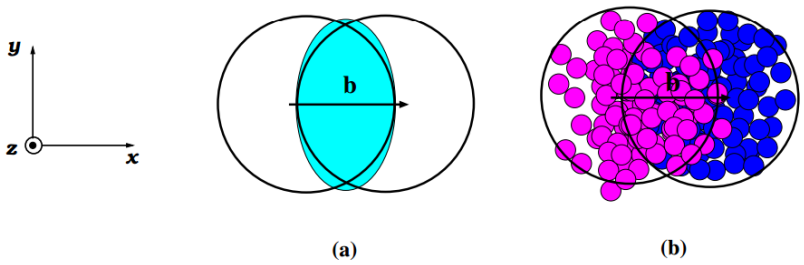

Figure 1.5. Initial geometry of heavy ion collisions. The smooth initial geometry (a) and the initial geometry with fluctuations (b).

In medium, the anisotropic initial shape leads to an anisotropy of the energy density, and thus the pressure gradient. The initial state eccentricity is defined by [23]:

$$\epsilon = \frac{\langle y^2 - x^2 \rangle}{\langle y^2 + x^2 \rangle}, \tag{1.2}$$

where (x, y) represents the spatial position of participant nucleons. The $\langle ... \rangle$ denotes the average over all nucleons. The particle distribution is driven by the pressure gradient in the system. During the evolution, the pressure gradient varies along different directions. The pressure gradient along the short axis of the elliptic shape is larger than along the long axis direction, because the density along the short axis goes more abruptly from maximum to minimum. The pressure gradient affects the particle distributions especially radial accelerations, i.e. the amount of radial flow. So the momentum space distribution is elliptic. In this way the initial anisotropy of coordinate space will be transferred to the final state momentum space. For example, if the particles stream freely from that region, the elliptic shape will not be transferred to the final particle distribution; the particle distribution will be isotropic.

However, with the medium effect, the momentum space distribution of particles will be anisotropic. As a result, the final particle distribution reflects the pressure gradient and medium effects.

The response of the final state anisotropy to initial state distribution is based on the interaction strength among the constituents, or the particle mean free path compared to the system size. If the system size is much smaller than the mean free path, there will be negligible interaction with the medium, thus no final state anisotropy.

The anisotropy is characterized by a Fourier decomposition of azimuthal angle distribution:

$$\frac{dN}{d\phi} \propto 1 + \sum_{n=1}^{\infty} 2v_n \cos[n(\phi - \Phi_{RP})], \tag{1.3}$$

where Φ_{RP} is the true event plane. If we apply orthogonal condition of $\cos[n(\phi - \Phi_{RP})]$ to the above equation, the Fourier coefficient v_n is obtained. Here v_n stands for the n-th harmonic of event azimuthal anisotropy. We can get the n-th harmonic coefficient as:

$$v_n = \langle cos[n(\phi - \Phi_{RP})] \rangle, \tag{1.4}$$

where $\langle ... \rangle$ denotes the average over all particles of all events.

The first harmonic v_1 is called direct flow. It describes the collective sideward motion of the particles, which probes pre-equilibrium, the thermalization stage as well as the initial state information [24–27]. While v_2 and v_3 both reflect medium response to the initial collision geometry. The second harmonics v_2 is called elliptic flow. As discussed above, in non-central collisions, the almond shaped collision zone causes different pressure gradients along different directions, this anisotropy could be quantified by v_2. The triangular flow v_3 at first was predicted to be zero because of the initial state symmetry, however, the non-zero measurements of v_3 from different collisions reveal the fact that the initial geometry varies event by event, which is caused by ϵ_3. The triangular flow characterizes the fluctuation of the triangularity in

the initial geometry of the overlap region. [28] Some measurement of v_2 and v_3 can be found in Refs. [24, 29–32].

1.5 Small collision system

As discussed, the pp system is a common reference for heavy ion collisions. It is the vacuum baseline of the heavy ion collisions, because it is commonly believed that QGP is not created in pp collisions. Furthermore, the parton distribution function in the nucleon, the partonic hard process and fragmentation are well understood [33]. However cold nuclear effects could also lead to the difference of pp and heavy ion collision measurements. The initial multiple soft scattering effect in heavy ion collisions, for example, is absent in pp collisions. Besides, another reference collision system is that of a proton-nucleus system (pA). pA collisions were originally regarded as an excellent reference, since in pA collisions, there are also cold nuclear effect, and the system size is smaller than in AA. Comparing measurements of AA collisions to pA collisions, the cold nuclear effect phenomena could be disentangled from QGP effect.

For example, ALICE (A Large Ion Collider Experiment) has measured nuclear modification factor for both pPb and PbPb in 2012 [34]. As shown in Fig. 1.6, R_{pA} (modification factor in pA system, similar definition as R_{pA}) of pPb is consistent with 1 for p_T greater than 2 GeV, whereas the R_{AA} for PbPb collision is much smaller than 1. This indicates that the strong suppression of PbPb collisions is not due to an initial state effect, but rather a finger print of medium effect after collisions.

Beyond one's expectation, pA collisions provided more information than just a reference. For example, the CMS collaboration has observed the long range ridge structure in pPb collisions [35]. The ridge was initially thought to exist only in AA collisions, as predicted by hydrodynamics. The ridge in pPb motivated a lot physics researches for collecting small system collisions [36–42]. To investigate whether collective flow is responsible for the ridge in pPb collisions,multiparticle correlations were studied in pPb collisions [35, 43, 44] in events with different multiplicity ranges. The

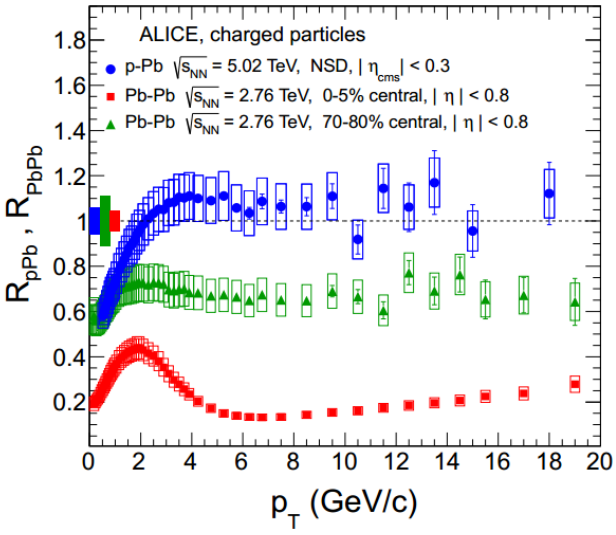

Figure 1.6. Measurements of the nuclear modification factor R_{AA} in pPb collisions at $\sqrt{s} = 5.02TeV$ and compared to central (0-5%) and peripheral PbPb (70-80%) collisions at $\sqrt{s} = 2.76TeV$. [34]

second Fourier coefficient v_2 of the particle azimuthal distributions measured using four-, six-, eight-, or all-particle correlations was found to have the same value [43], as expected in a system with global collective flow [45]. In addition, the particle correlations of identified hadrons were measured in pPb [46,47] and dAu collisions [41]. The anisotropies are observed to depend on the mass of the particle. More specifically, for particles with transverse momentum below about 2 GeV, the anisotropy is larger for lighter particles than for heavier ones. This mass ordering of the anisotropy is qualitatively consistent with hydrodynamics, where particles move with a common flow velocity. The similarities of long-range correlations between the small system collisions and the heavy ion collisions allures a hydrodynamic origin [35,48,49], however, it is still under investigation whether hydrodynamics can be applied reliably to pp or pA systems.

1.6 Two particle $\Delta\eta$-$\Delta\phi$ correlation method

The two-particle correlation is a commonly used method for both the flow and the jet-like correlation measurements. The two-particle correlation is usually done for a certain trigger and associated particle p_{T} range, i.e. p_T^{trig} and p_T^{assoc} for each track multiplicity bin. Multiple p_{T} ranges can be studied and compared to gain physics insights, since the physics for low p_T and high p_T are distinct.

1.6.1 Two particle correlation technique

The two-particle (dihadron) correlation is quantified as a function of the azimuthal angle ϕ and pseudorapidity η differences between two particles (referred to as trigger particle and associate particle):

$$\Delta\phi = \phi_{assoc} - \phi_{trig}, \Delta\eta = \eta_{assoc} - \eta_{trig}. \tag{1.5}$$

The per-trigger-particle associated yield distribution is defined by

$$S(\Delta\eta, \Delta\phi) = \frac{1}{N_{\mathrm{trig}}} \frac{d^2N^{\mathrm{same}}}{d\Delta\eta d\Delta\phi}, \tag{1.6}$$

in which the trigger and associated particles are taken from the same event.

The signal correlation function is approximately of triangular shape in $\Delta\eta$ because of the fixed η acceptance range. The mixed events technique is used to correct the η acceptance. It can also correct for the detector non-uniformity. The mixed event background distribution is defined as:

$$B(\Delta\eta, \Delta\phi) = \frac{1}{N_{\mathrm{trig}}} \frac{d^2N^{\mathrm{mix}}}{d\Delta\eta d\Delta\phi}, \tag{1.7}$$

constructed by pairing the trigger particles in each event with the associated particles from a number of different random events. The symbol N^{mix} denotes the number of pairs resulting from the event mixing.

The dihadron correlation with mixed events correction is defined as

$$\frac{1}{N_{\mathrm{trig}}} \frac{d^2N^{\mathrm{pair}}}{d\Delta\eta d\Delta\phi} = B(0,0) \times \frac{S(\Delta\eta, \Delta\phi)}{B(\Delta\eta, \Delta\phi)}. \tag{1.8}$$

The normalization of both signal and background distributions by dividing by $N_{\rm trig}$ is done after summing up the pair density distributions for all the events and then dividing by the total number of trigger particles from all the events. The normalization factor $B(0,0)$ is the value of $B(\Delta\eta,\Delta\phi)$ at $\Delta\eta = 0$ and $\Delta\phi = 0$. The ratio $B(0,0)/B(\Delta\eta,\Delta\phi)$ represents the pair-acceptance correction factor.

1.6.2 Azimuthal anisotropy from dihadron correlation

The azimuthal anisotropy harmonics can be obtained from a Fourier decomposition two-particle $\Delta\phi$ correlation functions,

$$\frac{1}{N_{\rm trig}}\frac{{\rm d}N^{\rm pair}}{{\rm d}\Delta\phi} = \frac{N_{\rm assoc}}{2\pi}\left\{1 + \sum_n 2V_{n\Delta}\cos(n\Delta\phi)\right\}, \tag{1.9}$$

as described in Refs. [50, 51], where $V_{n\Delta}$ are the Fourier coefficients and $N_{\rm assoc}$ represents the number of associate particles per trigger particle for a given $(p_{\rm T}^{\rm trig}, p_{\rm T}^{\rm assoc})$ bin.

For the trigger and associate particles from full ϕ and η acceptance, a minimum η gap of 2 units is applied to remove short-range correlations such as jet fragmentation [35]. The elliptic and triangular anisotropy harmonics, $v_2\{2, |\Delta\eta| > 2\}$ and $v_3\{2, |\Delta\eta| > 2\}$, from two-particle correlation method can be extracted from the fitted Fourier coefficients as a function of $p_{\rm T}$, or direct calculation of Fourier coefficient,

$$V_{n\Delta} = \langle {\rm cos}n\Delta\phi\rangle. \tag{1.10}$$

Here $\langle ...\rangle$ represents the average over all particle pairs. The single particle azimuthal anisotropy is then calculated via

$$v_n\{2, |\Delta\eta| > 2\}(p_{\rm T}) = \frac{V_{n\Delta}(p_{\rm T}, p_{\rm T}^{\rm ref})}{\sqrt{V_{n\Delta}(p_{\rm T}^{\rm ref}, p_{\rm T}^{\rm ref})}},\ n = 2, 3. \tag{1.11}$$

In the analysis discussed in the following section, the reference particle $p_{\rm T}^{\rm ref}$ range is chosen to be $0.3 < p_{\rm T} < 3.0$ GeV/c.

In addition, the low-multiplicity subtraction is used to minimize the contribution from jets. At large $\Delta\eta$, the near-side jet contribution is minimal, but the away-side

jet still contributes. The jet contributions may be significantly reduced or eliminated by subtracting low-multiplicity collisions data. [35]

In some analyses [35], the second-order elliptic harmonics was also determined from a four-particle cumulant analysis using the Q-cumulant method, $v_2\{4\}$, described in Ref [52].

1.6.3 Long range near-side ridge analysis

As discussed in section 1.6, measurement of azimuthal two-particle correlations is a powerful tool to study the properties of the medium. The two-particle correlation leads to the ridge-shaped long-range correlations at small $\Delta\phi$ as an extensive structure to large $\Delta\eta$ range. This ridge has been studied both at RHIC and LHC for various collision types over a wide range of energy and system size. The ridge, first discovered in central AA collisions, was observed after elliptic flow (second Fourier coefficient v_2) subtraction [53–55]. The origin of the ridge in AA collisions has been quantitatively described in multiple models. It may be primarily attributed to triangular anisotropy (third Fourier coefficient v_3), generated by hydrodynamic expansion from a nonuniform energy density distribution in the initial state that fluctuates on an event-by-event basis [28]. In the hydrodynamic picture with initial geometry fluctuations, all Fourier harmonics (v_n) are possible; it is more straightforward to treat v_n on equal footing as modulation around an average, uniform azimuthal distribution.

The ridge correlations were also observed in high-multiplicity pp and pPb collisions [36–39]. The similarity to the heavy ion ridge suggests a hydrodynamic origin [35, 48, 49], however, whether hydrodynamics can be reliably applied to pp and pA systems is under active debate. Another proposed mechanism is the color glass condensate (CGC) where the two-gluon density is enhanced at small $\Delta\phi$ over a wide $\Delta\eta$ range [56, 57].

An example of signal and background pair two-dimensional (2-D) distributions in $\Delta\eta$ and $\Delta\phi$ is shown in Fig. 1.7 for $1 < p_{\mathrm{T}} < 3$ GeV/c in 2.76 TeV PbPb data

(left) and in 5.02 TeVpPb data (right) [35]. The near-side jet-like structure around $(\Delta\eta, \Delta\phi) = (0, 0)$ on both PbPb and pPb system, is observed in the correlation. Yet another profound phenomenon of the extensive structure at near-side($\Delta\phi \approx 0$) along $\Delta\eta$ direction is seen not only in PbPb, but also in pPb with a comparable strength. The extensive long range structure is called "ridge", which had been observed in many different nuclei species and energy AA collisions, was first observed in a pA system. Along with the away-side ridge structure, the $cos(2\Delta\phi)$ azimuthal structure is seen in both systems. The away-side also contains away-side jet, which should be taken into account in the ridge study. In some paper the low-multiplicity subtraction was used to subtract the jet contribution [38]. The ridge in non-central AA system is believed to be explained by the hydrodynamics. However the physics behind pPb ridge is still under debate.

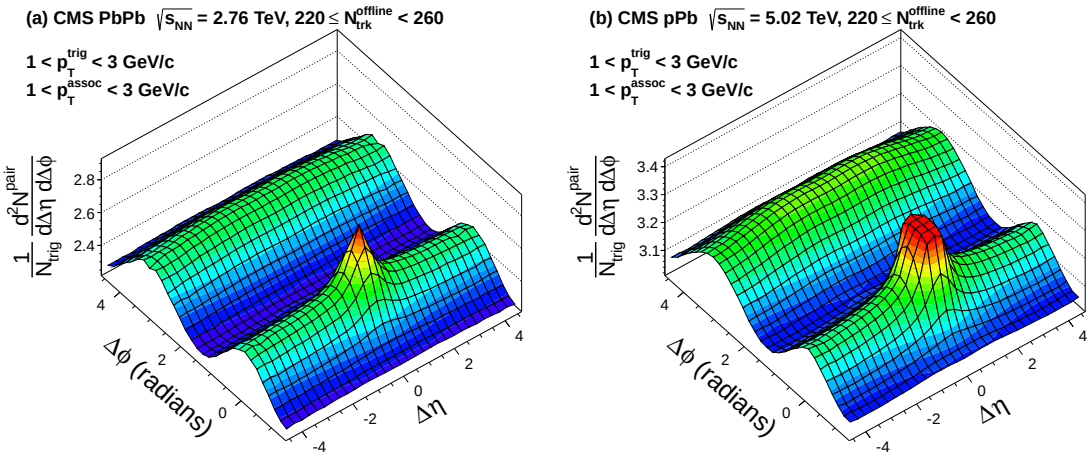

Figure 1.7. The 2D two-particle correlation functions for (a) 2.76 TeV PbPb and (b) 5.02 TeV pPb for pairs of charged particles with $1 < p_T < 3$ GeV/c within $220 \leq N_{trk}^{offline} 260$ multiplicity bin. [35]

To study the detailed long-range correlation structure, the elliptic anisotropy v_2 and triangular flow v_3 are measured in pPb and PbPb from the two-particle correlation and cumulant methods. As discussed in Eq. 1.9, the Fourier coefficient can be extracted from two-particle correlation. A minimum η gap of 2 units is applied to

remove short-range correlations from jet fragmentation. The elliptic and triangular anisotropy harmonics, $v_2\{2, |\Delta\eta| > 2\}$ and $v_3\{2, |\Delta\eta| > 2\}$, from the two-particle correlation method can be extracted from the fitted Fourier coefficients as a function of p_{T},

$$v_n\{2, |\Delta\eta| > 2\}(p_{\mathrm{T}}) = \frac{V_{n\Delta}(p_{\mathrm{T}}, p_{\mathrm{T}}^{\mathrm{ref}})}{\sqrt{V_{n\Delta}(p_{\mathrm{T}}^{\mathrm{ref}}, p_{\mathrm{T}}^{\mathrm{ref}})}}, n = 2, 3 \tag{1.12}$$

Here, the reference-particle $p_{\mathrm{T}}^{\mathrm{ref}}$ range is chosen to be $0.3 < p_{\mathrm{T}} < 3.0$ GeV/c.

The second-order elliptic harmonics is also determined from a four-particle cumulant analysis using the Q-cumulant method, $v_2\{4\}$, described in Ref. [52].

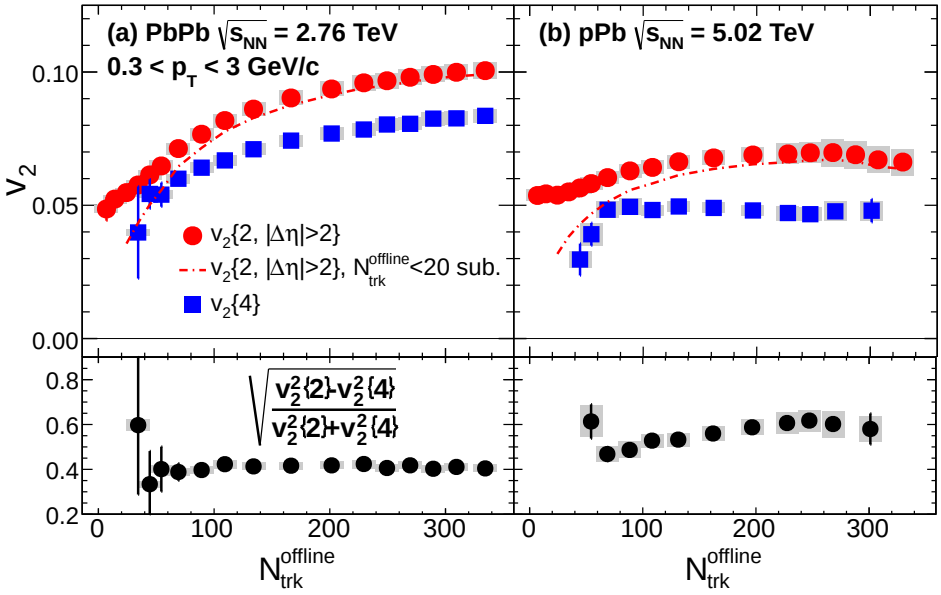

Figure 1.8. Top: The $v_2\{2, |\Delta\eta| > 2\}$ (circles) and $v_2\{4\}$ (squares) values as a function of $N_{trk}^{offline}$ for 2.76TeV PbPb (left) and 5.02 TeV pPb (right) for pairs of charged particles with $1 < p_T < 3$ GeV/c. Bottom: upper limits on the relative v_2 fluctuation estimated from $v_2\{2\}$ and $v_2\{4\}$ in 2.76TeV PbPb (left) and 5.02 TeV pPb (right). [35]

The multiplicity dependence of v_2 and v_3 for PbPb and pPb collisions, averaged over $0.3 < p_T < 3$ GeV/c, are shown in Fig .1.10 and Fig .1.11. The $v_2\{2\}$ and $v_2\{4\}$

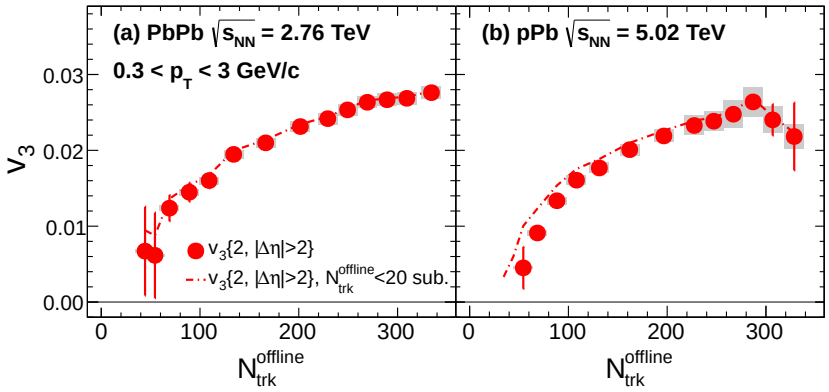

Figure 1.9. The $v_3\{2, |\Delta\eta| > 2\}$ values as a function of $N_{trk}^{offline}$ for 2.76TeV PbPb (left) and 5.02 TeV pPb (right) for pairs of charged particles with $1 < p_T < 3$ GeV/c. d $v_2\{4\}$ in 2.76TeV PbPb (left) and 5.02 TeV pPb (right). [35]

values shows a increasing trend in PbPb collisions, and it is flat in pPb collisions, the magnitude is quite comparable. Moreover in v_3 vs $N_{trk}^{offline}$ plot, the v_3 shows very similar trend and magnitude for pPb and PbPb systems.

$$v_n\{2, |\Delta\eta| > 2\}(p_{\mathrm{T}}) = \frac{V_{n\Delta}(p_{\mathrm{T}}, p_{\mathrm{T}}^{\mathrm{ref}})}{\sqrt{V_{n\Delta}(p_{\mathrm{T}}^{\mathrm{ref}}, p_{\mathrm{T}}^{\mathrm{ref}})}}, n = 2, 3 \tag{1.13}$$

Here, the reference-particle $p_{\mathrm{T}}^{\mathrm{ref}}$ range is chosen to be $0.3 < p_{\mathrm{T}} < 3.0$ GeV/c.

The second-order elliptic harmonics is also determined from a four-particle cumulant analysis using the Q-cumulant method, $v_2\{4\}$, described in Ref. [52].

The multiplicity dependence of v_2 and v_3 for PbPb and pPb collisions, averaged over $0.3 < p_T < 3$ GeV/c, are shown in Fig .1.10 and Fig .1.11. The $v_2\{2\}$ and $v_2\{4\}$ values shows a increasing trend in PbPb collisions, and it is flat in pPb collisions, the magnitude is quite comparable. Moreover in v_3 vs $N_{trk}^{offline}$ plot, the v_3 shows very similar trend and magnitude for pPb and PbPb systems.

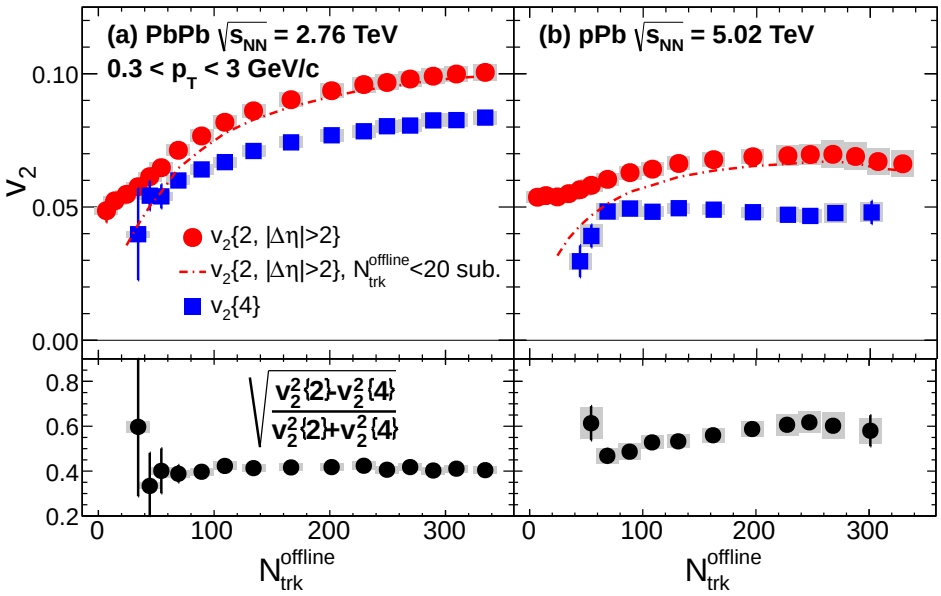

Figure 1.10. Top: The $v_2\{2, |\Delta\eta| > 2\}$ (circles) and $v_2\{4\}$ (squares) values as a function of $N_{trk}^{offline}$ for 2.76TeV PbPb (left) and 5.02 TeV pPb (right) for pairs of charged particles with $1 < p_T < 3$ GeV/c. Bottom: upper limits on the relative v_2 fluctuation estimated from $v_2\{2\}$ and $v_2\{4\}$ in 2.76TeV PbPb (left) and 5.02 TeV pPb (right). [35]

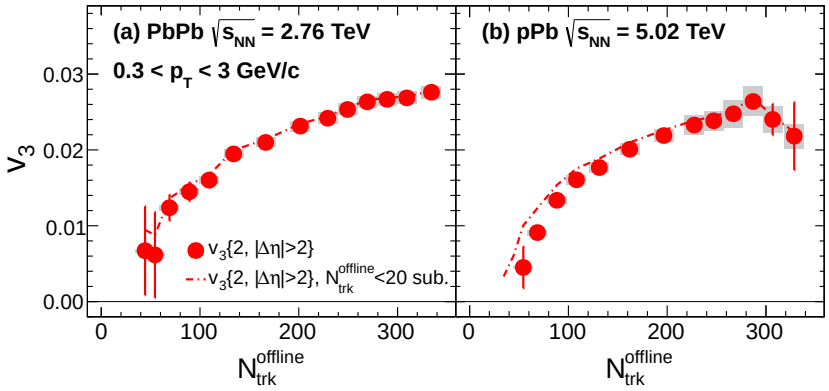

Figure 1.11. The $v_3\{2, |\Delta\eta| > 2\}$ values as a function of $N_{trk}^{offline}$ for 2.76TeV PbPb (left) and 5.02 TeV pPb (right) for pairs of charged particles with $1 < p_T < 3$ GeV/c. d $v_2\{4\}$ in 2.76TeV PbPb (left) and 5.02 TeV pPb (right). [35]

1.6.4 Away side jet measurement

Jets are important probes to study the medium interaction as discussed in section 1.4.1. Jets are produced in pairs. As a result, in heavy ion collisions, one jet is usually closer to the QGP surface than the corresponding back jet (i.e. has shorter path length), and experiences less energy loss, so the energy of the jet will be higher. This is usually called leading jet. The back jet, usually denoted as "subleading jet", however, may go through multiple medium interactions, thus it will be less energetic. A dijet event display is shown on Fig, 1.12. One can utilize the final state particles to reconstruct jets with a certain jet cone ($\Delta R = \sqrt{\Delta\eta^2 + \Delta\phi^2}$).

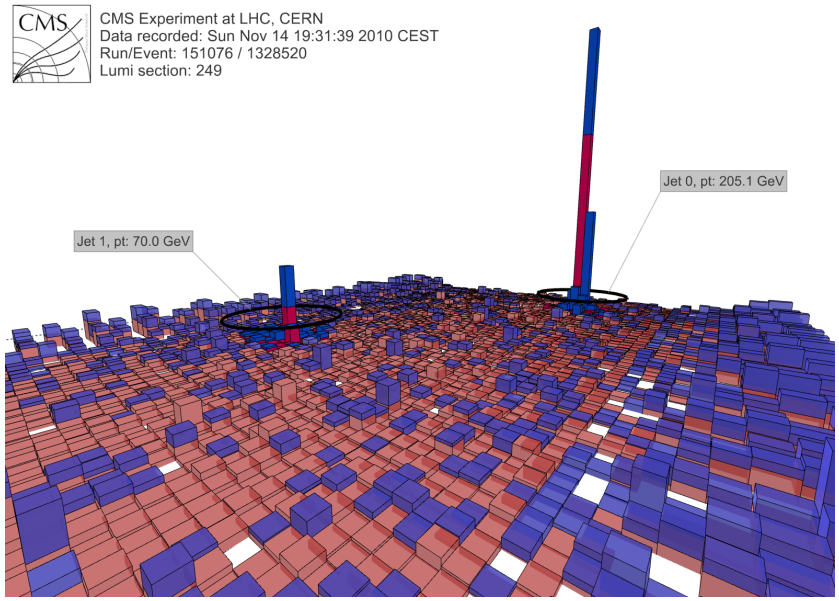

Figure 1.12. A dijet event detected by CMS detector. [58]

Another way to study the jet-like structure is through the two-particle correlation method. In the correlation function, usually the a high p_{T} particle is regarded as the trigger particle, and it is regarded as a substitute for jets assuming it is the leading fragments of the jet (usually $p_{\mathrm{T}} > 3$ GeV/c). The jet suppression and jet broadening are widely studied by two-particle correlation method [59–62]. When selecting the high p_{T} trigger particle, the shortest path jet is more likely to be selected

because it loses less energy. The recoil jet that is produced because of momentum conservation, usually experiences much more medium interactions, as it transverses the QGP through longer path length. So by studying the recoil jet shape, one could get information of the jet medium interaction. Fig. 1.13 compares the dihadron correlation $\Delta\phi$ projection of AuAu and pp for both near-side and away-side. The background is already subtracted from the two-particle correlation function. Two peaks are observed for pp collisions, but not for AuAu collision. Instead, the away-side jet "disappears" because of the jet medium interaction. This jet suppression effect is observed also in other heavy ion collision systems.

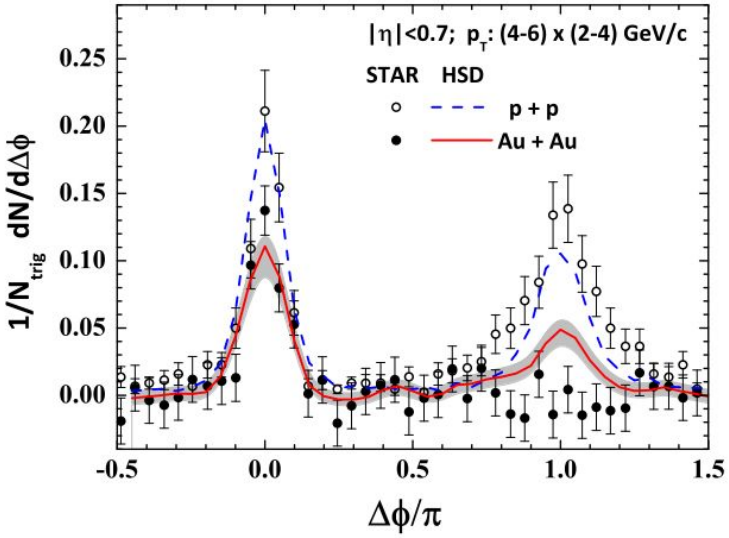

Figure 1.13. Two particle angular correlation from pp and AuAu collision events from STAR data and the Hadron String Dynamic(HSD) transport model calculation. Associated particles are $2 < p_{\mathrm{T}} < 4$ GeV/c and trigger particles are $p_{\mathrm{T}} > 4$ GeV/c. [63]

Fig. 1.14 shows a jet-like probe study done in-plane and out-plane in pp and AuAu collisions. The in-plane flow is directed preferentially to the positive and negative x axes on the transverse plane. [64]. The rest of the particles are out-plane flow. In

the upper panel, the dihadron correlation azimuthal angle distribution exhibits a strong elliptic flow pattern. In most jet-like correlation studies, the background is the biggest challenge. [61,62] The flow background shape could be construct from the Fourier coefficient of the bulk system.

With measured v_n values as input, the flow background shape is fitted to data, usually under the Zero-Yield-At-Minimum (ZYAM) [65] assumption. The ZYAM condition can be obtained by subtracting the lowest value in the distribution. With the ZYAM condition one can decompose the correlation function into jet and Harmonic coefficient.

The lower panel of Fig. 1.14 is obtained by subtracting the ZYAM-fitted elliptic flow background. The near-side jet ($\Delta\phi < 0.75$) was observed in the lower panel. But on the away-side ($\Delta\phi \approx \pi$) an excess is observed for in-plane distribution, but not for out-plane distribution. Comparing to the pp collision result, the suppression in AA is stronger for in-plane and much stronger for out-plane. This is due to the fact that jet modification is much stronger in the in-plane direction.

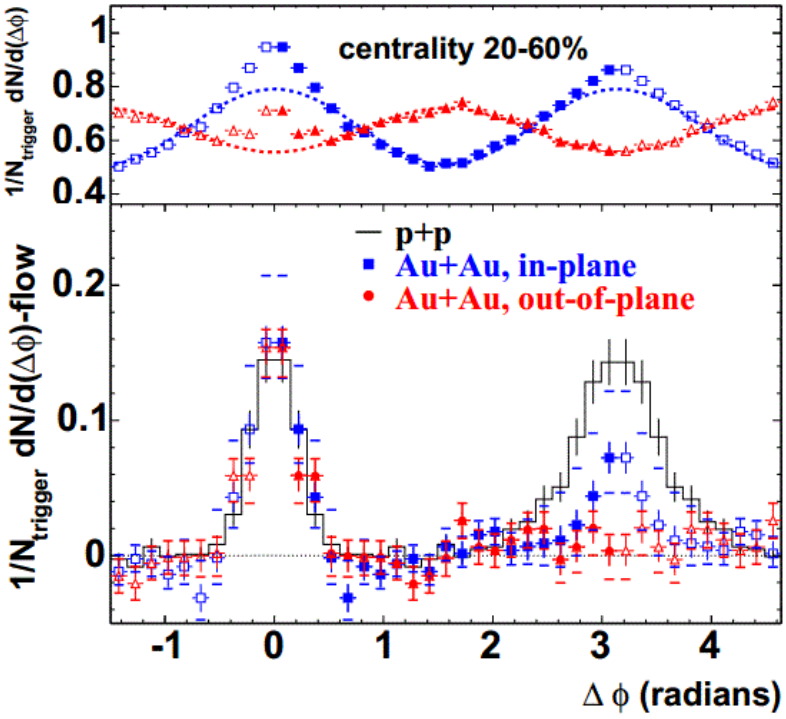

Figure 1.14. Upper: Azimuthal distributions of associated particles for trigger particles in-plane(squares) and out-of-plane(triangles) for AuAu collisions at centrality 20-60%. Open symbols are reflections of solid symbols around $\Delta\phi = 0$ and $\Delta\phi = \pi$. Elliptic flow contribution is shown by dashed lines. Lower: Distribution after subtracting elliptic flow, and the corresponding measurement in pp collisions. [66]

2. Experiemnt setup

2.1 Large Hadron Collider (LHC)

The Large Hadron Collider (LHC) is a two-ring, superconducting hadron accelerator with a circumference of 26.7 km [67] and is built about 100m below the ground. It is the world's largest and most powerful particle collider, built by the European Organization for Nuclear Research (CERN). It accelarates both protons and nuclei. It is designed to accelerate and collide protons at a center of mass energy at 14 TeV and heavy ion bunches at 5.5 TeV per nucleon pair. The protons or heavy ions are accelerated in two separate rings in opposite directions with superconducting magnets. The LHC started its first operation in 2009. From 2010, the LHC began to produce heavy ion collisions. The center-of-mass energy for PbPb collision and pPb collision was $\sqrt{s_{NN}} = 2.76$ TeV and $\sqrt{s_{NN}} = 5.02$ TeV, which are the main collision systems for current heavy ion analyses at LHC. The collision energy of pp collisions was 7 TeV in 2010 and 2011, and it has reached 8 TeV in 2012. From 2015, after the upgrade, the maximum center-of-mass energy for pp collisions could reach 14 TeV, and the lead energy will be up to 5.02 TeV per nucleon pair.

The sketch of LHC is in Fig. 2.1. The accelerator houses 4 main experiments, CMS (Compact Muon Solenoid), ALICE (A Large Ion Collider Experiment), ATLAS (A Toroidal LHC Apparatus) and LHCb (LHC beauty). ATLAS and CMS are multi-purpose detector designed for elementary particle physics investigations but has capability for heavy ion physics. ALICE is designed to solely study the heavy ion collisions.

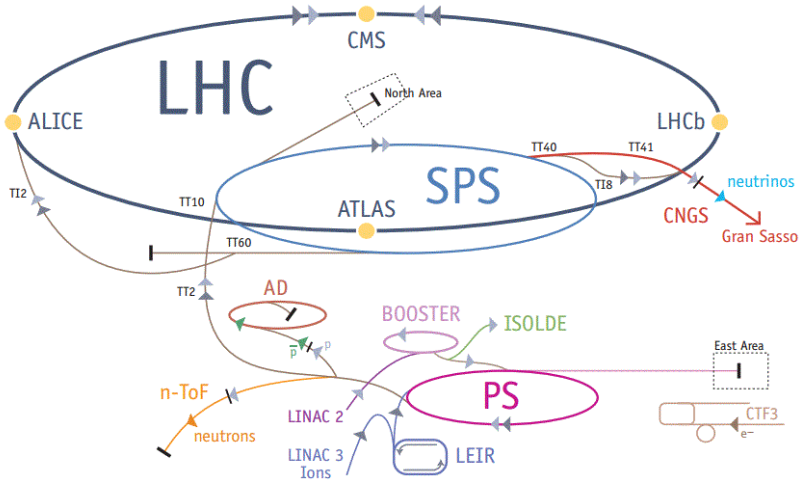

Figure 2.1. Sketch of LHC complex. The pre-accelerator, the LHC storage ring and the 4 main experiments are shown. [67]

2.2 Compact Muon Solenoid

CMS is a multi-purpose a detector. The dimensions are a length of 21.6 m, a diameter of 14.6 m and a weight of 125000 t [68, 69], which is twice the weight of ATLAS. The two beams collide at the center of the CMS detector and the products will go through several layers of the detector. Starting from the innermost layer, the detector composing of a pixel tracker, a silicon strip tracker, an electromagnetic (ECAL) and hadron calorimeter (HCAL), the superconducting solenoid and the muon system. The detector is separated into the central part (barrel region) and the foward part (endcap region). The zoomed view of the CMS detector is in Fig .2.3. Some subdetectors used in the two-particle correlation analysis will be discussed in this section.

To measure the momentum of charged particles, the detector requires magnetic field that bends the particle tracks according to their momentum. CMS uses a superconducting magnet which could reach a maximum of 4T magnetic field. The length

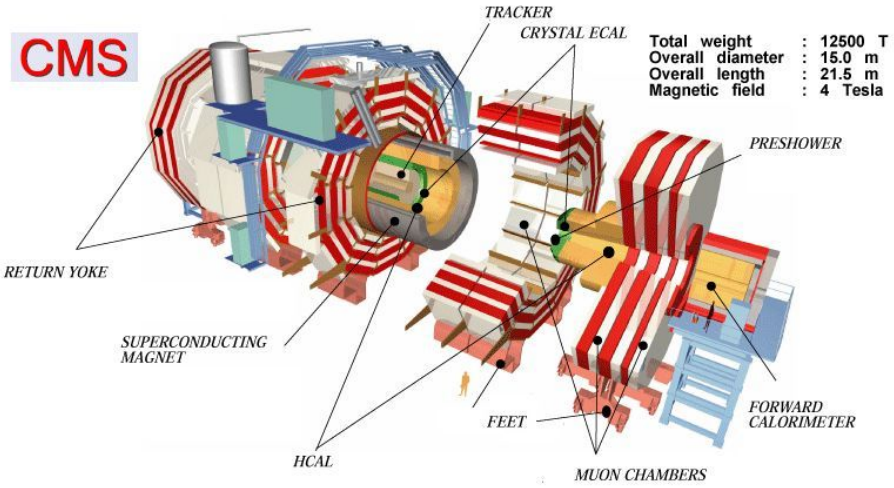

Figure 2.2. CMS detector cross section. From the innermost: pixel tracker, silicon strip tracker, electromagnetic (ECAL) and hadron calorimeter (HCAL), the superconducting solenoid and the muon system. [70]

of the magnet is 13 m and the inner diameter is 5.9 m with a stored energy of 2.67 GJ at full current. The magnet is kept superconducting with liquid helium. The tracking parts and part of the calorimeter are inside the coil. The total tracking volume is approximately a cylinder of 5.8 m in length and 2.6 m in diameter.

The coordinate system in CMS has its origin centered at the nominal collision point in the detector center, the y-axis pointing upwards and the x-axis radially inwards towards the center of the LHC. The z-axis is along the beam direction. The azimuthal angle ϕ is measured from the x-axis in the x-y plane and the radial coordinate in this plane is r. The polar angle θ is measured from the z-axis relative to the counterclockwise beam. The pseudorapidity is defined as $\eta = -\ln(\tan(\theta/2))$. In addition, the transverse momentum and energy, denoted by p_{T} and E_{T}, is the momentum component in the x-y plane.

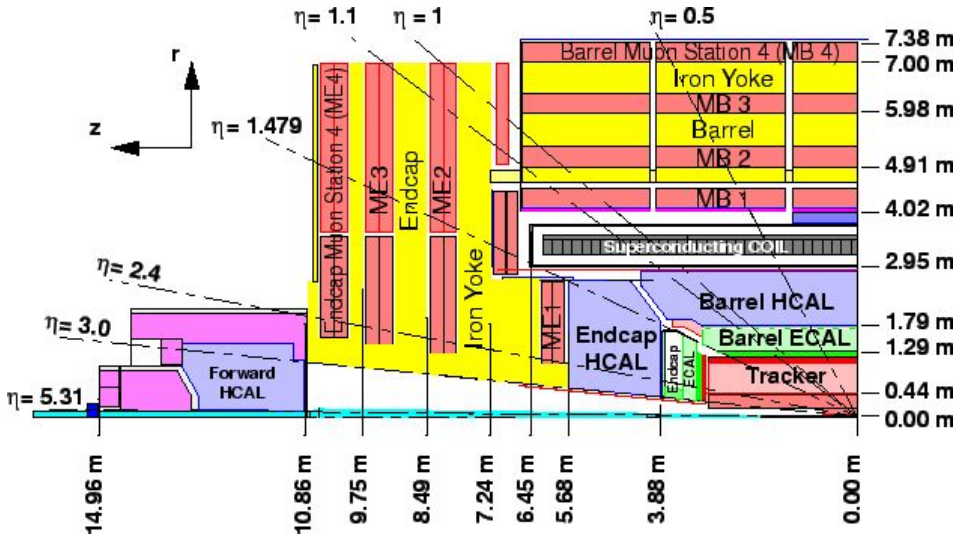

Figure 2.3. Schematic of longitudinal view of CMS detector. The dashed line indicates the limitation of different subdetectors acceptance. [71]

2.2.1 Inner Tracking System

The tracking system is the innermost part of the CMS detector. It provides the precise measurement for reconstructing tracks close to the collision point. The tracking system is also an essential part to reconstruct the primary and secondary vertices and to reconstruct long lived particles such as B_s^0 mesons. It surrounds the interaction points and is 5.8 m in length and 2.5 m in diameter. The magnetic field is 4 T in the full tracking system. At the LHC design luminosity of $10^{34}\text{cm}^{-2}\text{s}^{-1}$ there will be on average about 1000 particles from more than 20 overlapping proton-proton interactions traversing the tracker each bunch crossing. During the design of the tracking system, a couple of requirements needed to be considered. First the system requires fast response, in order to record the huge amount of particles produced in the collision. However, these feature imply a high power density of on-detector

electronics, and as a result, an efficient cooling system is essential. In addition, the amount of material needs to be minimized in order to limit the multiple scattering. Together with the aim to produce a detector with 10 years lifetime, a design of silicon detector was utilized for the tracking system. The silicon tracker is composed of a pixel detector with three barrel layers at radii between 4.4 cm and 10.2 cm and a silicon strip tracker with 10 barrel detection layers extending outwards to a radius of 1.1 m. Each system contains endcaps including 2 disks in the pixel detector and 3 plus 9 disks in the strip tracker on each side of the barrel, extending the acceptance of the detector to $|\eta| < 2.5$. The total volume of the tracker is about 200 m^2, making it the largest silicon tracker that ever built.

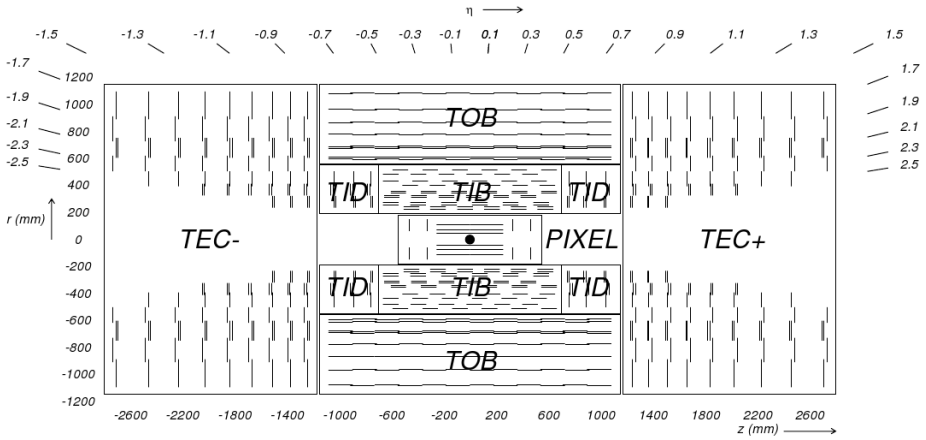

Figure 2.4. Schematic of the CMS silicon tracker cross section. Each line represents a detector module. Double lines indicates back-to-back modules which deliver stero hits. [72]

The schematic drawing the of detailed structrue of the silicon tracker is shown in Fig 2.4. The pixel tracker is the innermost part of the silicon tracker and is closest to the interaction point. It provides precise measurement of the tracking point and it is essential for secondary vertex reconstruction from τ decays. It also provides tracking seeds for the outer tracker and triggering. It covers a pseudorapidity range of $-2.5 < \eta < 2.5$, matching the acceptance of the central tracker.

The radial region between 20 cm and 116 cm is occupied by the silicon strip tracker. It it composed of three subsystems. The Tracker Inner Barrel and Disks (TIB/TID) extend in radius towards 55 cm and are composed of 4 barrel layers, with 3 disks at each end. They are surrounded by the Tracker Outer Barrel(TOB). It has an outer radius of 116 cm and contains 6 barrel layers. The TOB extends in z between $\pm$118 cm. Beyond this range in z there is the Tracker EndCaps (TEC+ and TEC-) covers the z range $124cm < |z| < 282cm$ and $22.5cm < |z| < 113.5cm$.

2.2.2 Calorimeters

The CMS calorimeters consist of an electromagnetic calorimeter (ECAL) and a hadron calorimeter (HCAL), made of layers of absorbing material and scintillators to measure the energy loss of particles traversing the layers. The ECAL identifies electromagnetic showers of eletrons, positrons and photons. The HCAL, on the other hand, measures energy deposited by hadrons due to hadronic interactions.

The ECAL is made of 61 200 lead tungstate($PbWO_r$) crystals on barrel region, and 7324 crystals in each of the two endcap regions, with a coverage of $|\eta| \leq 3.0$. A pre-shower detector is placed in front of the endcap crystals.

The HCAL is designed to study a wide range of high energy processes. The crystals have short radiation length (X_0 = 0.89 cm) and fast response (80% of the light is emitted in 25 ns). The HCAL is located behind the tracker and ECAL as seen from the interaction point. The HCAL barrel is restricted between the outer extend of the ECAL (R=1.77 m)and inner extend of the magnetic coil (R=2.95 m).

The hadronic forward (HF) detector, which is the forward part of the hadronic calorimeter, has a high pseudorapidity region ($3.0 < \eta < 5.0$), designated to allow better separation of particles in the congested forward region. The HF detector plays an important role in many aspects. The main role of the HF detector is the following. First, it provides information for event selection. HF can quantify the topology of soft particle production in a collision, which is an important event discrinimator in many

event types. The centrality of the event can also be studied by selecting different HF energies. The HF detector is placed in the forward region, which is far away from the barrel region of the main observables. By selecting the HF energy, the centrality will be less biased by presence of jets. In addition, the HF detector is widely used in event plane reconstruction, which is the angle in $x - y$ event plane. It is an essential parameter for azimuthal flow analysis.

As discussed above, different types of particles interact differently in the detector system. A schematic figure of how different species of particles are absorbed in the detector is shown in Fig. 2.5.

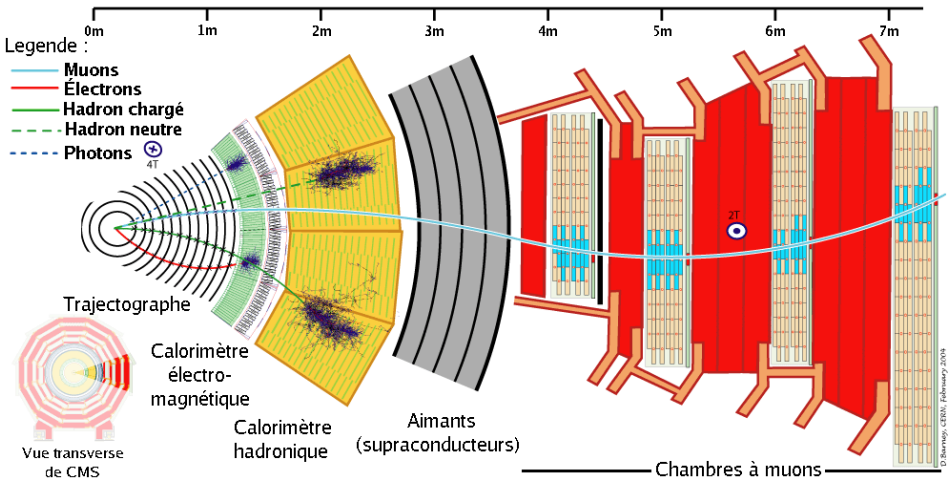

Figure 2.5. Schematic of the cross section of CMS detector and how different species of particles are absorbed in the detector.

2.2.3 Data Sample

The pPb analysis uses the data recorded by CMS during LHC nominal pPb run in January and February of 2013. The CMSSW (The overall collection of CMS software) release version 5_3_8_HI_patch2 was used for data taking, prompt reconstruction and physics analysis. The data were certified by the CMS Physics Validation Team (PVT). Good collision runs and luminosity blocks were selected with the official JSON file

that was signed off on by the PVT. The total integrated luminosity is about 18.4 nb^{-1} for Pb beam going along positive η direction and proton beam going along negative η direction.

The data used in PbPb analysis is recorded by CMS during LHC PbPb run in November and December 2011 at $\sqrt{s_{_{NN}}} = 2.76$ TeV. The CMSSW release version 4_4_2 was used for data taking. The data was then re-reconstructed with improved algorithm. Which helps with better tracking efficiency and wider p_{T} range.

3. Two-particle correlation analysis

In this chapter, multiple methods of two-particle correlation measurements from CMS experiment are described. Then the analysis details including the good track quality cuts and multiplicity selection are described. The results of azimuthal anisotropy and long range dihadron correlations are presented.

3.1 Event selection

3.1.1 L1 and HLT trigger system

The minimum-bias (inclusive) events provided by the LHC in the nominal run allowed the use of a track-based minimum-bias trigger (HLT PAZeroBiasPixel SingleTrack v1). These events were triggered by requiring at least one track with $p_T > 0.4$ GeV/c found in the pixel tracker.

The high multiplicity events were collected by unprescaled trigger (trigger with initial rate). With the goal to study the properties of high multiplicity pPb collision, a dedicated high multiplicity trigger was designed and implemented in the HLT menu. With the two highest paths running unprescaled, each recording data at around 20 Hz. There were five trigger paths for different multiplicity thresholds of online pixel tracks (100, 130, 160, 190, and 220).

The high multiplicity trigger involves two levels. The Level-1 is L1 seeds that one used to filter out events using a scalar sum of total transverse energy. The multiplicity 100 and 130 triggers are seeded by L1_ETT20_BptxAND, 160 and 190 are seeded by L1_ETT40, and 220 threshold trigger is seeded by L1_ETT60.

The high level trigger, on the other hand, selects events based on pixel tracking information. Our trigger paths proceed the following sequences: after reconstructing

the pixel tracks with $p_T > 0.4$ GeV/c and track origin within a cylindrical region of 15.0 cm in half length and 0.2 cm in transverse radius, the CMS standard adaptive online pixel vertexing algorithm is executed with pixel tracks as its seeds. The path is then followed by an HLT filter that counts the number of pixel tracks with kinematic cuts of $|\eta| < 2.4$ and $p_T > 0.4$ GeV/c, within a distance of 0.4 cm to the best found pixel vertex (associated with highest number of tracks). The position of pixel vertices along the beam axis is also required to be within the $z_{vtx} \pm 15$ cm range.

3.1.2 Offline event cuts

In the offline analysis, hadronic collisions were selected by requiring a coincidence of at least one HF calorimeter tower with more than 3 GeV of total energy on both the positive and the negative sides of HF. Events were also required to contain at least one reconstructed primary vertex within 15 cm of the nominal interaction point along the beam axis ($z_{\rm vtx}$) and within 0.15 cm transverse distance to the beam trajectory. At least two reconstructed tracks were required to be associated with the primary vertex. Beam related background was suppressed by rejecting events with a low fraction (25%) of high quality reconstructed tracks. Based on simulations using the HIJING 1.383 event generator, the event selections have a total acceptance of about 96.2% for hadronic inelastic pPb interactions.

3.2 Track Selection and Multiplicity definition

3.2.1 Track Quality cuts

In this analysis, the "generalTracks" collection of reconstruction files was used. For further selections, a reconstructed track was considered as a primary-track candidate if the impact parameter significance $d_{\rm xy}/\sigma(d_{\rm xy})$ (here $d_{\rm xy}$ is the transverse impact parameter, and $\sigma(d_{\rm xy})$ is the error of $d_{\rm xy}$) and significance of z separation between the track and the best reconstructed primary vertex (the one associated with the largest

Table 3.1
Summary of each HLT trigger used for each $N_{trk}^{offline}$ range in pPb collisions.

HLT path	$N_{trk}^{offline}$ range
MB	$[0, 120)$
HLT_PixelTracks_Multiplicity100	$[120, 150)$
HLT_PixelTracks_Multiplicity130	$[150, 185)$
HLT_PixelTracks_Multiplicity160	$[185, 220)$
HLT_PixelTracks_Multiplicity190	$[220, inf)$

number of tracks, or best χ^2 probability if the same number of tracks is found) $d_z/\sigma(d_z)$ are both less than 3. In order to remove tracks with poor momentum estimates, the relative uncertainty of the momentum measurement $\sigma(p_T)/p_T$ was required to be less than 10%.

Comparisons of tracking performance (efficiency and fake rate) as a function of N_{TP} (which should be directly correlated with multiplicity) for $0 < |\eta| < 1.2$ and $1.2 < |\eta| < 2.4$, respectively, are shown in Fig. 3.1 for projection ranges $0.5 < p_T < 2.0$ GeV/c (blue symbols) and $2.0 < p_T < 6.0$ GeV/c (red symbols). Fake rate seems to increase a little when going from low to high multiplicity events. However, the overall fake rate still remains at the 1–2% level. Therefore, corrections for tracking efficiency and fake rate that are applied to the analysis are considered to be multiplicity independent.

3.2.2 Multiplicity Definition

In pPb collisions, the multiplicity is quantified by the number of tracks $N_{trk}^{offline}$. The $N_{trk}^{offline}$ is defined as the number of good tracks within $|\eta| < 2.4$ and $p_T > 0.4$ GeV/c after good track quality selections. The information on which HLT trigger used for which $N_{trk}^{offline}$ range is summarized in Table. 3.1.

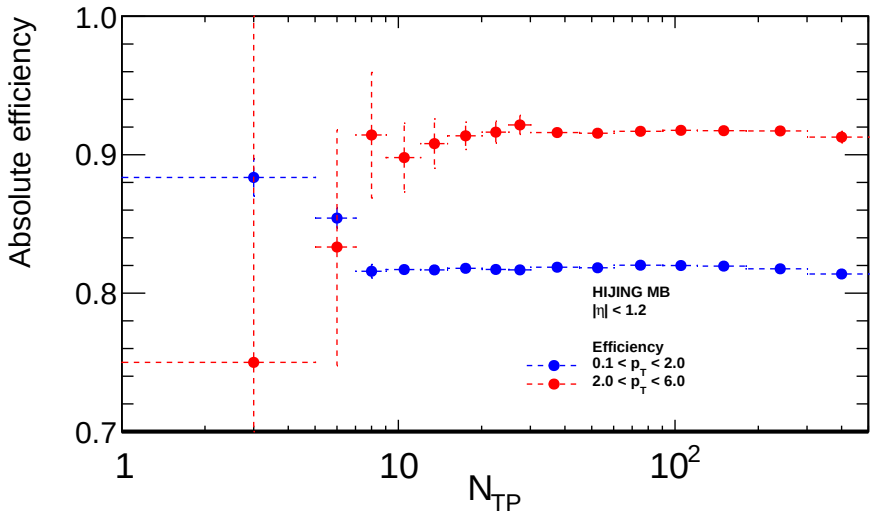

Figure 3.1. Projection of the tracking efficiency as a function of N_{TP} (the total number of simulated tracks in each event) for $0.1 < p_T < 2.0$ GeV/c (blue) and $2.0 < p_T < 6.0$ (red) with $|\eta| < 1.2$. [35]

3.2.3 Tracking correction

Each associated particle track is weighted by the inverse of the efficiency factor, $\varepsilon_{\mathrm{trk}}(\eta, p_{\mathrm{T}})$, as a function of the track's pseudorapidity and transverse momentum. The track efficiency correction is shown in Fig 3.2 as a function of the track's

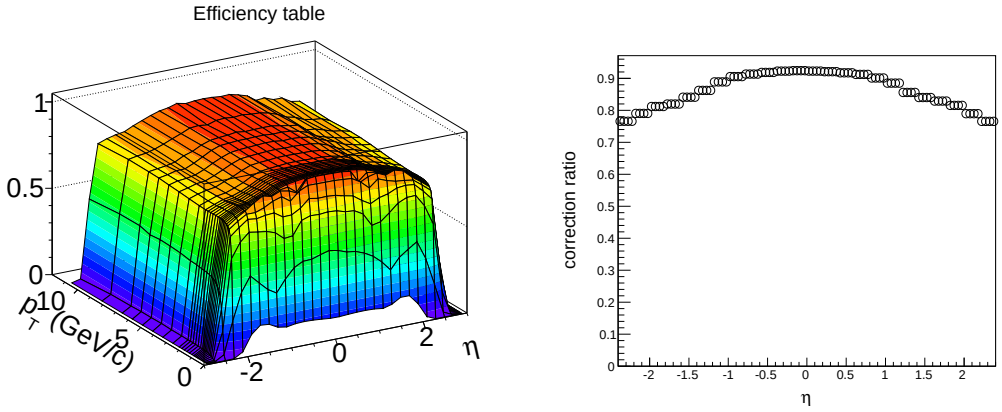

Figure 3.2. Tracking efficiency 2D plot vs η and p_T (left) and the projection on η. The efficiency is obtained from PYTHIA (tune Z2) [73] pp simulation.

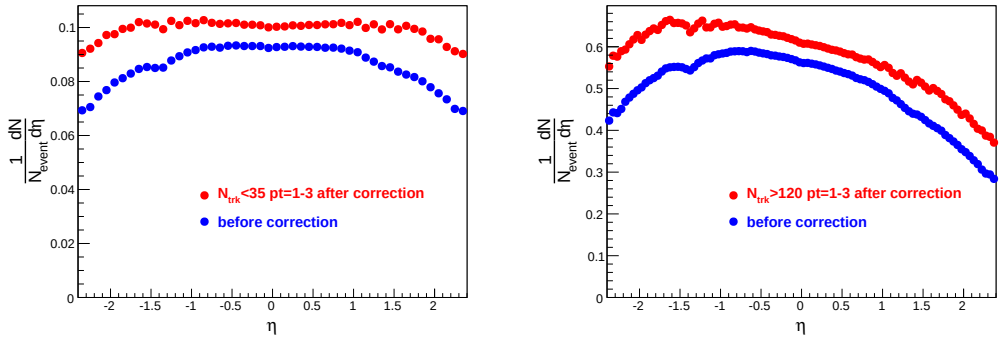

Figure 3.3. Charged particle distribution (within $1 < p_T < 3$ GeV/c) before and after efficiency correction for 5.02 TeV pPb collisions. Two multiplicity bins are shown: $N_{trk}^{offline} < 35$ (left) and $120 \leq \ noff < 150$ (right).

pseudorapidity and transverse momentum. The efficiency as a function η is shown in Fig 3.3.

The efficiency weighting factor accounts for the detector acceptance $A(\eta, p_{\mathrm{T}})$, the reconstruction efficiency $E(\eta, p_{\mathrm{T}})$, and the fraction of misidentified tracks, $F(\eta, p_{\mathrm{T}})$,

$$\varepsilon_{\mathrm{trk}}(\eta_{\mathrm{lab}}, p_{\mathrm{T}}) = \frac{AE}{1-F}\,. \tag{3.1}$$

PYTHIA (tune Z2) simulation result were used to produce the tracking efficiency table according to The associated particles are weighted by the inverse of the efficiency factor, $\varepsilon_{\mathrm{trk}}(\eta, p_{\mathrm{T}})$, as a function of the track's pseudorapidity and transverse momentum. The N_{trig} is accumulated with the corresponding weight.

3.3 Pseudorapidity dependence of azimuthal anisotropy

Dihadron correlations are analyzed between two charged particles, called trigger and associated particles. In this analysis, the trigger particles are restricted to a narrow η range. Two trigger particle η ranges are used in this analysis: $-2.4 < \eta_{\mathrm{trig}} < -2.0$ (lead going side) and $2.0 < \eta_{\mathrm{trig}} < 2.4$ (proton going side). As a result, within $0 < |\Delta\eta| < 4.4$ the dihadron correlation has full acceptance, there is no need to The associate particles are taken from the entire η range of $|\eta_{\mathrm{assoc}}| < 2.4$. The trigger particle p_{T} range is fixed to be $0.3 < p_{\mathrm{T}}^{\mathrm{trig}} < 3$ GeV/c in the main results.

Unlike in previous studies [36–39, 53–55], the trigger particles in this analysis are restricted to two narrow η_{lab} windows: $-2.4 < \eta_{\mathrm{lab}}^{\mathrm{trig}} < -2.0$ (Pb-side) and $2.0 < \eta_{\mathrm{lab}}^{\mathrm{trig}} < 2.4$ (p-side). The associated particles are from the entire measured η_{lab} range of $-2.4 < \eta_{\mathrm{lab}}^{\mathrm{assoc}} < 2.4$.

3.3.1 ZYAM normalization

The raw 2D correlated yield in pPb collision of $\sqrt{s_{_{NN}}} = 5.02$ TeVis shown in Fig. 3.4 with both $-2.4 < \eta_{trig} < -2.0$, $-2.4 < \eta_{assoc} < 2.4$ for 0.3 GeV/c < $p_{\mathrm{T}}^{\mathrm{trig}}, p_{\mathrm{T}}^{\mathrm{assoc}} < 3.0$ GeV/c. In the correlated yield plot, the peak around (0,0) is the

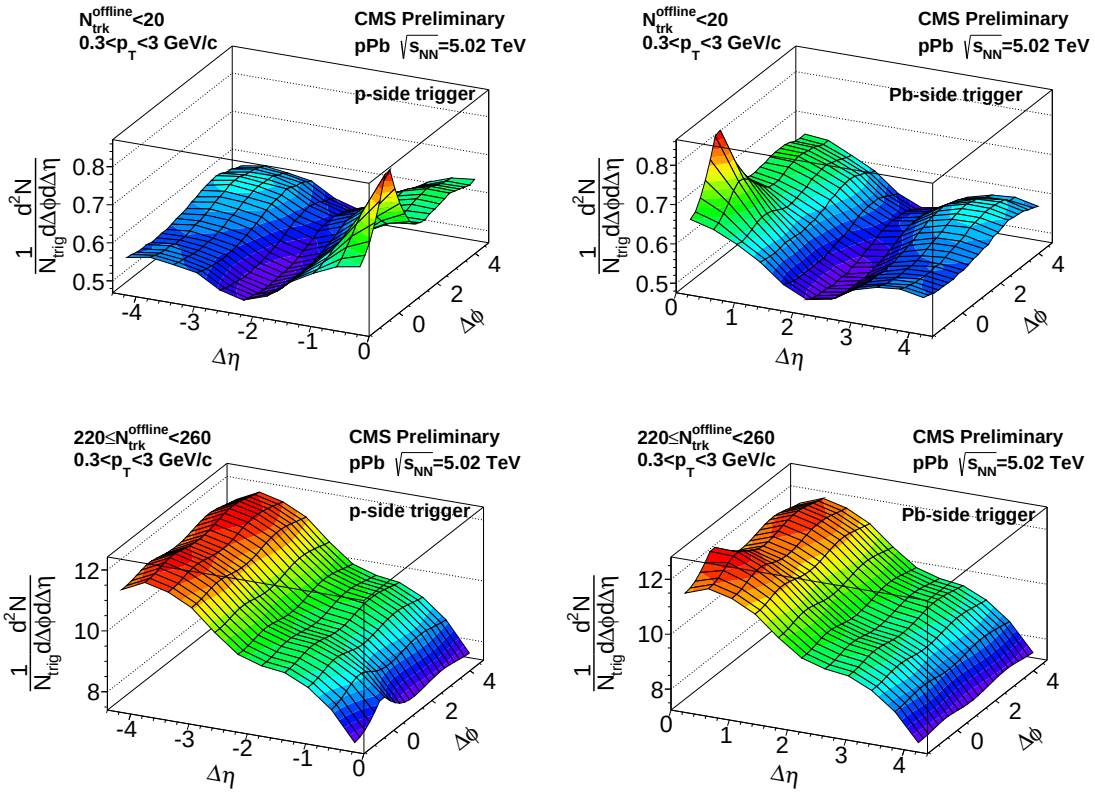

Figure 3.4. 2D correlated yield with $2.0 < \eta_{trig} < 2.4$ (left panel) and $-2.4 < \eta_{trig} < -2.0$ (right panel) for low-multiplicity $2 \leq N_{trk}^{offline} < 20$ (upper panels) and high-multiplicity $220 \leq N_{trk}^{offline} < 260$ (lower panels) pPb collisions at 5.02 TeV. The p_{T} ranges are $0.3 < p_{\mathrm{T}}^{\mathrm{trig}}, p_{\mathrm{T}}^{\mathrm{assoc}} < 3$ GeV/c. The data are efficiency corrected.

near-side jet-like structure, while the extensive feature at $\Delta\phi = 0$ in the large $\Delta\eta$ range is the "ridge" phenomenon. The extensive feature is also seen at away side $\Delta\phi = \pi$, which is believed to contain the back to back jet. Unlike the correlation function in previous pPb analysis (e.g. in [35]), the 2D correlated yield is asymmetric. The structure reflects the asymmetric single particle distribution in the pPb system.

The $\Delta\phi$ distribution of the correlated yield is projected within each $\Delta\eta$ bin with low-multiplicity in Figs. 3.5 and 3.6 and high-multiplicity collisions in Figs. 3.7 and 3.8.

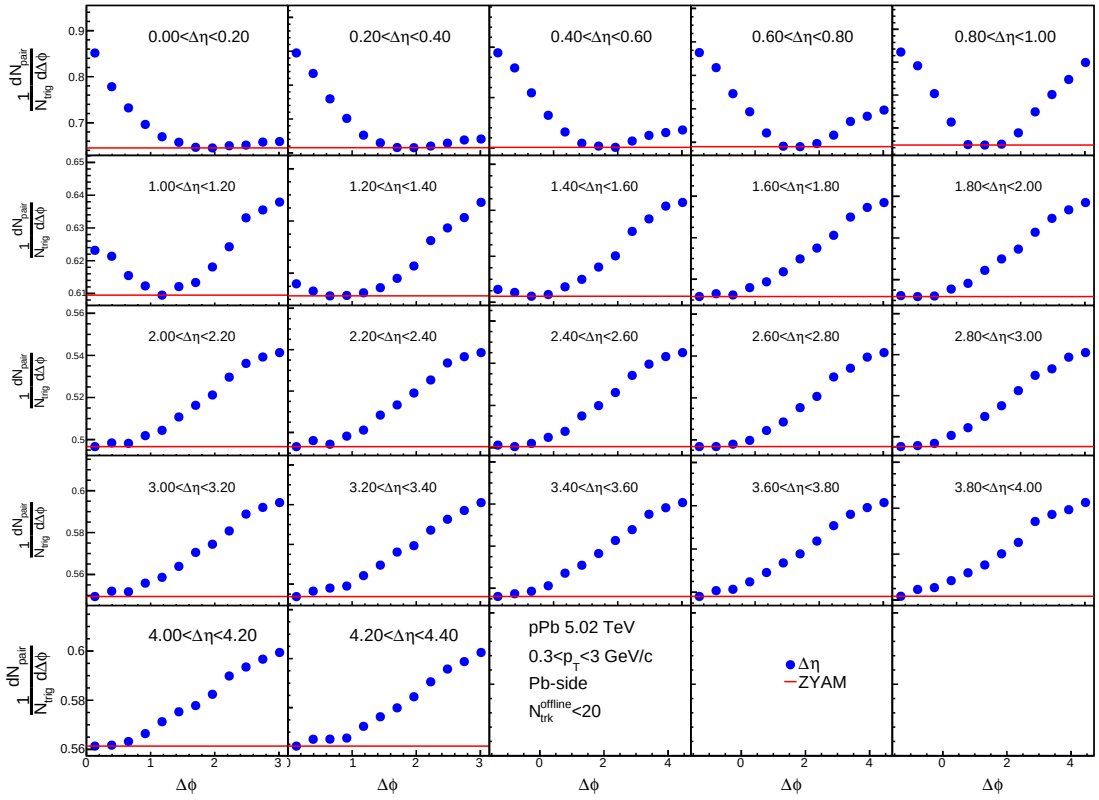

Figure 3.5. $\Delta\phi$ projection of each $\Delta\eta$ bin of 2D correlated yield with $-2.4 < \eta_{trig} < -2.0$ for high-multiplicity $N_{trk}^{offline} < 20$ pPb collisions at 5.02 TeV. The $p_{\rm T}$ ranges are $0.3 < p_{\rm T}^{\rm trig}, p_{\rm T}^{\rm assoc} < 3$ GeV/c. The data are efficiency corrected.

The high multiplicity plots are composed of two characteristic peaks: one at $\Delta\phi = 0$ (near-side) and the other at $\Delta\phi = \pi$ (away-side), with a minimum valley between the two peaks. For low-multiplicity collisions at large $\Delta\eta$, no near-side peak is observed.

In order to study the correlated yields, we subtract the combinatorial background assuming zero-yield-at-minimum (ZYAM) [65]. To obtain the ZYAM background magnitude, the correlated yield distribution is stepped through to find the minimum

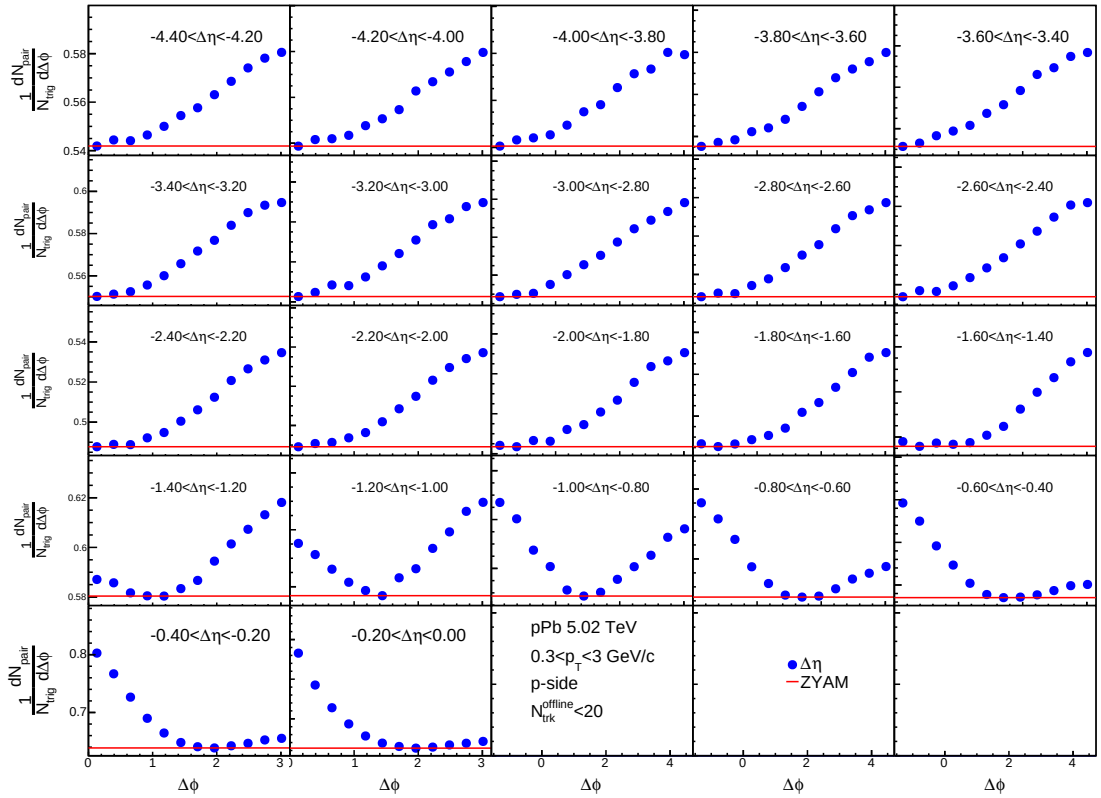

Figure 3.6. $\Delta\phi$ projection of each $\Delta\eta$ bin of 2D correlated yield with $2.0 < \eta_{trig} < 2.4$ for high-multiplicity $N_{trk}^{offline} < 20$ pPb collisions at 5.02 TeV. The $p_{\rm T}$ ranges are $0.3 < p_{\rm T}^{\rm trig}, p_{\rm T}^{\rm assoc} < 3$ GeV/c. The data are efficiency corrected.

yield in a $\Delta\phi$ window of $\pi/6$ radian. This minimum yield is treated as the ZYAM background, which is also shown in Figs. 3.5 - 3.8 as the horizontal line.

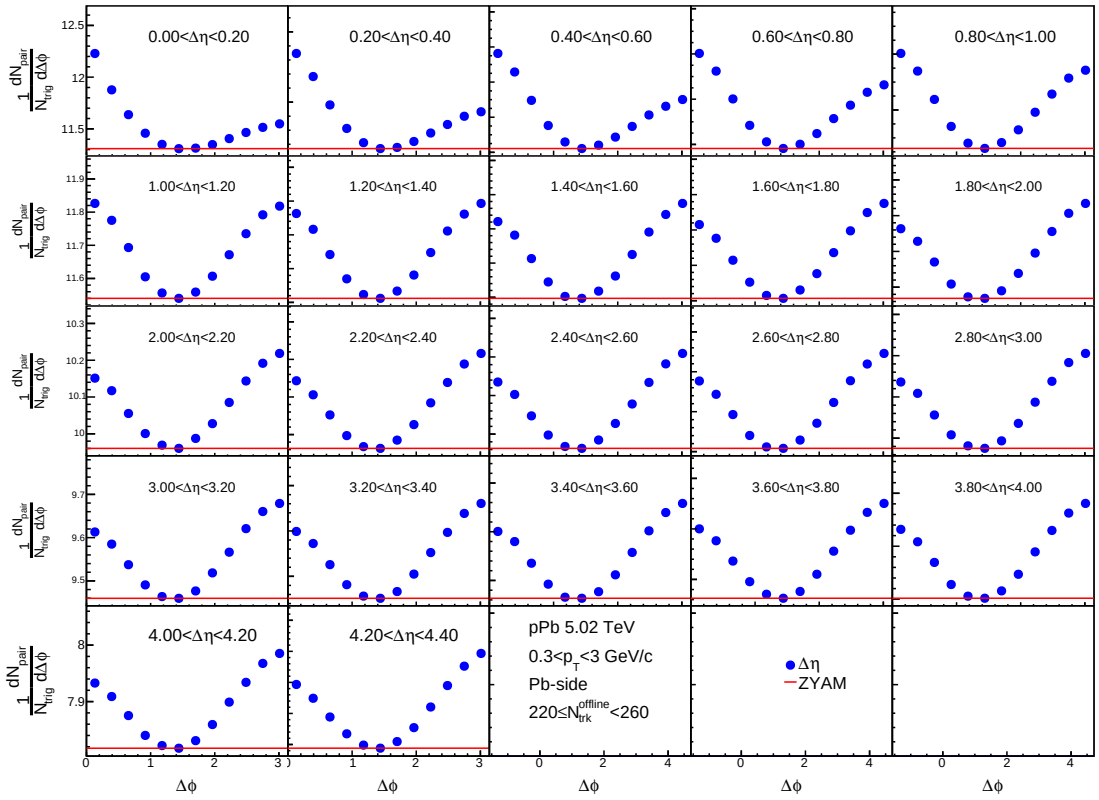

Figure 3.7. $\Delta\phi$ projection of each $\Delta\eta$ bin of 2D correlated yield with $-2.4 < \eta_{trig} < -2.0$ for high-multiplicity $220 \leq N_{trk}^{offline} < 260$ pPb collisions at 5.02 TeV. The $p_{\rm T}$ ranges are $0.3 < p_{\rm T}^{\rm trig}, p_{\rm T}^{\rm assoc} < 3$ GeV/c. The data are efficiency corrected.

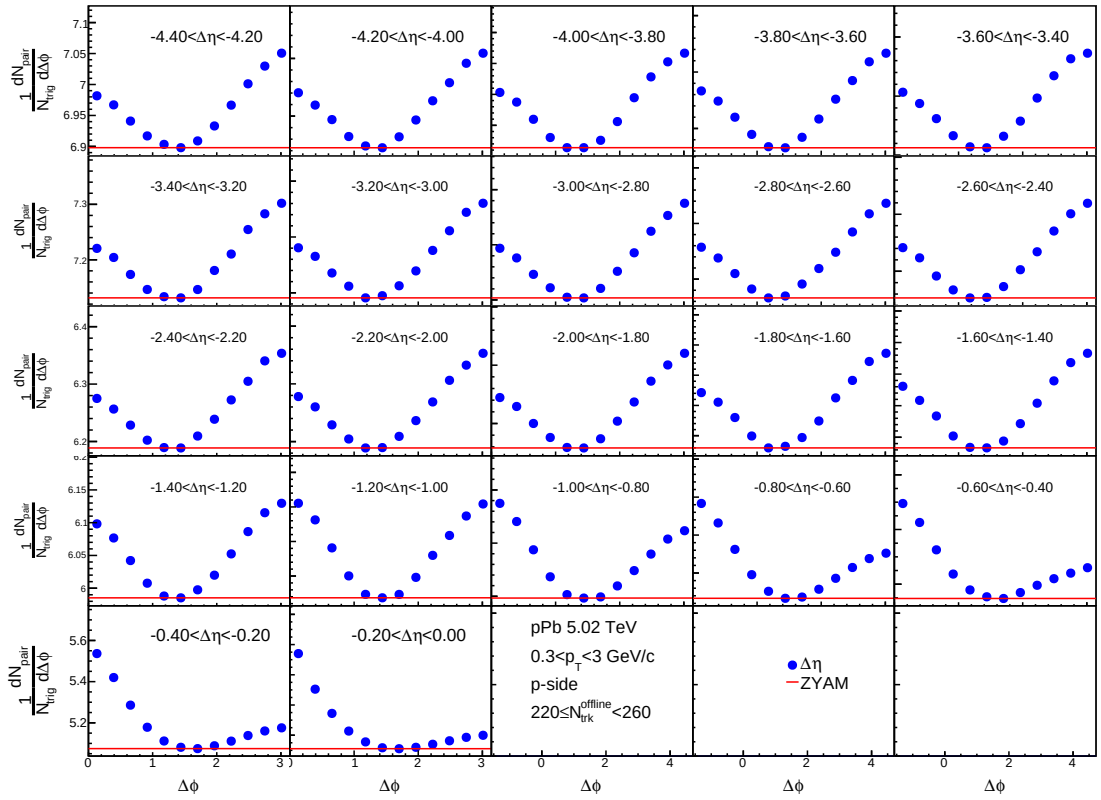

Figure 3.8. $\Delta\phi$ projection of each $\Delta\eta$ bin of 2D correlated yield with $2.0 < \eta_{trig} < 2.4$ for high-multiplicity $220 \leq N_{trk}^{offline} < 260$ pPb collisions at 5.02 TeV. The p_{T} ranges are $0.3 < p_{\mathrm{T}}^{\mathrm{trig}}, p_{\mathrm{T}}^{\mathrm{assoc}} < 3$ GeV/c. The data are efficiency corrected.

To investigate the "ridge" in details and to quantify the "ridge" and jet shapes, near-side and away-side one-dimensional (1-D) distributions in $\Delta\eta$ are found by averaging the correlated yield 2-D distributions over the 2 different $\Delta\phi$ range, which are defined below:

- near-side range: $|\Delta\phi| < \pi/3$
- away-side range: $|\Delta\phi - \pi| < \pi/3$

Figure 3.9 shows 1-D projections in the near-side and away-side $\Delta\phi$ ranges with $-2.4 < \eta_{trig} < -2.0$, $2.4 < \eta_{assoc} < -2.0$, and $0.3 < p_{\mathrm{T}}^{\mathrm{trig}}, p_{\mathrm{T}}^{\mathrm{assoc}} < 3.0$ GeV/c. The ZYAM magnitudes are plotted as the open circles in the figure as well.

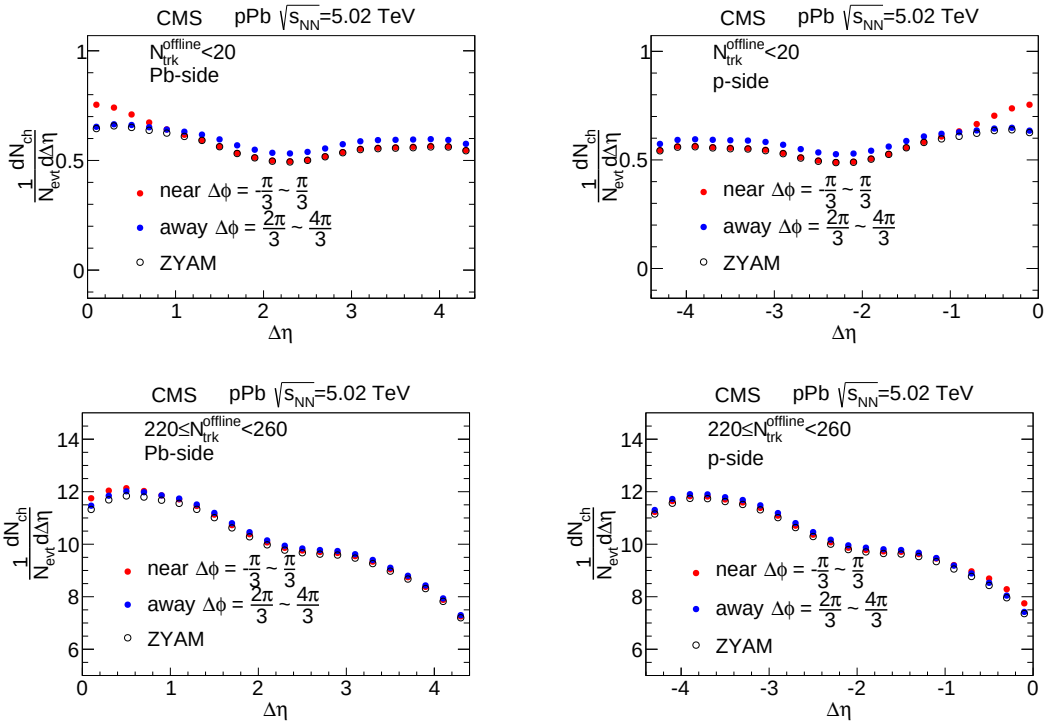

Figure 3.9. Correlated yields for different $|\Delta\phi|$ ranges of correlated yields for Pb-side ($-2.4 < \eta_{trig} < -2.0$, left) and p-side ($2.0 < \eta_{trig} < 2.4$, right) in pPb collisions at 5.02 TeV. The p_{T} ranges are $0.3 < p_{\mathrm{T}}^{\mathrm{trig}}, p_{\mathrm{T}}^{\mathrm{assoc}} < 3.0$ GeV/c. Upper panels are low-multiplicity collisions and lower panels are high-multiplicity collisions.

In low-multiplicity ($N_{trk}^{offline} < 20$) collisions, the near-side $\Delta\eta$ correlations is larger than the ZYAM $\Delta\eta$ correlation at small $\Delta\eta$, as shown in the top plots, but very close to the ZYAM value at large $\Delta\eta$, as shown in the bottom plots. This indicates that the near-side correlation in low-multiplicity pPb is composed of jet only, no ridge. In high-multiplicity collisions, an excess of the near-side correlation above ZYAM is due to the ridge. In both low- and high-multiplicity collisions, the away side is larger than ZYAM because back-to-back jets contribute to the away-side, as shown in the bottom plots of Fig. 3.10.

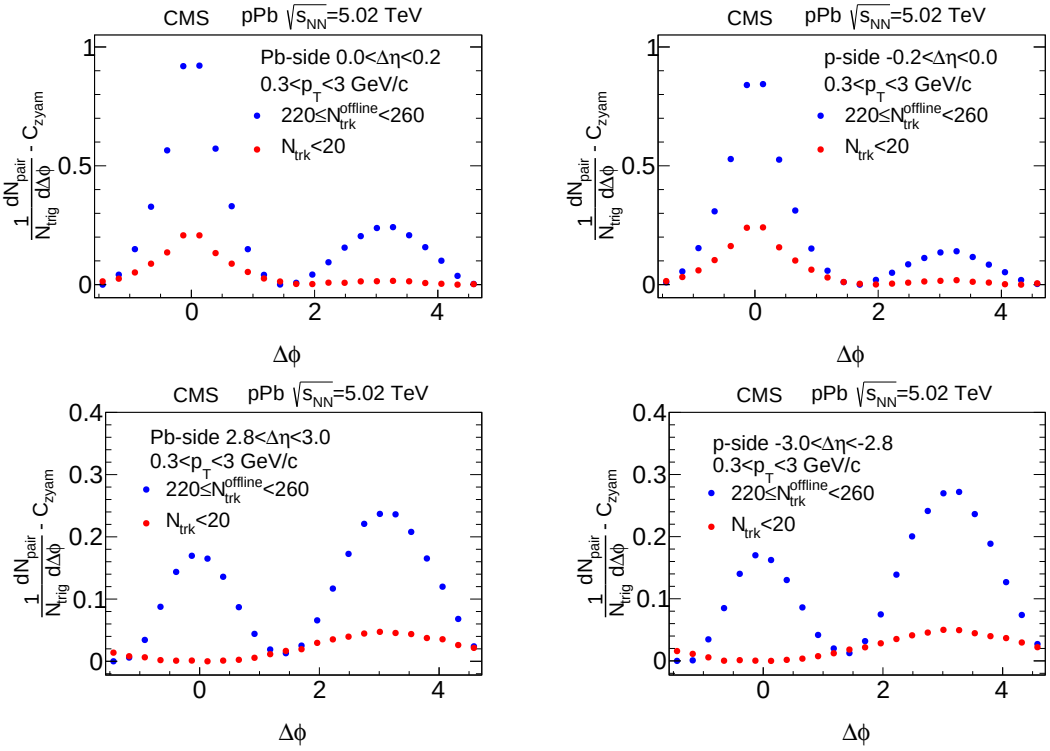

Figure 3.10. Distributions of associated yields after ZYAM subtraction for both low-multiplicity ($2 \leq N_{trk}^{offline} < 20$, red points) and high-multiplicity ($220 \leq N_{trk}^{offline} < 260$, blue points), pPb collisions at 5.02 TeV. The results for Pb-side (left panels) and p-side (right panels) trigger particles are both shown; two $\Delta\eta$ bins are shown: small $\Delta\eta$ in the upper panels and large $\Delta\eta$ in the lower panels. The trigger and associated particle p_{T} ranges are both $0.3 < p_{\mathrm{T}} < 3$ GeV/c.

After ZYAM subtraction, the signal will be zero at the minimum. Example $\Delta\phi$ distributions in high-multiplicity and low-multiplicity collisions are depicted in Fig. 3.10 for two, short- and long-range, $\Delta\eta$ bins.

3.3.2 Fit the near-side jet and ridge

Figure 3.11 shows the near-side range projection after subtracting the ZYAM range projection with η_{trig} in (2.0,2.4) and (-2.4,-2.0) range. In the high multiplicity plots, the peak around $\Delta\eta = 0$ is the near-side jet, and the extensive bump feature at large $\Delta\eta$ is the ridge-like structure.

To decompose jet-like and ridge-like structure and quantify the correlation strength, we fit the high-multiplicity data with the following functional form:

$$\frac{1}{N_{\rm trig}}\frac{dN_{\rm near}(\Delta\eta)}{d\Delta\eta} = \frac{Y\beta}{\sqrt{2}\sigma\Gamma(1/2\beta)}\exp\left[-\left(\frac{\Delta\eta^2}{2\sigma^2}\right)^{\beta}\right]+(C+k\Delta\eta)\times{\rm ZYAM}(\Delta\eta)\,. \quad (3.2)$$

The first term represents the near-side jet; Y is the correlated yield, and σ and β describe the correlation shape. A simple Gaussian was found inadequate to describe the jet-like peak, nor was an exponential. A generalized Gaussian form as in Eq. 3.3 was found to describe the data well. The $\frac{N\beta}{\sigma\Gamma(\beta/2)}$ part is normalization factor, σ is the width of the jet peak and Y is the jet correlated yield that quantify the amplitude of the jet. Fit results of low-multiplicity collisions are shown in the upper panel of Fig. 3.11. The fit parameters are written on the plots. The fitted pedestal is slight negative, indicating that the ZYAM is an overestimate of the underlying background. (Note: the ZYAM values at $|\Delta\eta| > 2$ for low-multiplicity collisions are average of the raw signal within $0.91 < |\Delta\phi| < 1.41$.)

The second term on the right-hand side of Eq. (3.2) represents the ridge structure. Since the ridge is wide in $\Delta\eta$ and may be related to the bulk medium, its shape is modeled as dominated by the underlying event magnitude, ZYAM($\Delta\eta$). However, the background shape multiplied by a constant is not adequate to describe the ridge in high multiplicity events. Instead, the background shape multiplied by a linear function in $\Delta\eta$, as in Eq. (3.2), can fit the data well, with reasonable χ^2/ndf (where

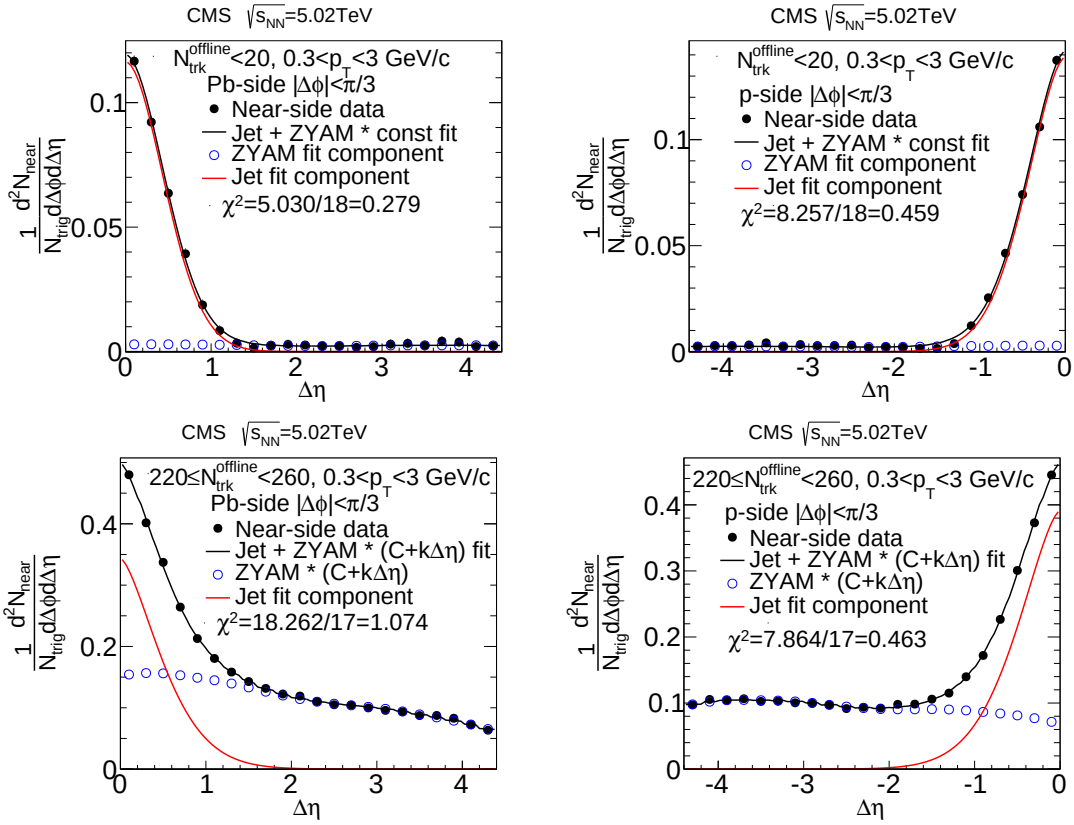

Figure 3.11. Near-side correlated yield after ZYAM subtraction for low-multiplicity $2 \leq N_{trk}^{offline} < 20$ (upper panels) and high-multiplicity $220 \leq N_{trk}^{offline} < 260$ (lower panels). The correlated yields are fit by Eq.(3.3) for low-multiplicity data and by Eq.(3.2) for high-multiplicity data. Data are 5.02 TeV pPb collisions for pairs of charged particles with $0.3 < p_{\mathrm{T}}^{\mathrm{trig}}, p_{\mathrm{T}}^{\mathrm{assoc}} < 3$ GeV/c, and trigger particle η windows of Pb-side ($-2.4 < \eta_{trig} < -2.0$, left) and p-side ($2.0 < \eta_{trig} < 2.4$, right).

ndf is the number of degree of freedom) (see Table 3.2). Here C quantifies the overall strength of the ridge yield relative to the underlying event, and k indicates the $\Delta\eta$ dependence of the ridge in addition to that of the underlying event.

The low-multiplicity data is composed of jet only; no ridge is observed. We, therefore, fit the low-multiplicity data with

$$\frac{1}{N_{\mathrm{trig}}}\frac{dN_{\mathrm{near}}(\Delta\eta)}{d\Delta\eta} = \frac{Y\beta}{\sqrt{2}\sigma\Gamma(1/2\beta)}\exp\left[-\left(\frac{\Delta\eta^2}{2\sigma^2}\right)^{\beta}\right] + C \times \mathrm{ZYAM}(\Delta\eta)\,. \qquad (3.3)$$

Similarly to Eq.(3.2), the first term represents the near-side jet. Besides jet there should not be any other contribution. The second term is to correct the uncertainty from the ZYAM subtraction.

Fit results of high-multiplicity collisions are shown in the lower panels of Fig. 3.11 The fitting parameters are also shown on the graphs. Comparing the Y parameter in the fit result, the jet correlated yield in high-multiplicity collision is larger than in low-multiplicity collision. This is likely due to multiplicity biases: jets contribute to the overall multiplicity of the event, and selecting high multiplicity events biases jets to have a larger correlated yield.

The fitted parameters are summarized in Table 3.2. We use a scaling factor α to quantify the jet yield ratio of high-multiplicity to low-multiplicity collisions which is from fit parameter Y. This factor will be used in low-multiplicity subtraction in the V_n calculation.

$$\begin{aligned} \alpha = Y_{220\leq \mathrm{N}_{\mathrm{trk}}^{\mathrm{offline}}<260} / Y_{\mathrm{N}_{\mathrm{trk}}^{\mathrm{offline}}<20} &= 3.08 \pm 0.11^{+0.96}_{-0.31} \text{for Pb-side triggers.} \\ &\quad 3.13 \pm 0.09^{+0.28}_{-0.28} \text{for p-side triggers.} \end{aligned}$$

3.3.3 η-dependence of the azimuthal anisotropy

If the ridge is of hydrodynamic origin, where all pairs are responsible for enhanced/depleted emission at certain azimuthal angles, the natural observable would be the Fourier coefficients, V_n, of two-particle azimuthal correlations and the inferred single-particle anisotropic parameters, v_n.

To obtain the two-particle harmonics, for each $\Delta\eta$ bin, the azimuthal anisotropy harmonics, V_n can be calculated from the two-particle correlation $\Delta\phi$ distribution, as

$$V_n = \langle \cos n\Delta\phi \rangle, \tag{3.4}$$

where $\Delta\phi$ is the azimuthal angle difference between trigger and associated particles. The $\langle\rangle$ means averaging over all particle pairs. At large $\Delta\eta$, near-side jet contribution

Table 3.2
Summary of fit parameters for low- and high-$N_{trk}^{offline}$ ranges in pPb collisions.

$N_{trk}^{offline} < 20$		
Parameter	Pb-side trigger	p-side trigger
Y	0.130 ± 0.003	0.156 ± 0.003
σ	0.445 ±0.011	0.446 ± 0.010
β	0.943 ± 0.057	0.870 ±0.043
C	0.0045 ±0.0009	0.0045 ± 0.0010
k	0 (Fixed)	0 (Fixed)
χ^2/ndf	0.279	0.459
$220 \leq N_{trk}^{offline} < 260$		
Parameter	Pb-side trigger	p-side trigger
Y	0.401 ± 0.011	0.489 ± 0.011
σ	0.457 ± 0.008	0.492 ±0.007
β	0.757 ±0.003	0.782 ± 0.025
C	0.0137 ± 0.0004	0.0098 ±0.0004
k	- 0.0011 ± 0.0001	0.0002 ± 0.0001
χ^2/ndf	1.074	0.463

is minimized, but the away-side jet still contributes. The jet contributions may be significantly reduced or eliminated by subtracting the low-multiplicity collision data, via [35]

$$V_n^{\rm sub} = V_n^{220\leq {\rm N}_{\rm trk}^{\rm offline}<260} - V_n^{{\rm N}_{\rm trk}^{\rm offline}<20} \times \frac{N_{\rm assoc}^{{\rm N}_{\rm trk}^{\rm offline}<20}}{N_{\rm assoc}^{220\leq {\rm N}_{\rm trk}^{\rm offline}<260}} \times \alpha\,. \tag{3.5}$$

Here $N_{\rm assoc}^{\rm cent}$ and $N_{\rm assoc}^{\rm peri}$ are the associated particle multiplicities in a given η bin, and $V_n^{\rm cent}$ and $V_n^{\rm peri}$ are the Fourier coefficients in high- and low-multiplicity collisions, respectively. This procedure to extract V_n is tested by studying the pPb collisions generated by HIJING model, where there are no final state interactions, and it will be discussed in section 3.4.10. The measured $V_2^{\rm sub}$ value after subtraction is found to be within 5% difference from the input value.

3.4 Systematics and Cross Checks

Systematic uncertainties on the Fourier coefficients V_n and the relative anisotropic parameter, $v_n(\eta)/v_n(0)$ were estimated for several sources [35]: 1) The effect from the track quality cuts is studied by comparing loose and tight cuts. 2) The bias in the event selection from the HLT trigger is studied by using different Multiplicity trigger filters. 3) The effect from pileup is studied by restricting one vertex per event, and 4) event-vertex position by studying different z vertex range. The effect of reversing beam direction is studied, which could be important for the η dependence of the results on the asymmetric pPb system. However it may originate from the same sources that described above, so this systematic uncertainty is not included in the total systematic uncertainties, but is used as a cross check. In the low multiplicity subtraction, the jet ratio parameter α is applied. The systematic errors on the α are assessed by using different fit functions and by varying ZYAM methods. These systematic uncertainties are propagated to the final results of V_n.

The above sources combine to a total of 3.9% and 10% systematic uncertainty on V_2 and V_3 coefficients, respectively, determined without subtraction of signals from low-multiplicity events. For low-multiplicity-subtracted results, the systematic uncertainties are 5.8% and 15%. The systematic uncertainties from track quality cut and jet ratio are correlated between η bins, therefore they cancel in the self-normalized anisotropic parameter, $v_n(\eta)/v_n(0)$. The systematic uncertainties from the other sources are treated as completely independent of η and are propagated in $v_n(\eta)/v_n(0)$. The systematic uncertainties of $v_2(\eta)/v_2(0)$ and $v_3(\eta)/v_3(0)$ without low multiplicity subtraction are 3.6% and 10%. For low-multiplicity-subtracted results, the systematic uncertainties are 5.7% and 14%.

The detailed systematic errors are listed in Table. 3.3. The detailed study of each source is discussed in the following sections (section 3.6.1-3.6.6). The total systematic uncertainty is obtained by the square root of the quadratic sum of each source.

Table 3.3

Summary of relative systematic uncertainties on second and third harmonics azimuthal anisotropy in pPb collisions at $\sqrt{s_{_{NN}}}$=5.02 TeV. "low-mult sub" stands for low-multiplicity subtracted results, while "no sub" stands for no subtraction results.

$220 \leq N_{trk}^{offline} < 260$				
Source	V_2 (no sub)	V_2(low-mult sub)	V_3(no sub)	V_3(low-mult sub)
Track quality cuts	3.0%	3.0%	7.0%	11%
HLT trigger bias	2.0%	2.5%	2.0%	2.5%
Effect from pileups	1.5%	3.0%	3.5%	3.5%
Vertex dependence	0.5%	1.0%	6.0%	9.0%
Jet ratio	–	3.0%	–	3.0%
Total	3.9%	5.8%	10%	15%

3.4.1 Systematics on vertex position dependence

The track acceptance has a slight dependence on the primary vertex position due to different detector geometry. So selecting events based on reconstructed track multiplicity may bias the vertex distribution, since at specific vertex positions the tracking acceptance is higher. In order to enhance the effect to test our understanding, the same analysis is done by restricting the acceptance for track counting further and make the event characterization more sensitive to vertex position. The tracking efficiency and fake rate corrections are applied in this analysis independently of the vertex position. To evaluate systematic uncertainties due to different vertex position, V_2 and V_3 in 5.02 TeV pPb collisions are compared between vertex range of $3 < |z_{vtx}| < 7.5$ cm and $|z_{vtx}| < 3$ cm in Fig. 3.12 and Fig. 3.13, respectively.

The ratio plots of these two vertex range are shown below the comparison plots. The ratio is plotted with error bars propagated from these two sets. The fluctuation in the ratio contains both statistical uncertainties and systematic errors. To disentangle these two sources, we plot the $(Ratio - 1)/E_{stat}$ distribution, in which E^{stat} is the statistical error of the ratio plots. If the fluctuation is only from the statistical uncertainty, this distribution will have $\sigma \approx 1$, and the mean value should be equal to 0.

The histograms and the Gaussian fits are shown in the bottom plots in Figs. 3.12 and 3.13. The RMS value and mean is from the histogram itself, not the fit. Only no subtraction ratio is plotted since the ratio of low multiplicity subtraction has a similar fluctuation. The systematic error has a influence on this distribution in two ways. The first kind of systematic errors adds quadratically to the statistical errors so that the $\sigma(RMS)$ will be larger than 1. This type systematic error E^1_{sys} can be obtained by

$$\sqrt{\frac{E_1^{sys_2}}{E^{stat2}} + 1} = RMS. \tag{3.6}$$

The second type systematic error could cause the mean value shifted from 1, for this error E_2^{sys} we have

$$\frac{E_2^{sys}}{E^{stat}} = mean \tag{3.7}$$

We can estimate the total systematic errors by combining the two type systematic errors quadratically (knowing the statistical error).

$$E^{sys} = E^{stat}\sqrt{mean^2 + RMS^2 - 1} \tag{3.8}$$

The systematic uncertainty is divided by $\sqrt{2}$ because the ratio is between the two subsets, and the default dataset is the addition of these two sets. Using Eq.(3.8), the systematic uncertainty of V_2 with low multiplicity subtraction is 1.0%, and without subtraction is 0.5%. The systematic uncertainty of V_3 with low multiplicity subtraction is 9.0%, and without subtraction is 6.0%. The same systematic errors are quoted for $v_2(\eta)/v_2(0)$ and $v_3(\eta)/v_3(0)$, respectively.

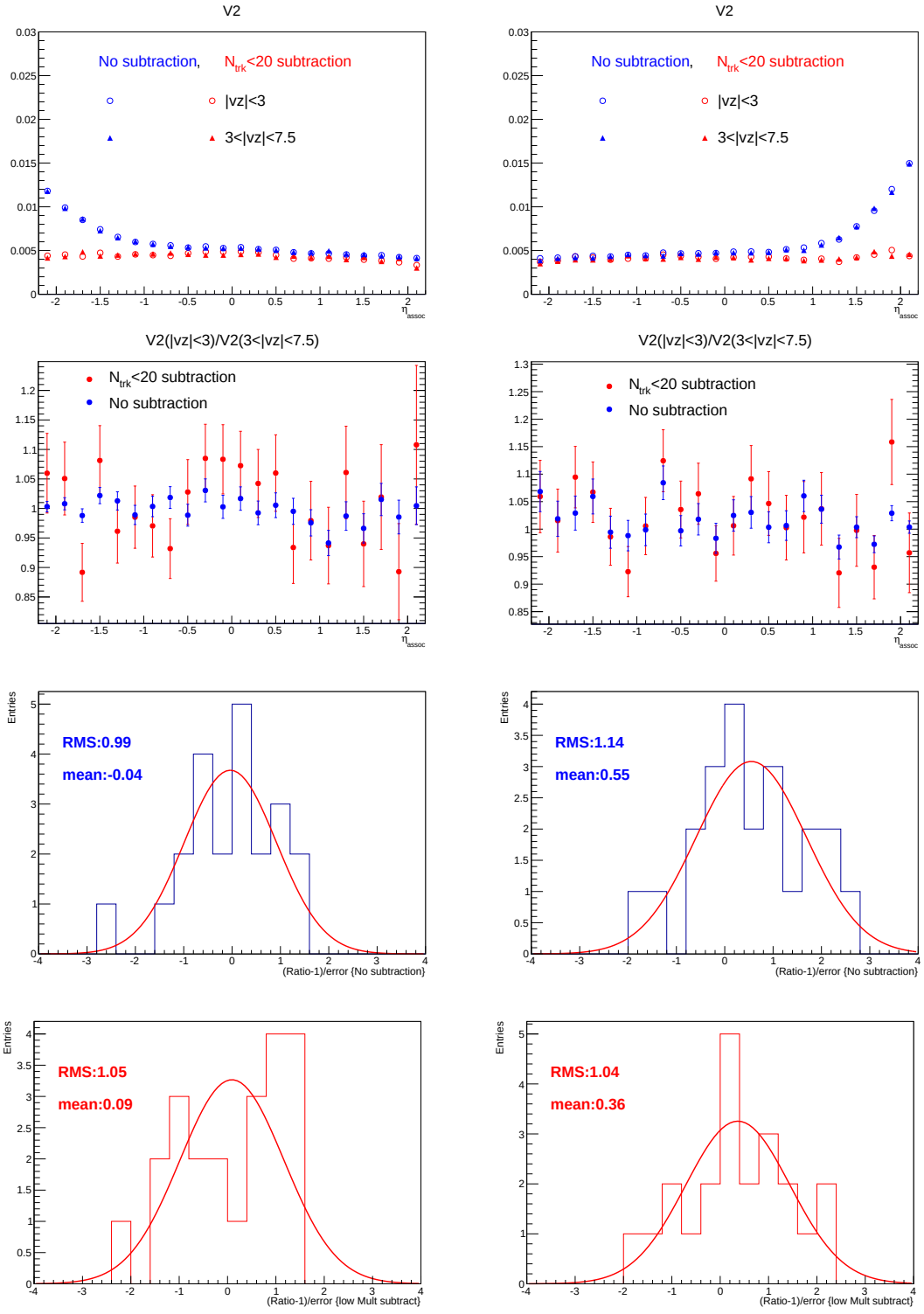

Figure 3.12. Top: Comparison of V_2 in pPb at 5.02 TeV for $3 < |z_{vtx}| < 7.5$ cm and $|z_{vtx}| < 3$ cm vertex range. High- and low-multiplicity events are from the same vertex range, respectively. Left is the Pb-side trigger, right is p-side trigger. V_n is compared for both before and after low multiplicity subtraction. Trigger and associated particle p_{T} are both $0.3 < p_{\mathrm{T}} < 3$ GeV/c. High multiplicity collisions are defined by $220 \leq N_{trk}^{offline} < 260$ and low multiplicity collisions by $2 \leq N_{trk}^{offline} < 20$. Second row: The ratio of $3 < |z_{vtx}| < 7.5$ cm to $|z_{vtx}| < 3$ cm result, before low multiplicity subtraction. Bottom two rows: $(Ratio - 1)/E_{stat}$ distribution of low multiplicity subtraction and no subtraction.

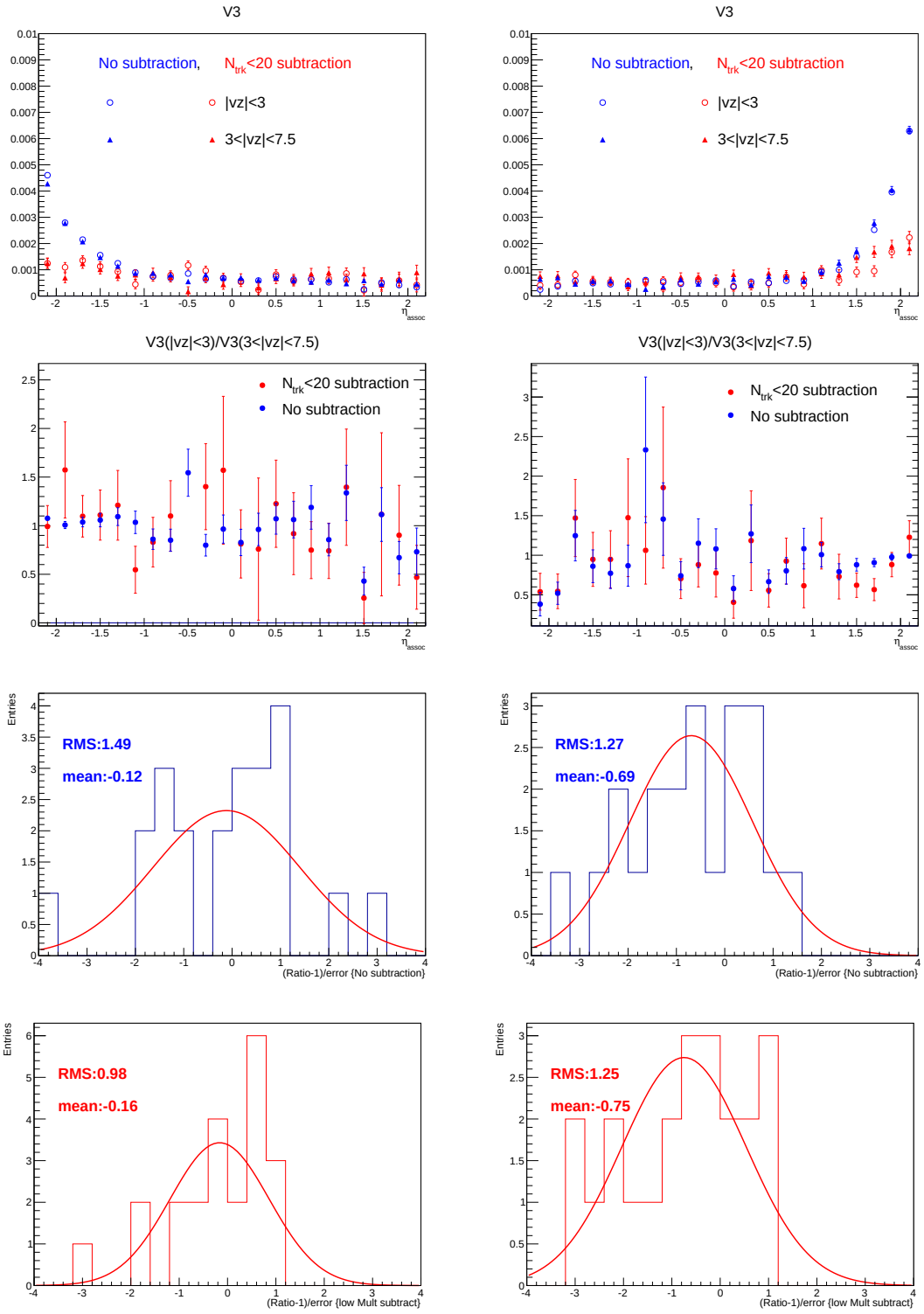

Figure 3.13. Top: Comparison of V_3 in pPb at 5.02 TeV for $3 < |z_{vtx}| < 7.5$ cm and $|z_{vtx}| < 3$ cm vertex range. High- and low-multiplicity events are from the same vertex range, respectively. Left is the Pb-side trigger, right is p-side trigger. V_n is compared for both before and after low multiplicity subtraction. Trigger and associated particle p_{T} are both $0.3 < p_{\mathrm{T}} < 3$ GeV/c. High multiplicity collisions are defined by $220 \leq N_{trk}^{offline} < 260$ and low multiplicity collisions by $2 \leq N_{trk}^{offline} < 20$. Second row: The ratio of $3 < |z_{vtx}| < 7.5$ cm to $|z_{vtx}| < 3$ cm result, before low multiplicity subtraction. Bottom two rows: $(Ratio - 1)/E_{stat}$ distribution of low multiplicity subtraction and no subtraction.

3.4.2 High Multiplicity HLT trigger bias

In this section, two different High Multiplicity HLT triggers HLT_PAPixelTracks_Multiplicity190_v1 and HLT_PAPixelTracks_Multiplicity160_v1 are selected and applied in the V_n study.

One dataset is selected by HLT_PAPixelTracks_Multiplicity190_v1 only, while the other events set is selected by HLT_PAPixelTracks_Multiplicity190_v1 only. As a result, errors for the two sets are independent of each other, therefore, the errors on the ratio plots of Figs. 3.4.2 and 3.4.2 are from the top plots.

As discussed in Section 3.4.1, systematic and statistical errors can be disentangled by studying the $(Ratio - 1)/E_{stat}$ distribution. As shown in Figs .3.4.2 and 3.4.2, the estimated systematic uncertainty of HLT trigger on two-particle harmonics for V_2 with low multiplicity subtraction is 2.5%, and without subtraction is 2.0%. For V_3 the error with low multiplicity subtraction is 2.5%, and without subtraction is 2.0%. The same errors are quoted for the self-normalized $v_n(\eta)/v_n(0)$,

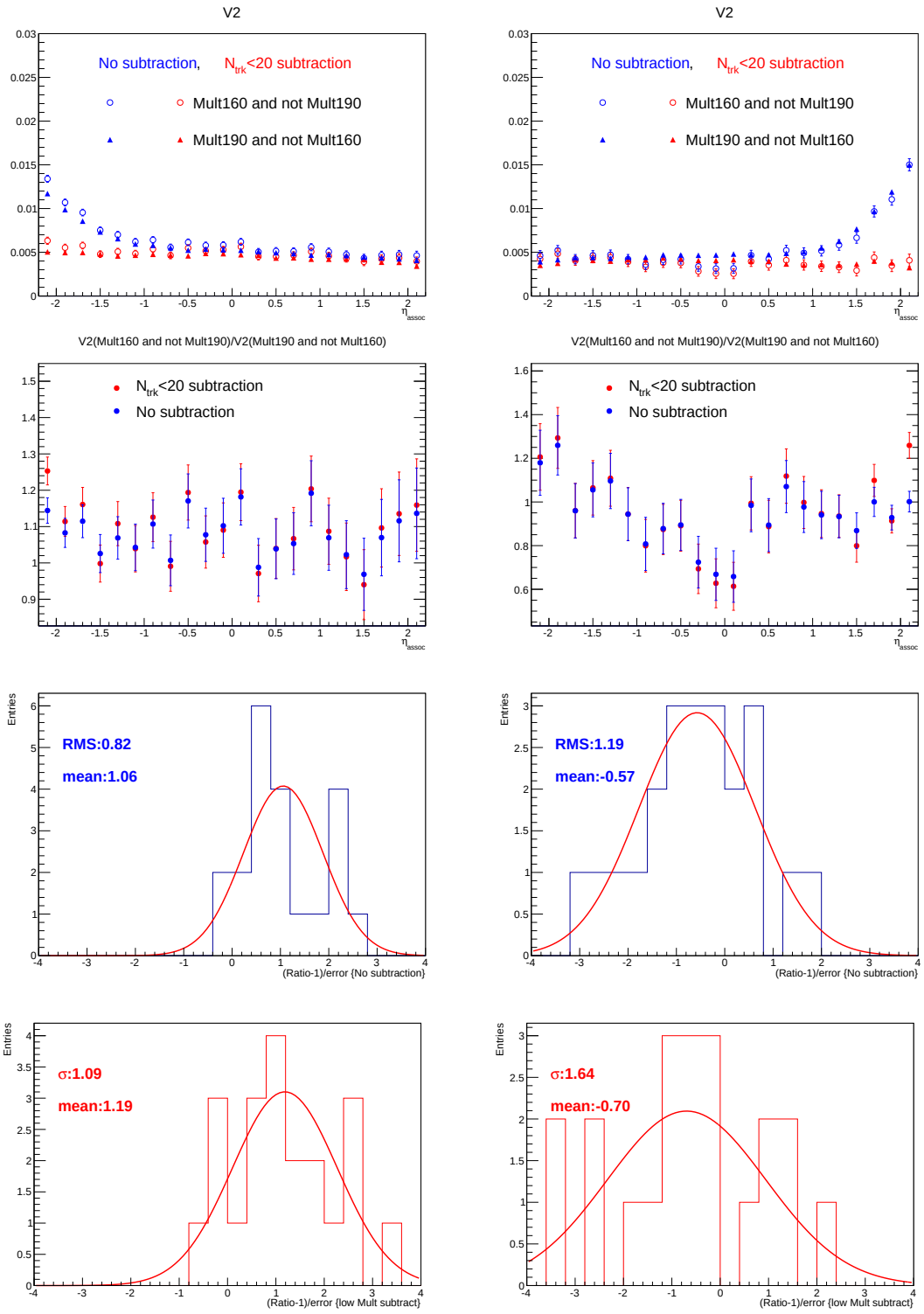

Figure 3.14. Top: Comparison of V_2 in pPb collisions at 5.02 TeV for Multiplicity190_v1 trigger only events and Multiplicity160_v1 triggers only events. Left is the Pb-side trigger, right is p-side trigger. V_n is compared for both before and after low multiplicity subtraction. Trigger and associated particle p_{T} are both $0.3 < p_{\mathrm{T}} < 3$ GeV/c. High multiplicity collisions are defined by $220 \leq N_{trk}^{offline} < 260$ and low multiplicity collisions by $2 \leq N_{trk}^{offline} < 20$. Second row: The ratio of Multiplicity190_v1 and Multiplicity160_v1 to default value, with low multiplicity subtraction. Bottom: $(Ratio-1)/E_{stat}$ distribution of low multiplicity subtraction and no subtraction.

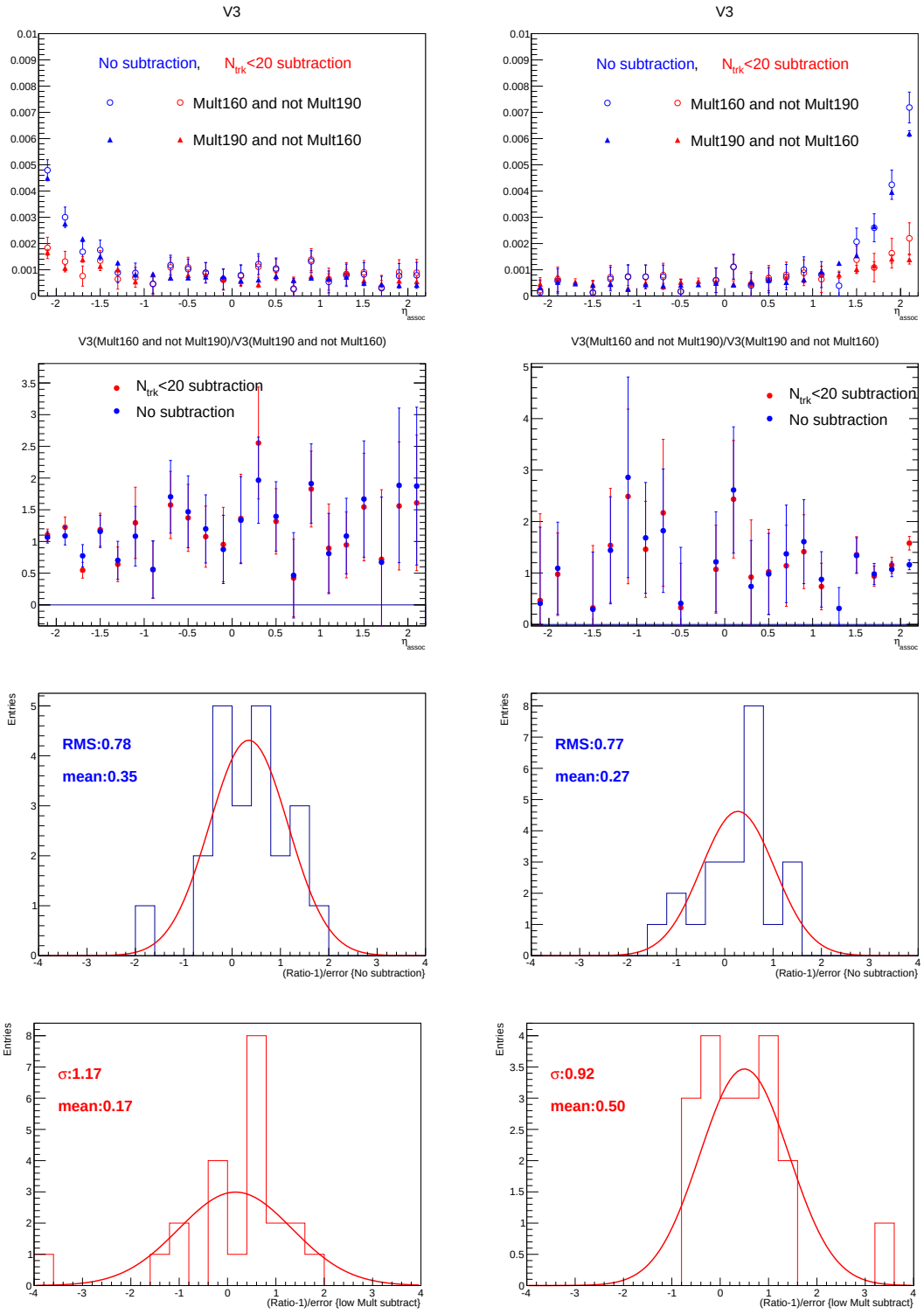

Figure 3.15. Top: Comparison of V_3 in pPb collisions at 5.02 TeV for Multiplicity190_v1 trigger only events and Multiplicity160_v1 triggers only events. Left is the Pb-side trigger,. Left is the Pb-side trigger, right is p-side trigger. V_n is compared for both before and after low multiplicity subtraction. Trigger and associated particle p_{T} are both $0.3 < p_{\mathrm{T}} < 3$ GeV/c. High multiplicity collisions are defined by $220 \leq N_{trk}^{offline} < 260$ and low multiplicity collisions by $2 \leq N_{trk}^{offline} < 20$. Second row: The ratio of Multiplicity190_v1 and Multiplicity160_v1 to default value, with low multiplicity subtraction. Bottom: $(Ratio - 1)/E_{stat}$ distribution of low multiplicity subtraction and no subtraction.

3.4.3 Systematics on track quality cuts

To estimate the uncertainty of track quality cuts, a set of tighter and looser track quality cuts are tested on the data:

Tight selections:

- $dz/dz_{err} < 2$
- $dxy/dxy_{err} < 2$
- $\sigma(p_T)/p_T < 0.05$.

Loose selections:

- $dz/dz_{err} < 5$
- $dxy/dxy_{err} < 5$.

The same efficiency table is used for different track quality cuts. After changing the track quality cuts, the definition of event multiplicity remains unchanged, since the multiplicity counting is still based on the default track quality cuts. After obtaining results from different track quality cuts, the calculated Fourier harmonics are compared.

The results are shown in Figs. 3.16 - 3.19. As in Section 3.4.5, the loose cuts and tight cuts are applied on the same events, so the statistical uncertainty does not contribute to the fluctuation of the ratio (of tight and loose cuts). Thus the systematic uncertainty can be directly obtained from the distribution.

Considering the mean value shifted from 1 and the RMS value of the ratio distribution, the systematic errors for V_2 with low multiplicity subtraction is 3.0%, and without subtraction is 3.0%. And the systematic errors for V_2 with low multiplicity subtraction is 11.0%, and without subtraction is 7.0%.

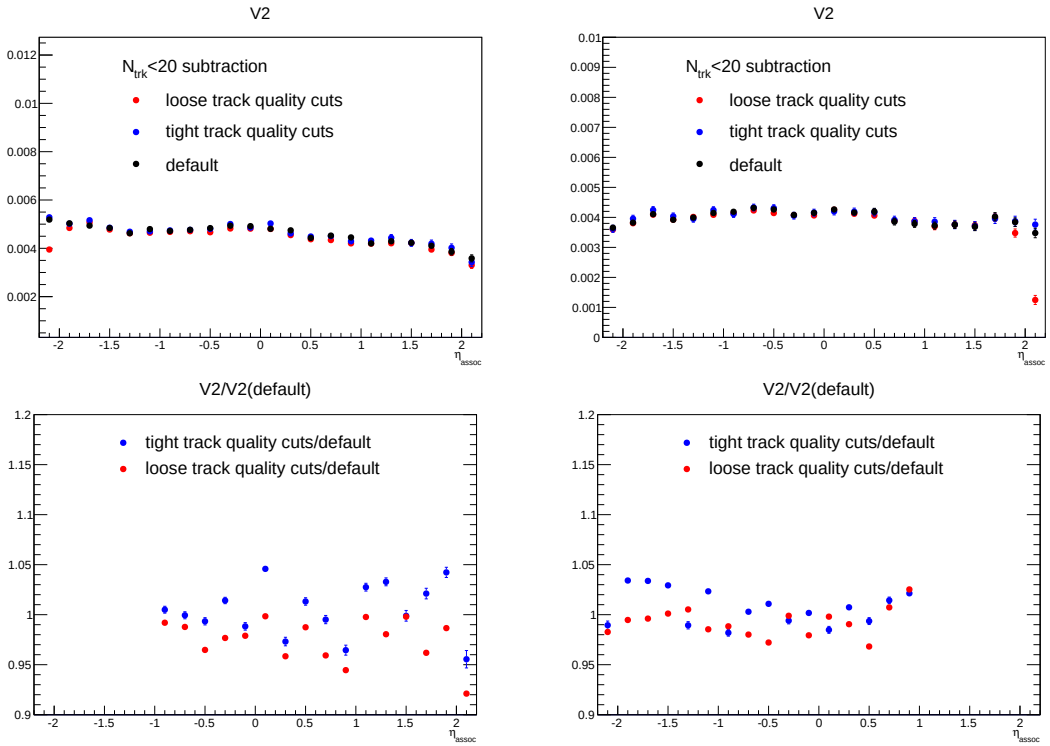

Figure 3.16. Top: Comparison V_2 in pPb collision at 5.02 TeV for loose cuts and tight cuts with low multiplicity subtraction. Left is the Pb-side trigger, right is p-side trigger. V_2 is compared for both before and after low multiplicity subtraction. Trigger and associated particle p_{T} values are both $0.3 < p_{\mathrm{T}} < 3$ GeV/c. High multiplicity collisions are defined by $220 \leq N_{trk}^{offline} < 260$ and low multiplicity collisions by $2 \leq N_{trk}^{offline} < 20$. Bottom: Ratios of loose cuts to default and tight cuts to default, with low multiplicity subtraction.

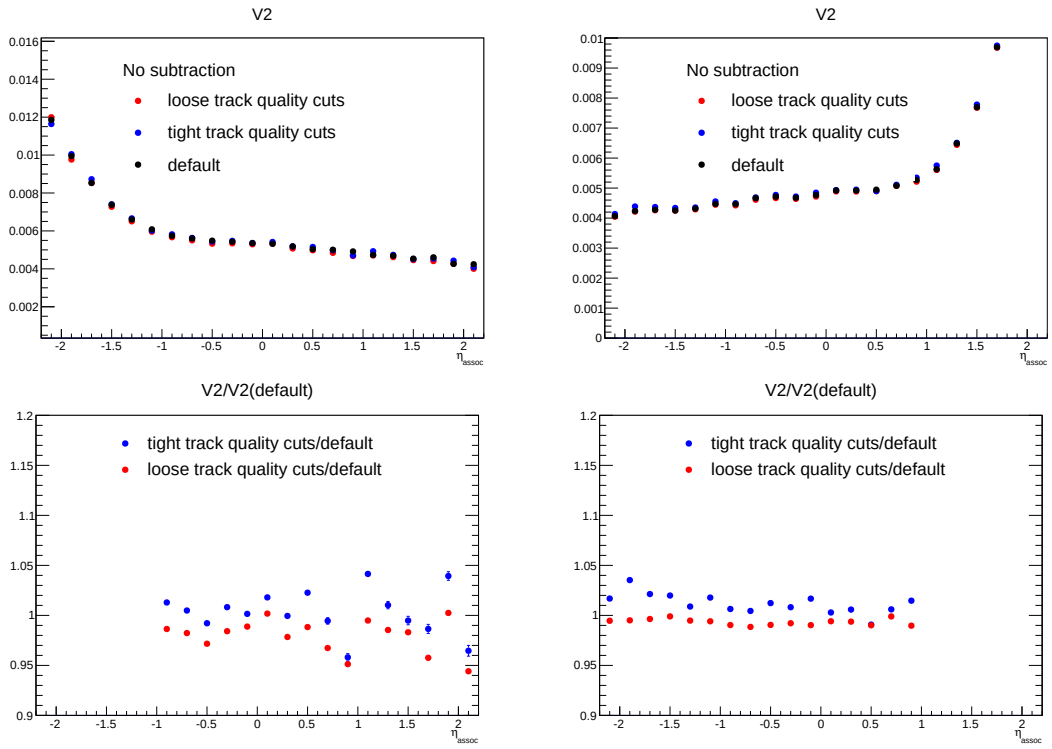

Figure 3.17. Top: Comparison V_2 in pPb collision at 5.02 TeV for loose cuts and tight cuts without low multiplicity subtraction. Left is the Pb-side trigger, right is p-side trigger. V_2 is compared for both before and after low multiplicity subtraction. Trigger and associated particle p_{T} values are both $0.3 < p_{\mathrm{T}} < 3$ GeV/c. High multiplicity collisions are defined by $220 \leq N_{trk}^{offline} < 260$. Bottom: Ratios of loose cuts to default and tight cuts to default, without low multiplicity subtraction.

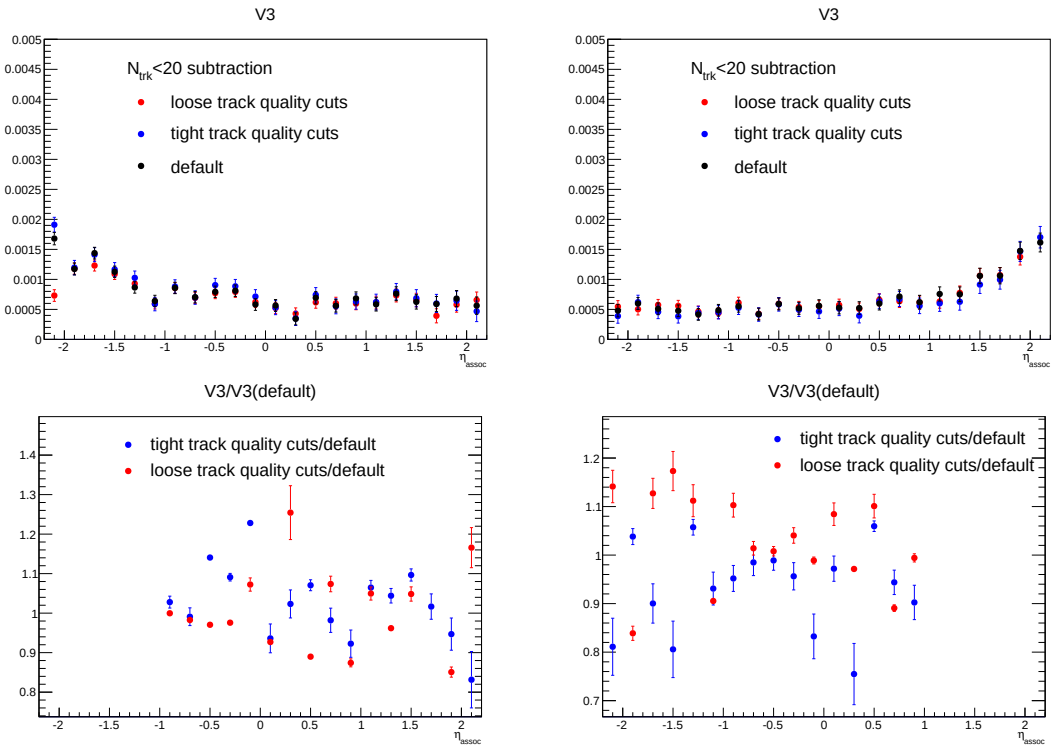

Figure 3.18. Top: Comparison of V_3 in pPb collision at 5.02 TeV for loose cuts and tight cuts with low multiplicity subtraction. Left is the Pb-side trigger, right is p-side trigger. V_2 is compared for both before and after low multiplicity subtraction. Trigger and associated particle p_{T} values are both $0.3 < p_{\mathrm{T}} < 3$ GeV/c. High multiplicity collisions are defined by $220 \leq N_{trk}^{offline} < 260$ and low multiplicity collisions by $2 \leq N_{trk}^{offline} < 20$. Bottom: Ratios of loose cuts to default and tight cuts to default, with low multiplicity subtraction.

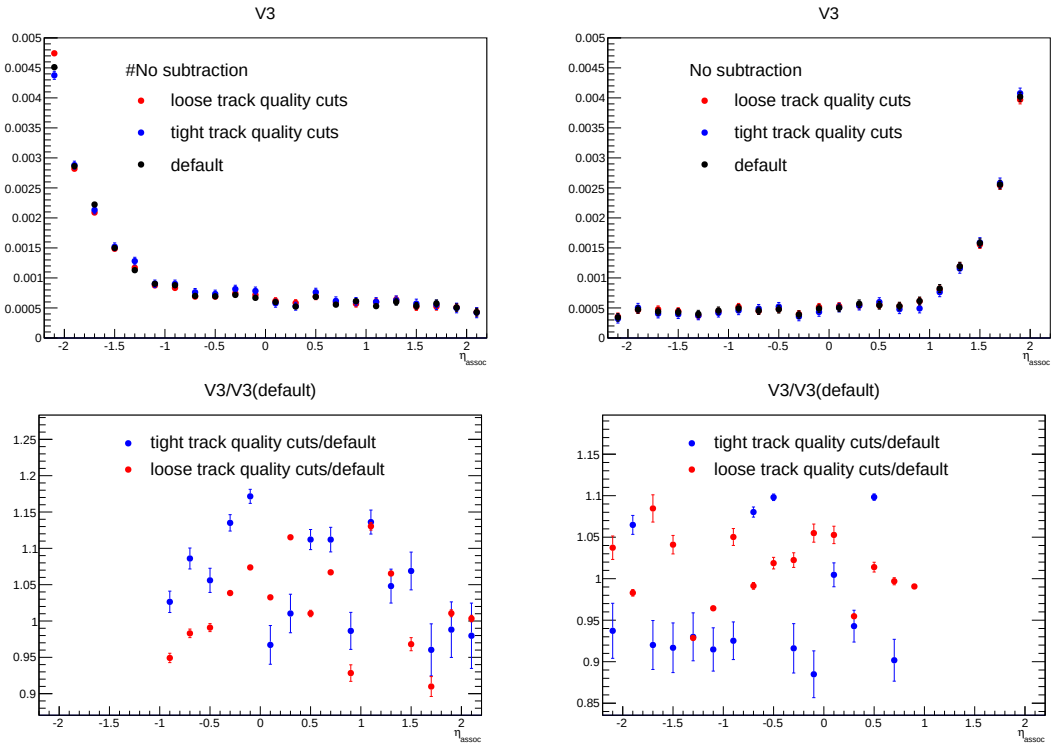

Figure 3.19. Top: Comparison of V_3 in pPb collision at 5.02 TeV for loose cuts and tight cuts without low multiplicity subtraction. Left is the Pb-side trigger, right is p-side trigger. V_2 is compared for both before and after low multiplicity subtraction. Trigger and associated particle p_{T} values are both $0.3 < p_{\mathrm{T}} < 3$ GeV/c. High multiplicity collisions are defined by $220 \leq N_{trk}^{offline} < 260$. Bottom: Ratios of loose cuts to default and tight cuts to default, without low multiplicity subtraction.

3.4.4 Systematic study pileup effects

It is quite possible that one single bunch crossing may produce several separate events, so-called "pileup" events. During the pPb run of 2013, the estimated pileup was considerably higher than the 2012 pilot run and, and since we are mainly interested in very high multiplicity events, it is crucial to make sure they are not resulted from multiple interactions. The pileup rejection is applied in the dataset for this analysis. However, to investigate potential residual pileup effect, especially for very high multiplicity events, we repeat the analysis by requiring only one reconstructed vertex to be present in the event. This will result in the some loss of good single collision events that have split reconstructed vertices but no real pileup collisions. It is an extreme way of removing pileup events and checking the systematic uncertainty by comparing to the rest of the data, which are the events with more than one vertex.

As discussed in Section 4.3, the systematic study can be calculated via Eq.(3.8). The systematic uncertainty on V_2 with low multiplicity subtraction is 3.0%, and without subtraction is 1.5%. The systematic uncertainty on V_3 with low multiplicity subtraction is 3.5%, and without subtraction is 3.5%. The details are shown in Figs. 3.4.4 and 3.21. The same systematic uncertainties are quoted for $v_2(\eta)/v_2(0)$ and $v_3(\eta)/v_3(0)$.

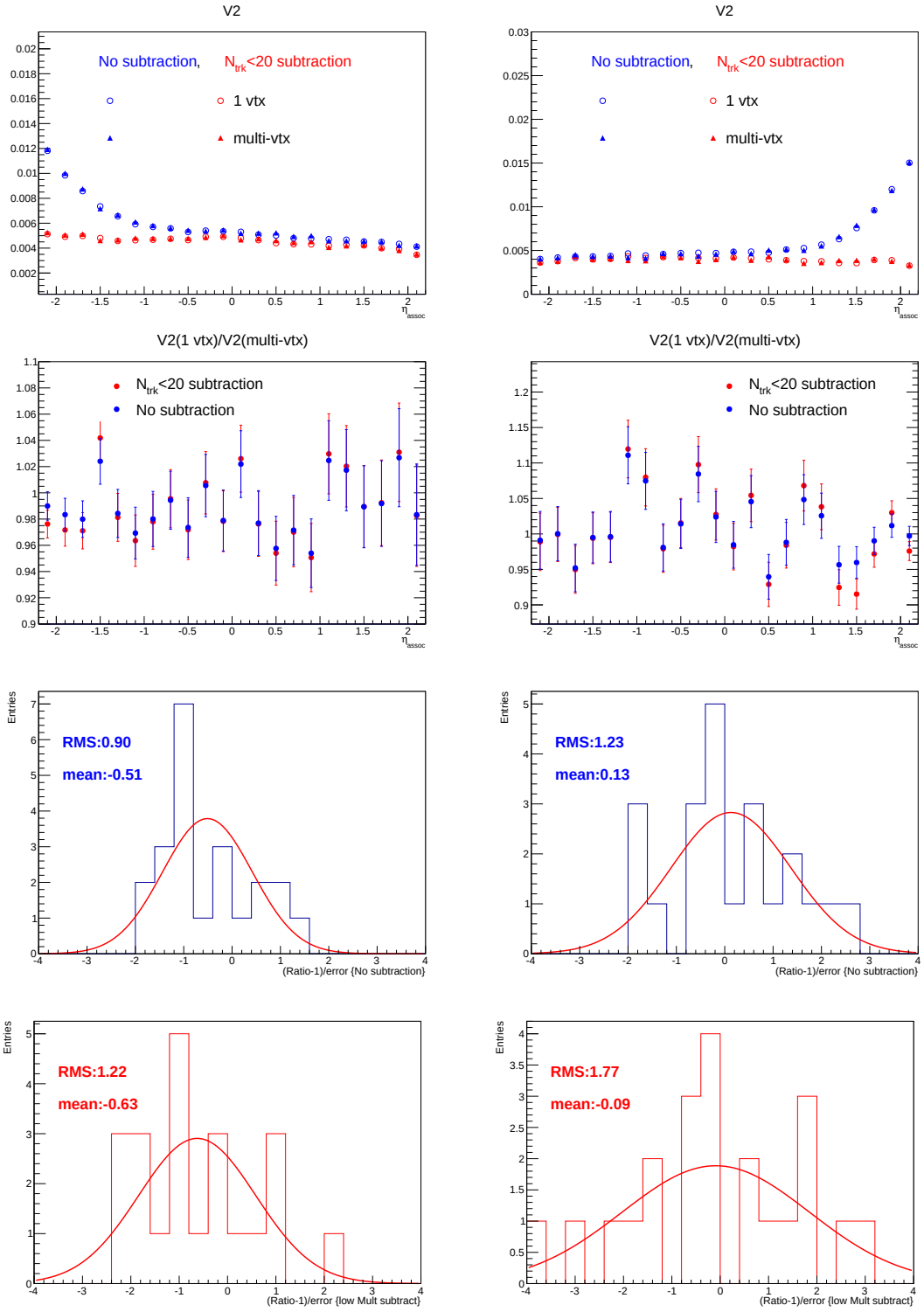

Figure 3.20. Top: Comparison of V_2 in pPb collision at 5.02 TeV for 1 events and multi-vertex events. Left is the Pb-side trigger, right is p-side trigger. V_n is compared for both before and after low multiplicity subtraction. Trigger and associated particle p_{T} are both $0.3 < p_{\mathrm{T}} < 3$ GeV/c. High multiplicity collisions are defined by $220 \leq N_{trk}^{offline} < 260$ and low multiplicity collisions by $2 \leq N_{trk}^{offline} < 20$. Second row: The ratio of V_2 of single-vertex events to V_2 of multiple-vertex events, without low multiplicity subtraction. Bottom: $(Ratio - 1)/E_{stat}$ distribution of low multiplicity subtraction and no subtraction.

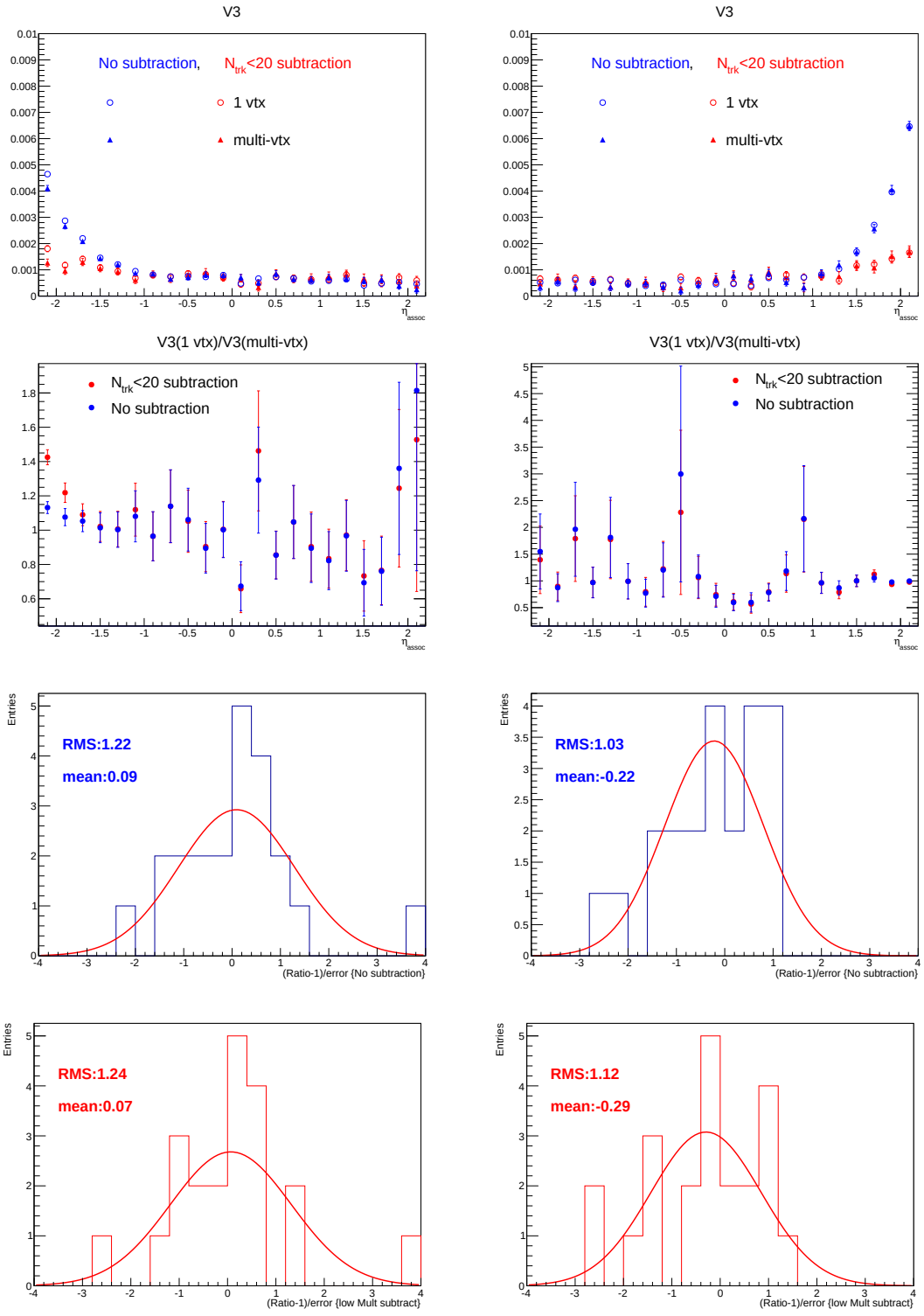

Figure 3.21. Top: Comparison of V_3 in pPb collision at 5.02 TeV for 1 events and multi-vertex events. Left is the Pb-side trigger, right is p-side trigger. V_n is compared for both before and after low multiplicity subtraction. Trigger and associated particle p_{T} are both $0.3 < p_{\mathrm{T}} < 3$ GeV/c. High multiplicity collisions are defined by $220 \leq N_{trk}^{offline} < 260$ and low multiplicity collisions by $2 \leq N_{trk}^{offline} < 20$. Second row: The ratio of V_3 of single-vertex events to V_3 of multiple-vertex events, without low multiplicity subtraction. Bottom: $(Ratio - 1)/E_{stat}$ distribution of low multiplicity subtraction and no subtraction.

3.4.5 Systematic uncertainties from near-side jet ratio

We used a generalized Gaussian function to fit the near-side jet shape, see Eqs.(3.2) and (3.3). To describe ridge structure, a linear function times ZYAM pedestal is favored, as discussed in Section 3.4. In this section, different functional forms for near-side fit were applied to study the systematic uncertainty. The fit function will influence the jet ratio used in the low multiplicity subtraction for V_n. The technique of low-multiplicity subtraction is described in Section 3.5.

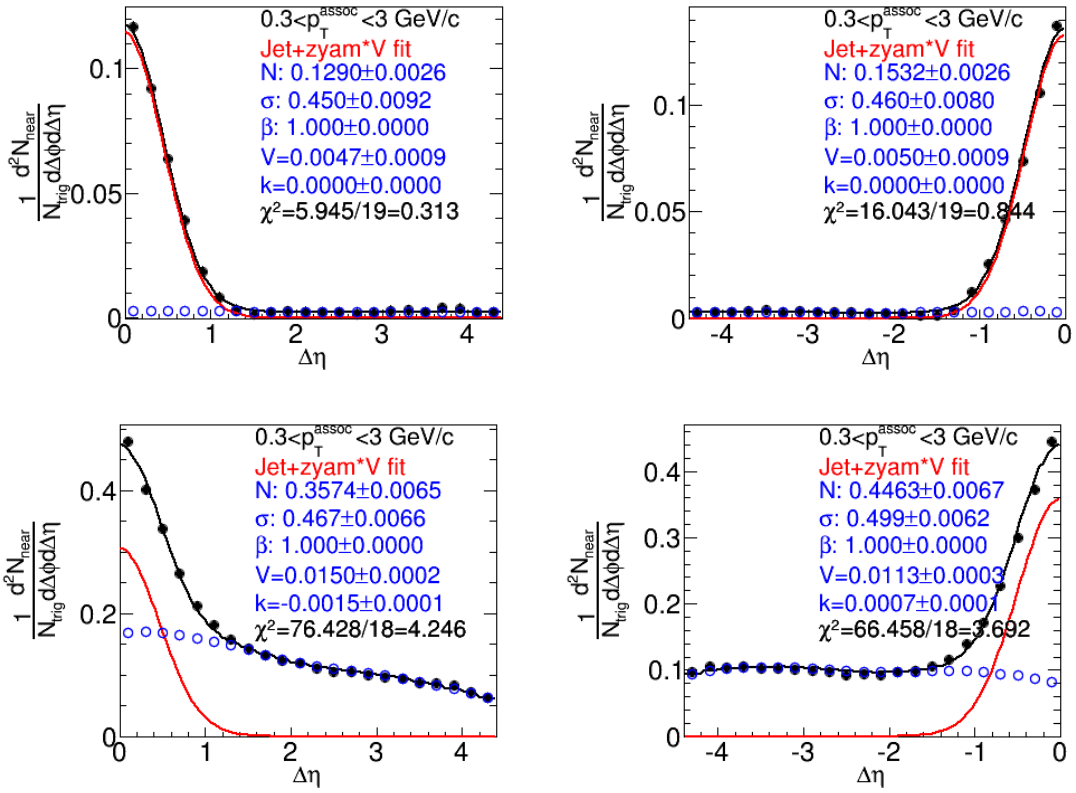

Figure 3.22. Gaussian plus linear function scaled ZYAM fit functions of near-side jet plus ridge with the fit parameters on the plots.

Two different fit functions for near-side projection is applied and shown in Figs. 3.22 and 3.23. In Fig. 3.22, a Gaussian function plus a linear scaled ZYAM is applied to fit the near-side. A similar function to Eq(.3.2) is used, with $\beta = 1.0$ fixed. While

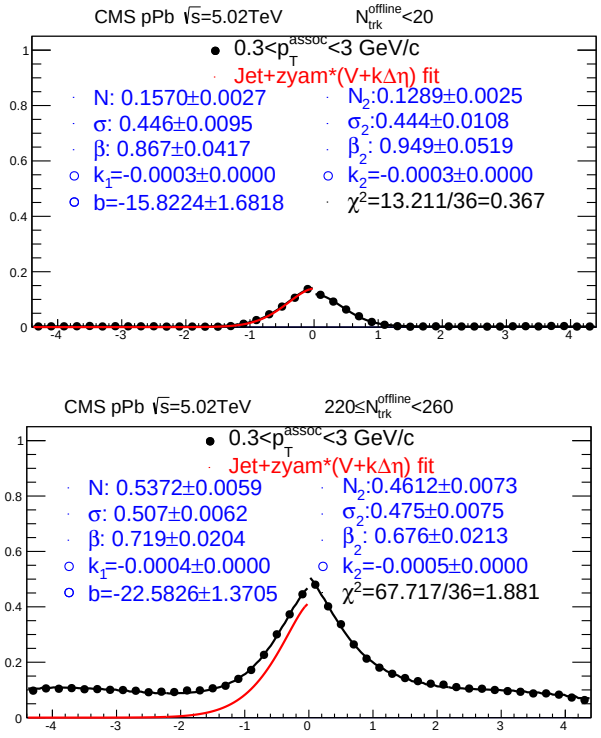

Figure 3.23. Fit p-side and Pb-side together with generalized Gaussian plus linear function scaled ZYAM, with the fit parameters on the plots.

in Fig. 3.23, p-side and Pb-side are fitted together assuming the ridge is related to hydrodynamics, so the ridge function is constructed by a scale factor times a linear function of η, i.e., $k_1(\eta + b)$ and $k_2(\eta + b)$ for two sides ridge function. The near-side jet function is same as Eq.(3.2). The fit parameter is shown in the plots. Parameter N is used for jet yield ratio calculation.

We also studied other fit functions. According to the χ^2 value for each fit, we conclude that those other functions do not describe data well.

Furthermore, different ZYAM methods could have an influence on the jet yield, thus affecting the jet yield ratio. Hence, we studied ZYAM systematics in the following ways. The ZYAM is obtained by stepping over the $\Delta\phi$ projection with a window of $\Delta\phi = \pi/6$. Other $\Delta\phi$ windows $\Delta\phi = \pi/8$ and $\Delta\phi = \pi/4$ were applied to both high-

Table 3.4
Jet ratio systematic study

Functions	p-side jet ratio	Pb-side jet ratio
Default: Generalized gaus + linear function * ZYAM	3.08	3.13
Gassian shape jet + linear function * ZYAM	2.91	2.76
Fit p-side and Pb-side together	3.47	3.51

and low- multiplicity events. The corresponding jet ratios are compared with the default value in Table. 3.5.

Table 3.5
ZYAM systematic study

ZYAM window	p-side jet ratio	Pb-side jet ratio
$\pi/8$	2.85	3.27
$\pi/6(default)$	3.08	3.13
$\pi/4$	3.03	3.12

From the Table 3.4 and 3.5, adding the two systematic errors of the jet ratio quadratically, we conclude the jet scales of both sides with systematic uncertainties are:

Pb-side: $3.08^{+0.39}_{-0.32}$, p-side: $3.13^{+0.40}_{-0.37}$

The comparison of V_2 and V_3 obtained from using lowest jet ratio, highest jet ratio is shown in Fig. 3.24. In the jet region ($1 < \eta < 2.2$ of p-side or $-2.2 < \eta < -1$ of Pb-side) the difference resulting from different jet ratios is significant. This is due to the influence from jet ratio on near-side jet subtraction (Eq.(3.5)), which leads to different V_n values in jet region. On the other hand, the jet ratio also influences how much the away-side is subtracted for the full η range, which is a smaller portion

compared to the away-side ridge. As a result, the ridge region ($-2.2 < \eta < 1$ of p-side or $-1 < \eta < 2.2$ of Pb-side) is less influenced by the different jet ratio.

Only the ridge region contributes to the final result. So when estimating the systematic error, only the ridge region is taken into account as shown in the ratio plots from Figs. 3.24 and 3.25.

The same dataset was used for V_2 calculation with identical statistical errors so no statistical errors contribute to the fluctuation in the ratio. All the fluctuation should be counted as systematic error. The ratio is filled into a histogram, the systematic error is then calculated via the fluctuation (the RMS value) of this histogram. The greater systematic value from p-side and Pb-side is chosen. The systematic error on V_2 is 3%. The systematic error on V_3 is 3%. The self-normalized $v_n(\eta)/v_n(0)$ is a constant scale of V_n, so we quote the same systematic errors.

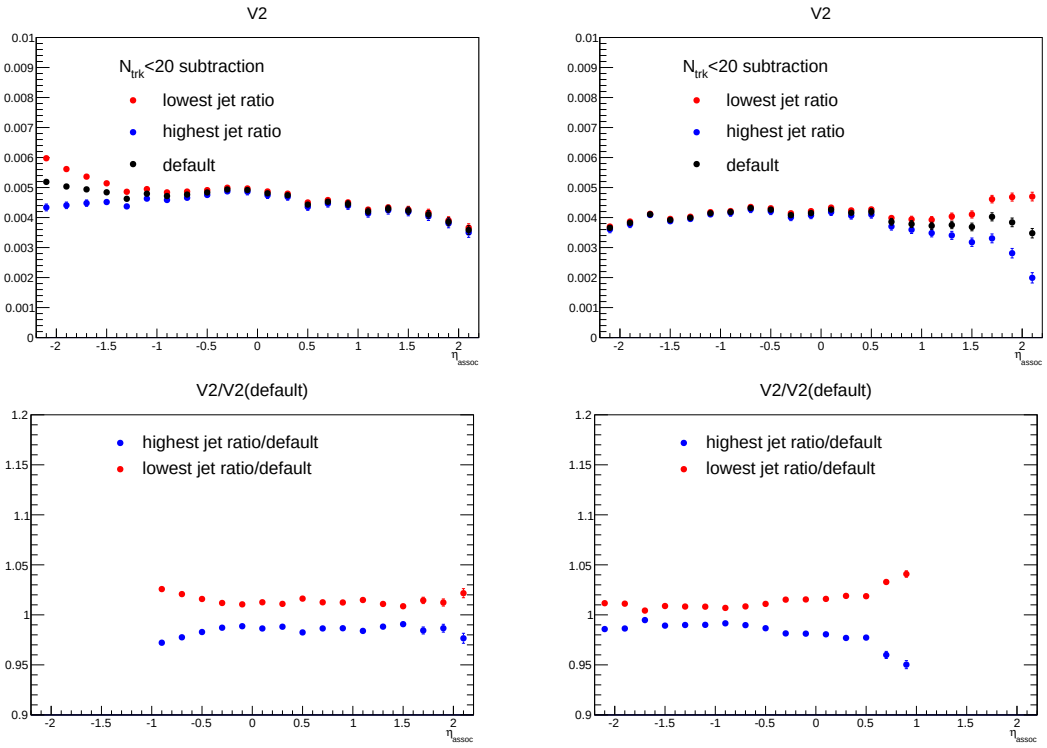

Figure 3.24. Top: Comparison of V_2 in pPb collisions without low multiplicity subtraction at 5.02 TeV extracted using low and high value of jet ratio (α) systematic error. *Left* is the Pb-side trigger, *right* is p-side trigger. V_n is compared for both before and after low multiplicity subtraction. Trigger and associated particle p_{T} are both $0.3 < p_{\mathrm{T}} < 3$ GeV/c. High multiplicity collisions are defined by $220 \leq N_{trk}^{offline} < 260$ and low multiplicity collisions by $2 \leq N_{trk}^{offline} < 20$. Bottom: The ratio of lowest jet ratio and highest jet ratio result to the default, with low multiplicity subtraction.

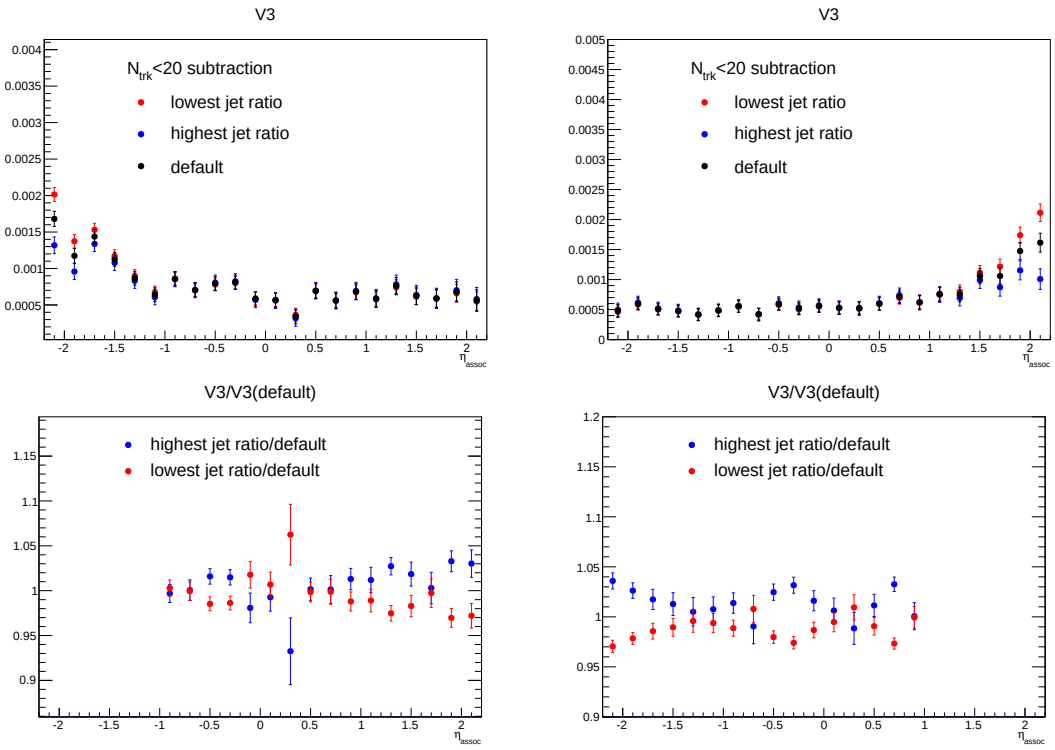

Figure 3.25. Top: Comparison of V_3 in pPb collisions without low multiplicity subtraction at 5.02 TeV extracted using low and high value of jet ratio (α) systematic error. *Left* is the Pb-side trigger, *right* is p-side trigger. V_n is compared for both before and after low multiplicity subtraction. Trigger and associated particle p_{T} are both $0.3 < p_{\mathrm{T}} < 3$ GeV/c. High multiplicity collisions are defined by $220 \leq N_{trk}^{offline} < 260$ and low multiplicity collisions by $2 \leq N_{trk}^{offline} < 20$. Bottom: The ratio of lowest jet ratio and highest jet ratio result to the default, with low multiplicity subtraction.

3.4.6 Study of beam direction systematics

In the middle of 2013 pPb run, the pPb beam direction was reversed. Our result contains both data. The reversed beam direction data is flipped in η and combined with the other half. Hence, we want to study the beam direction systematic error to estimate some of the η dependent systematic errors. Such as the tracking efficiency, and the detector acceptance systematics.

Figs. 3.26 and 3.27 shows the V_n comparison and ratio of the two different beam directions. Similar as we discussed in section3.4.1, the pPb and Pbp samples are statistically independent, so the error is propagated on ratio plot. The $(Ratio - 1)/E_{stat}$ distribution is filled in the histogram and fit with Gaussian. RMS and mean values are shown in the plot. The systematic error can be obtained via Eq (3.8).

The systematic uncertainty of $\pm 3\%$ is estimated for V_2 with low multiplicity subtraction, and $\pm 2.5\%$ without low multiplicity subtraction. The systematic uncertainty of $\pm 12.5\%$ is estimated for V_3 with low multiplicity subtraction, and $\pm 8.5\%$ without low multiplicity subtraction. The same systematic errors are quoted for $v_2(\eta)/v_2(0)$, and $v_3(\eta)/v_3(0)$, respectively.

The systematic error of beam direction is no greater than the addition of other systematic errors, as shown in Table 3. This demonstrates that no additional η dependent systematic errors need to be considered. Hence, in order to avoid the double counting, the beam direction systematic study is *not* added to the total systematic uncertainty.

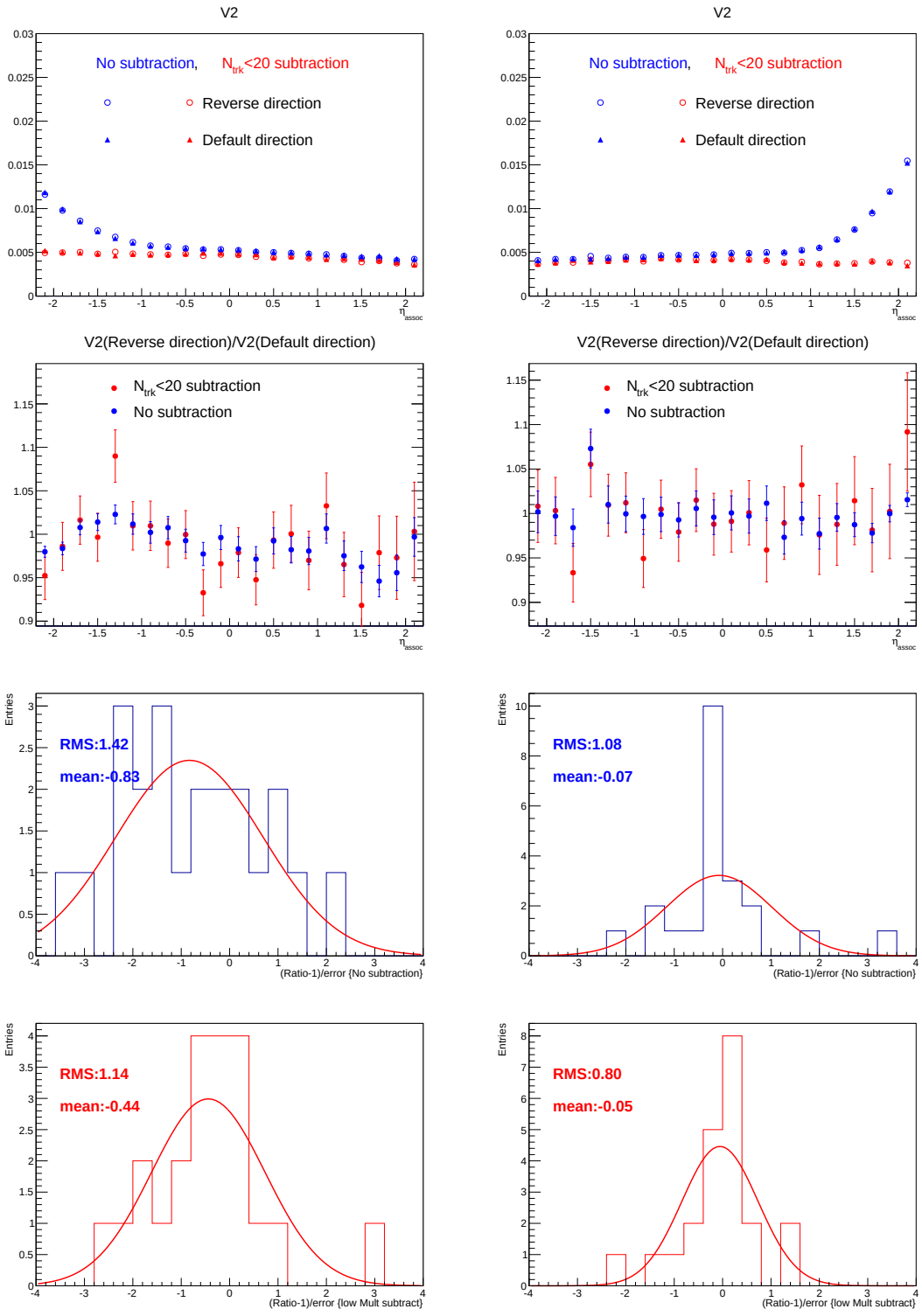

Figure 3.26. Top: Comparison V_2 of pPb default direction collisions events and reversed direction events at 5.02 TeV. V_2 result before low multiplicity subtraction (blue) and after subtraction (red) are shown with both Pb-side trigger (left) and p-side trigger(Right). Trigger and associated particle p_{T} are both $0.3 < p_{\mathrm{T}} < 3$ GeV/c. High multiplicity collisions are defined by $220 \leq N_{trk}^{offline} < 260$ and low multiplicity collisions by $2 \leq N_{trk}^{offline} < 20$. Second row: V_2 Ratio of reversed beam direction to the default direction. Bottom: $(Ratio - 1)/E_{stat}$ distribution of low multiplicity subtraction and no subtraction.

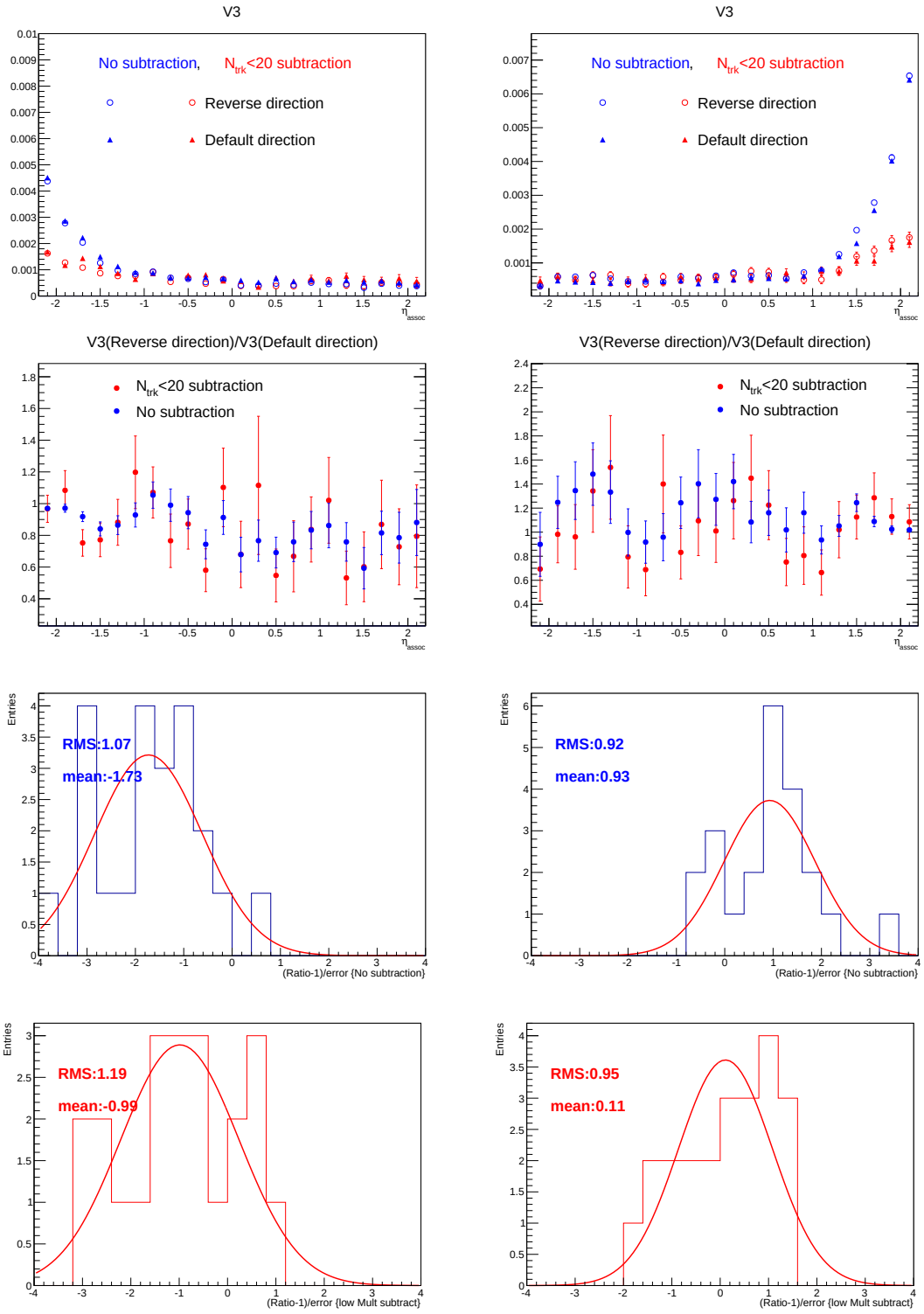

Figure 3.27. Top: Comparison V_3 of pPb default direction collisions events and reversed direction events at 5.02 TeV. V_2 result before low multiplicity subtraction (Blue) and after subtraction (Red) are shown with both Pb-side trigger(Left) and p-side trigger(Right). Trigger and associated particle p_{T} are both $0.3 < p_{\mathrm{T}} < 3$ GeV/c. High multiplicity collisions are defined by $220 \leq N_{trk}^{offline} < 260$ and low multiplicity collisions by $2 \leq N_{trk}^{offline} < 20$. subtraction. Second row: V_3 Ratio of reversed beam direction to the default direction. Bottom: $(Ratio - 1)/E_{stat}$ distribution of low multiplicity subtraction and no subtraction.

3.4.7 Cross check of efficiency correction of trigger particles

The trigger efficiency was not applied to the trigger particles in the two-particle correlation calculation. In this section, trigger efficiency is applied as a cross check to the default selection. The result is shown in Fig. 3.28. The V_2 results with and without trigger efficiency are consistent with each other within a small uncertainty.

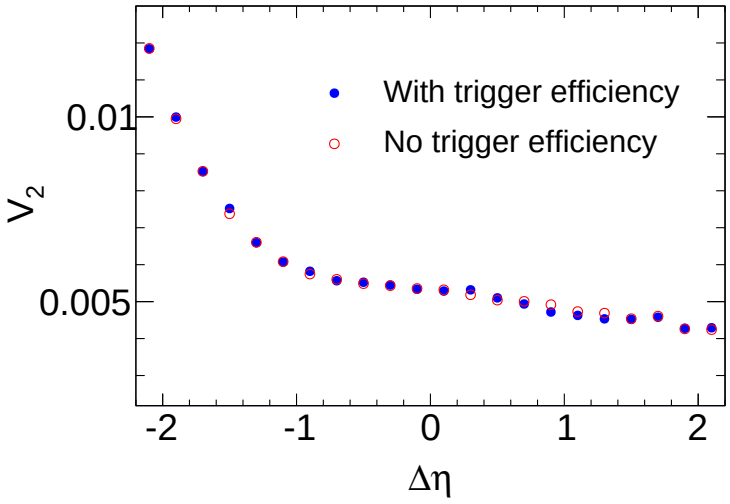

Figure 3.28. Comparison V_2 in pPb collisions at 5.02 TeV for trigger efficiency corrected events (blue) and not corrected (red) events. Trigger and associated particle p_{T} are both $0.3 < p_{\mathrm{T}} < 3$ GeV/c. High multiplicity collisions are defined by $220 \leq N_{trk}^{offline} < 260$.

3.4.8 Cross check of V_2 calculation method

The procedure to calculate Fourier decomposition V_2 is from a previous publication [35]. As a cross check, another method is applied by subtracting the scaled low multiplicity correlation function from high multiplicity correlation function. The underlying event was subtracted from the low multiplicity correlation using the ZYAM method. This ensures that the low multiplicity subtraction only removes the jet

contribution to the correlation function. A comparison of these methods is shown in Fig. 3.29. As can be seen, the two methods are consistent with each other with a negligible uncertainty.

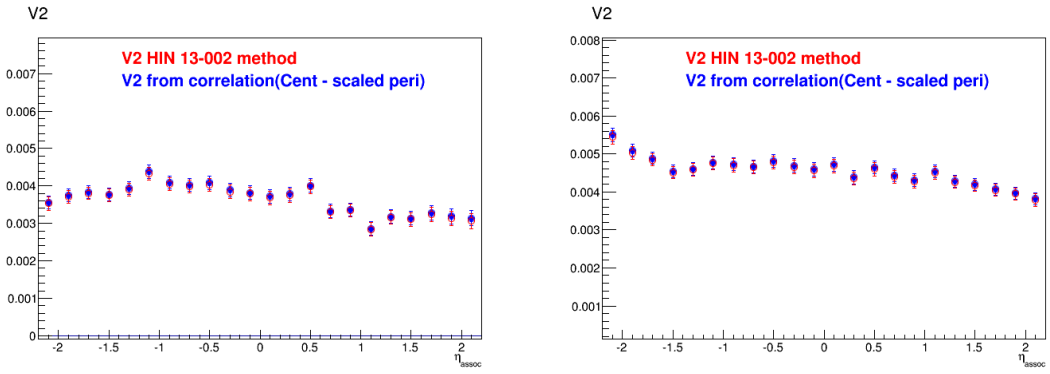

Figure 3.29. Comparison of V_2 results obtained by two methods as labeled, for p-side trigger (left) and Pb-side (right). Trigger and associated particle p_{T} are both $0.3 < p_{\mathrm{T}} < 3$ GeV/c. High multiplicity collisions are defined by $220 \leq N_{trk}^{offline} < 260$ and low multiplicity collisions by $2 \leq N_{trk}^{offline} < 20$.

3.4.9 Comparison to cumulant method

The Fourier harmonics can be extracted from two-particle correlation. The cumulant methods were also processed to obtain the single particle v_2. In addition, the 2- and 4-particle cumulant calculations were both applied and the reference particle method was used. The single particle $v_2\{2\}$ and $v_2\{4\}$ are scaled by arbitrary numbers so that the values are comparable. Only the shape of the single particle η dependence is compared. Furthermore, the ratio of the cumulant method to two-particle correlation method is calculated. Both the v_2 shape comparison and the ratio are shown in Fig. 3.30. In the ratio plot, a linear fit is included to check if the ratio is flat. If the slope is 0, the ratio is consistent with a constant number, which means the two datasets are comparable.

In Fig. 3.30 the $v_2\{2\}$ shape is comparable to the result from the non-subtracted two-particle method, and $v_2\{4\}$ is comparable to the result from low-subtracted two-particle method. This is expected, since the 4-particle v_2 contains less non-flow effect, in which a dominant source is near-side jet. Also in the low-multiplicity results, the jet is subtracted. On the other hand, $v_2\{2\}$ and non-subtracted results both contain some jet contribution.

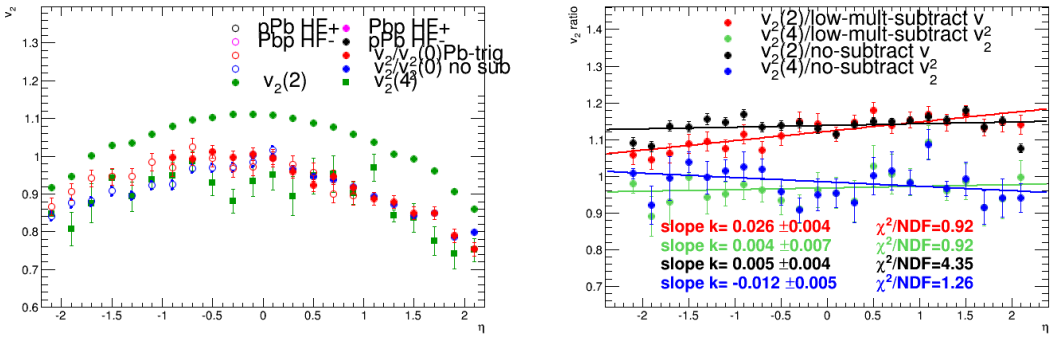

Figure 3.30. (Left)Comparison of η dependence v_2 results obtained by cumulant method and two-particle correlation method as labeled. (Right) Ratio of cumulant method v_2 to two-particle correlation method single particle v_2. Trigger and associated particle p_{T} are both $0.3 < p_{\mathrm{T}} < 3$ GeV/c. High multiplicity collisions are defined by $220 \leq N_{trk}^{offline} < 260$ and low multiplicity collisions by $2 \leq N_{trk}^{offline} < 20$. Cumulant method is using $220 \leq N_{trk}^{offline} < 240$ multiplicity bin.

3.4.10 Closure test with HIJING

To verify the procedure of subtracting the low multiplicity V_n result from the high multiplicity data to remove non-flow effects, studies using HIJING simulation are presented. Only generator-level (generated particles before going to the detector step) particles are used to maximize the event samples.

Two CMS HIJING samples were processed, one without flow (default HIJING), the other with afterburner flow. The input value to generate flow particles is $v_2 = 0.05$. The high multiplicity and low multiplicity cuts are $120 \leq N^{\text{gen-level}} < 150$ and $N^{\text{gen-level}} < 35$.

The $\Delta\phi$ distribution of high multiplicity 2-particle correlation and scaled low multiplicity correlation are shown in Fig. 3.31. The scaled $N^{\text{gen-level}} < 35$ distribution is very close to the distribution for $120 \leq N^{\text{gen-level}} < 150$. The $\Delta\phi$ distribution of HIJING with flow is shown in Fig. 3.32.

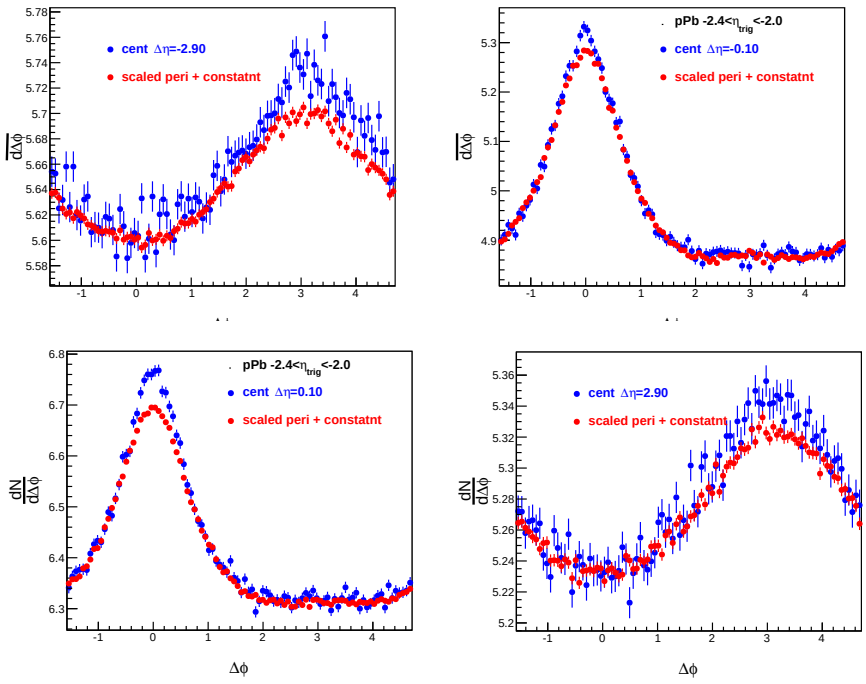

Figure 3.31. $\Delta\phi$ distribution of high multiplicity 2-particle correlation and scaled low multiplicity correlation. The scale is from jet yield ratio times associate particle per trigger ratio of p-side trigger(Top) and Pb-side trigger (Bottom) for HIJING only, $0.3 < p_{\text{T}}^{\text{trig}} < 3$ GeV/c.

Fig. 3.33 shows the V_2 η dependence result for both HIJING with flow and HIJING only. They are plotted with and without low multiplicity subtraction. In the top plots, V_2 for low multiplicity subtraction shows V_2 is consistent with zero within 5%.

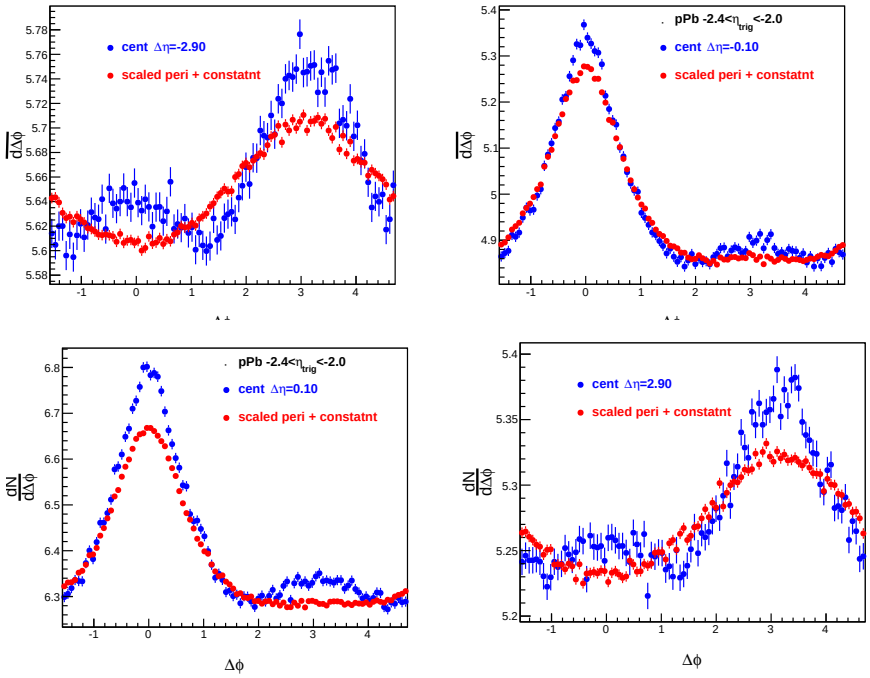

Figure 3.32. $\Delta\phi$ distribution of high multiplicity 2-particle correlation and scaled low multiplicity correlation. The scale is from jet yield ratio times associate particle per trigger ratio of p-side trigger (Top) and Pb-side trigger, for HIJING +flow with input $v_2 = 0.05$, $0.3 < p_{\mathrm{T}}^{\mathrm{trig}} < 3$ GeV/c.

Moreover, in the HIJING with flow result, the V_2 value is around 0.0025, which is the square of the input vale $v_2 = 0.05$. This indicates that the low multiplicity subtraction method works as expected.

3.4.11 Cross check of ZYAM method

The ZYAM method introduced in Section 3.3.1 involved by selecting the minimum value at each $\Delta\eta$ bin. However, in the near-side jet region, the minimum value is raised up by the jet contribution, thus the ZYAM value may not be the real background. The shape of the ZYAM "background" could potentially influence the linear dependence

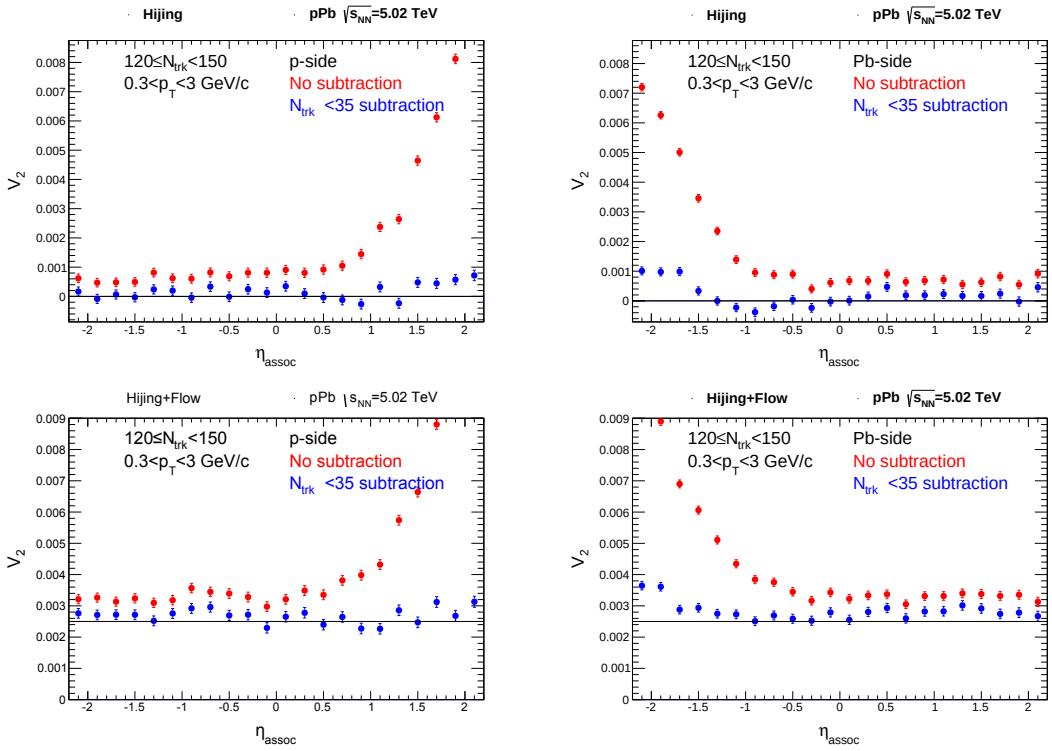

Figure 3.33. The extracted V_2 from high multiplicity 2-particle correlation and with subtraction of scaled low multiplicity correlation. The scale is from jet yield ratio times associate particle per trigger ratio of p-side trigger(Left) and Pb-side trigger (Right), with HIJING (Top) and HIJING+flow(Bottom) with input $v_2 = 0.05$, $0.3 < p_{\mathrm{T}}^{\mathrm{trig}} < 3$ GeV/c. The black line in top plots is at $V_2 = 0$, in the bottom plots is at $V_2 = 0.0025$.

of the ridge. Here we use an alternative background as a cross check to study the dependence.

We may use the $dN/d\eta$ as the background, but the $\eta_{\mathrm{lab}}^{\mathrm{trig}}$ distribution smears to the two-particle correlation $\Delta\eta$ projection, as well as the background. As a result, a randomized $\eta_{\mathrm{lab}}^{\mathrm{trig}}$ distribution is introduced and the background is filled with

$$\Delta\eta_{rand} = \eta_{\mathrm{lab}}^{\mathrm{assoc}} - \eta_{\mathrm{lab}}^{\mathrm{trig}}{}_{rand}. \tag{3.9}$$

Table 3.6

Comparison of fitted parameters between those for default background (ZYAM) and background built from $\Delta\eta_{rand}$ in pPb collisions (labeled as "$\Delta\eta_{rand}$ background").

Parameter	Pb-side trigger	p-side trigger
Y (default)	0.401 ± 0.011	0.489 ± 0.011
Y ($\Delta\eta_{rand}$ background)	0.499 ± 0.077	0.493 ± 0.075
k (default)	- 0.0011 ± 0.0001	0.0002 ± 0.0001
k ($\Delta\eta_{rand}$ background)	- 0.0008 ± 0.0008	0.0047 ± 0.0009
α (default) with uncertainties	$3.08 \pm 0.11^{+0.96}_{-0.31}$	$3.13 \pm 0.09^{+0.28}_{-0.28}$
α ($\Delta\eta_{rand}$ background)	3.83	3.16

Here ${\eta^{\rm trig}_{\rm lab}}_{rand}$ is a random value obtained from the $dN/d\eta^{\rm trig}_{\rm lab}$ distribution. To simplify the $dN/d\eta^{\rm trig}_{\rm lab}$ distribution, a linear function is used to fit the distribution, and then the random values are generated from on this linear function. In this way the $B(\Delta\eta)$ (the background from $\Delta\eta_{rand}$) is the realistic background. It's not precisely equal to the shape of the single particle $dN/d\eta$, but smeared by the trigger η range.

The background is then scaled by a factor, which is obtained from the averaged long range $S(\Delta\eta)/B(\Delta\eta)$ ratio, where the $S(\Delta\eta)$ is the signal correlated yield. Repeating the same procedure to fit the ridge shape, we obtain the results in Fig. 3.34. The fits show similar linear dependence compared to those in Fig. 3.11. The Table 3.6 lists the comparison of part of fitted parameter of high multiplicity events between the default result and the the result using background built from $\Delta\eta_{rand}$. The jet ratios α are also compared. The α ($\Delta\eta_{rand}$ background) values of both sides are within the systematic uncertainties of the α (default). Thus it will not add extra systematic uncertainties.

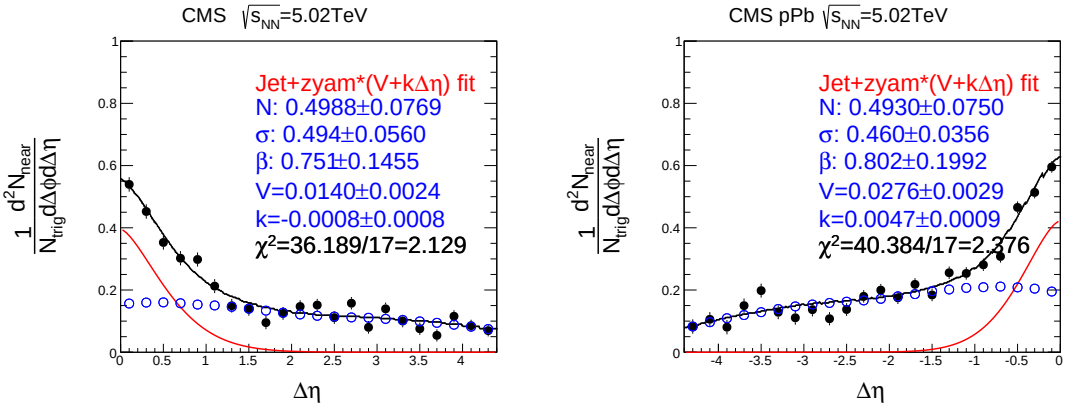

Figure 3.34. Near-side correlated yield after $B(\Delta\eta)$ background subtraction for high-multiplicity $220 \leq N_{trk}^{offline} < 260$. The correlated yields are fit by Eq. 3.2. Data are 5.02 TeV pPb collisions for pairs of charged particles with $0.3 < p_{\mathrm{T}}^{\mathrm{trig}}, p_{\mathrm{T}}^{\mathrm{assoc}} < 3$ GeV/c, and trigger particle η windows of Pb-side ($-2.4 < \eta_{\mathrm{lab}}^{\mathrm{trig}} < -2.0$, left) and p-side ($2.0 < \eta_{\mathrm{lab}}^{\mathrm{trig}} < 2.4$, right.)

3.5 Results

The V_2 and V_3 values in high-multiplicity collisions (triangles) for Pb-side and p-side trigger particles are shown in Fig. 3.35. The strong peak is caused by near-side short-range jet contributions. The circles in Fig. 3.35 show the Fourier coefficients, $V_2^{\rm sub}$ and $V_3^{\rm sub}$, after the low-multiplicity data are subtracted. The short-range jet-like peak is largely reduced, but may not be completely eliminated due to different near-side jet-correlation shapes for high- and low-multiplicity collisions. The long-range results are not affected by the near-side jet, but the away-side jet may still contribute if its shape is different in high- and low-multiplicity collisions or if its magnitude does not scale according to α. By self-normalization,

$$v_n(\eta_{\rm lab}^{\rm assoc})/v_n(\eta_{\rm lab}^{\rm assoc}=0) = V_n(\eta_{\rm lab}^{\rm assoc})/V_n(\eta_{\rm lab}^{\rm assoc}=0). \tag{3.10}$$

the Fourier coefficient from both trigger sides can be merged into a single distribution by combining the negative and positive $\eta_{\rm lab}$ range. The lab frame central value $\eta_{\rm lab}=0$ is used so that the separation of the central value to both $\eta_{\rm lab}^{\rm trig}$ is the same. In this way, possible contamination from jets is kept at the same level as a function of $\eta_{\rm lab}$. This is more important for the Fourier coefficients determined without subtraction of the low-multiplicity data. Figure 3.36 shows the $v_2(\eta_{\rm lab})/v_2(\eta_{\rm lab}=0)$ and $v_3(\eta_{\rm lab})/v_3(\eta_{\rm lab}=0)$ results obtained from the corresponding V_2 and V_3 data in Fig. 3.35. The curves show the $v_n(\eta_{\rm lab})/v_n(\eta_{\rm lab}=0)$ obtained from the high-multiplicity data alone, V_n^{HM}, without subtraction of the low-multiplicity data. The data points are obtained from the low-multiplicity-subtracted $V_n^{\rm sub}$; closed circles are from the Pb-side trigger particle data and open circles from the p-side. To avoid large contamination from short-range correlations, only the $|\Delta\eta|>2$ range is shown, but still with enough overlap in mid-rapidity $\eta_{\rm lab}$ between the two trigger selections. A good agreement is observed between with and without low multiplicity subtraction. Significant pseudorapidity dependence is observed for the anisotropy parameter; it decreases by about $(24\pm4)\%$ (statistical uncertainty only) from $\eta_{\rm lab}=0$ to $\eta_{\rm lab}=2$

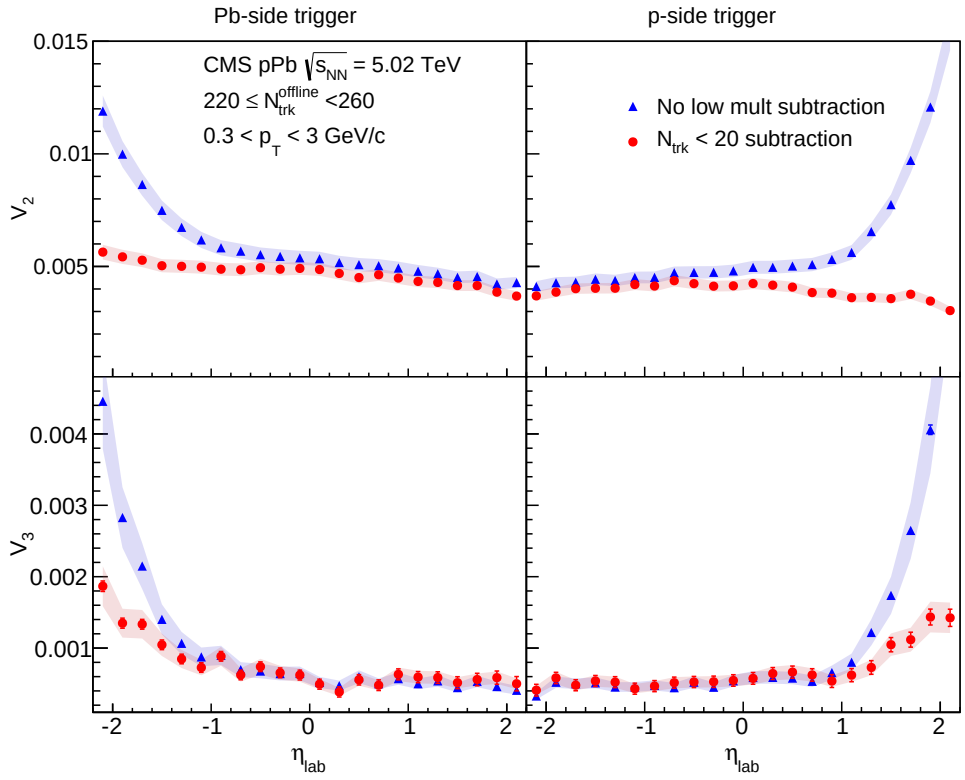

Figure 3.35. Fourier coefficients, V_2 (upper) and V_3 (lower), of two-particle azimuthal correlations in high-multiplicity collisions ($220 \leq N_{trk}^{offline} < 260$) with and without subtraction of low-multiplicity data, as a function of $\eta_{\rm lab}$. Left panel shows data for Pb-side trigger particles and the right panel for the p-side. Statistical uncertainties are mostly smaller than point size; systematic uncertainties are 3.9% and 10% for V_2 and V_3 without low-multiplicity subtraction, 5.8% and 15% for V_2 and V_3 with low-multiplicity subtraction, respectively. The systematic uncertainties are shown by the shaded bands.

in the p-direction. The behavior of the normalized $v_2(\eta_{\rm lab})/v_2(\eta_{\rm lab}=0)$ is different in the Pb-side, with the maximum difference being smaller. The v_2 appears to be asymmetric about $\eta_{\rm cm}=0$, which corresponds to $\eta_{\rm lab}=0.465$. A non-zero v_3 is observed, however, the uncertainties are too large to draw a definite conclusion regarding its pseudorapidity dependence.

When using long-range two-particle correlations to obtain anisotropic flow, the large pseudorapidity separation between the particles, while reducing nonflow effects, may also lead to an underestimation of the anisotropic flow because of event plane decorrelation stemming from the fluctuating initial conditions [74, 75]. This effect was studied in pPb and PbPb collisions [76]. The observed decrease in v_2 with increasing absolute value of pseudorapidity in Fig. 3.36 could be partially due to such decorrelation.

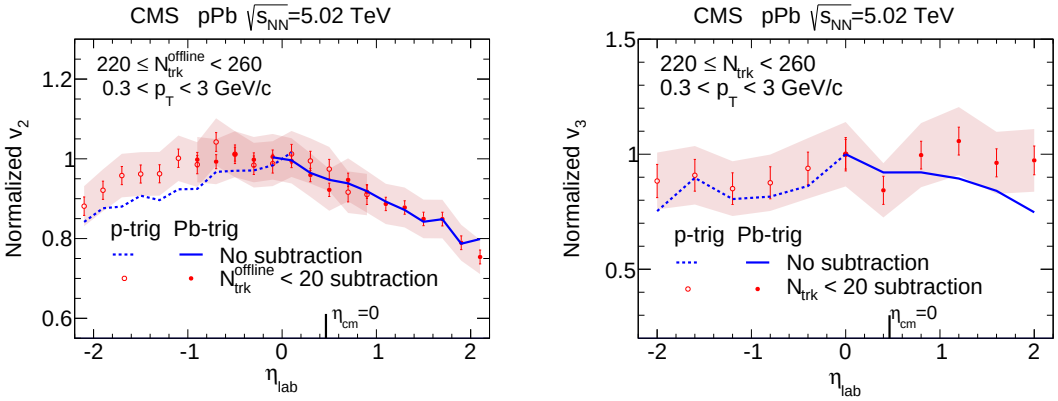

Figure 3.36. Self-normalized anisotropy parameters, $v_2(\eta_{\rm lab})/v_2(\eta_{\rm lab} = 0)$ (left panel) and $v_3(\eta_{\rm lab})/v_3(\eta_{\rm lab} = 0)$ (right panel), as a function of $\eta_{\rm lab}$. Data points (curves) are results with (without) low-multiplicity data subtraction; filled circles and solid line are from the Pb-side trigger. Open circles and dashed line are from the p-side trigger. The bands show systematic uncertainties of $\pm 5.7\%$ and $\pm 14\%$ for $v_2(\eta_{\rm lab})/v_2(\eta_{\rm lab} = 0)$ and $v_3(\eta_{\rm lab})/v_3(\eta_{\rm lab} = 0)$, respectively. The systematic uncertainties in $v_n(\eta_{\rm lab})/v_n(\eta_{\rm lab} = 0)$ without subtraction are similar. Error bars indicate statistical uncertainties only.

The asymmetry of the azimuthal anisotropy distribution as pseudorapidity is studied by taking the ratio of the v_n value at positive $\eta_{\rm cm}$ to the value at $-\eta_{\rm cm}$ in the center-of-mass frame, as shown in Fig. 3.37. The ratio shows a decreasing trend with increasing $\eta_{\rm cm}$.

In pPb collisions, the average $p_{\rm T}$ of charged hadrons depends on pseudorapidity. As stated in Ref. [77], the pseudorapidity dependence of $\langle p_{\rm T} \rangle$ could influence the pseu-

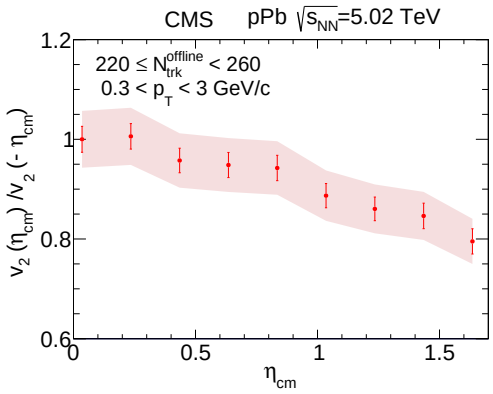

Figure 3.37. $v_2(\eta_{\rm cm})/v_2(-\eta_{\rm cm})$, as a function of $\eta_{\rm cm}$ in the center-of-mass frame. The data points are results from $V_n^{\rm sub}$ with low-multiplicity data subtracted. The bands show the systematic uncertainty of $\pm 5.7\%$. Error bars indicate statistical uncertainties only.

dorapidity dependence of v_2. This may have relevance to the shape of the normalized v_2 distribution as observed in Fig. 3.36. To compare v_2 and the $\langle p_{\rm T}\rangle$ distribution, the $p_{\rm T}$ spectra for different $\eta_{\rm cm}$ ranges are obtained from Ref. [78]. The charged particle $p_{\rm T}$ spectra in minimum-bias events are then fitted with a Tsallis function [30],

$$\frac{1}{2\pi p_{\rm T}}\frac{d^2N}{d\eta dp_{\rm T}} = C\left(1+\frac{p_{\rm T}}{nT}\right)^{-n} \tag{3.11}$$

where C, n, T are the fit parameters. The inclusive-particle $p_{\rm T}$ is averaged within $0 < p_{\rm T} < 6$ GeV/c. In addition, the average momentum for the particles used in this analysis, $0.3 < p_{\rm T} < 3$ GeV/c and $220 \le N_{trk}^{offline} < 260$, is calculated and plotted in Fig. 3.38. The $\langle p_{\rm T}\rangle$ as a function of $\eta_{\rm cm}$ does not change for different multiplicity ranges within 1%. Thus, the minimum bias $\langle p_{\rm T}\rangle$ distribution is compared directly to the high-multiplicity anisotropy v_2 result. The $\langle p_{\rm T}\rangle$ distribution is normalized by its value at $\eta_{\rm cm} = 0$. Self-normalized $\langle p_{\rm T}\rangle(\eta_{\rm cm})/\langle p_{\rm T}\rangle(\eta_{\rm cm}=0)$ is plotted in Fig. 3.38, compared to the self-normalized $v_2(\eta_{\rm cm})/v_2(\eta_{\rm cm}=-0.465)$ distribution in the center-of-mass frame. The systematic uncertainty band on $\langle p_{\rm T}\rangle(\eta_{\rm cm})/\langle p_{\rm T}\rangle(\eta_{\rm cm}=0)$ is obtained separately from averaging the upper and lower limits from the underlying $p_{\rm T}$

spectra. The upper and lower limits are from the systematic uncertainty band. The hydrodynamic theoretical prediction for $\langle p_{\mathrm{T}}\rangle(\eta_{\mathrm{cm}})/\langle p_{\mathrm{T}}\rangle(\eta_{\mathrm{cm}}=0)$ is also plotted.

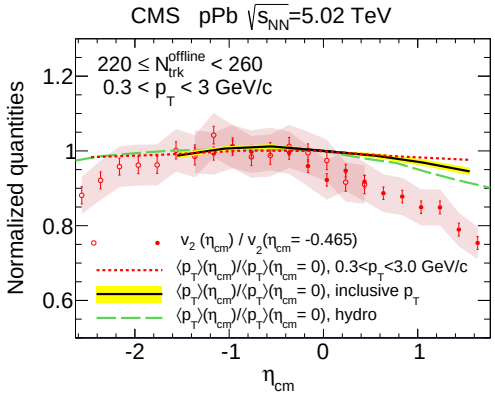

Figure 3.38. Self-normalized $v_2(\eta_{\mathrm{cm}})/v_2(\eta_{\mathrm{cm}}=-0.465)$ distribution with low-multiplicity subtraction from Pb-side (filled circles) and p-side (open circles) triggers, and $\langle p_{\mathrm{T}}\rangle(\eta_{\mathrm{cm}})/\langle p_{\mathrm{T}}\rangle(\eta_{\mathrm{cm}}=0)$ of $0<p_{\mathrm{T}}<6$ GeV/c range from minimum-bias events (solid line) and $0.3<p_{\mathrm{T}}<3$ GeV/c range from high-multiplicity ($220\leq N_{trk}^{offline}<260$) events (dotted line) as functions of η_{cm}. Dashed curve is the hydrodynamic prediction [77] for $\langle p_{\mathrm{T}}\rangle(\eta_{\mathrm{cm}})/\langle p_{\mathrm{T}}\rangle(\eta_{\mathrm{cm}}=0)$ distribution.

As shown in Fig. 3.38, the hydrodynamic calculation [77] for $\langle p_{\mathrm{T}}\rangle$ falls more rapidly than $\langle p_{\mathrm{T}}\rangle$ of data (solid and dotted lines) towards positive η_{cm}, and slightly less towards the negative side. The distribution is asymmetric for both data and theory. The comparison of the $\langle p_{\mathrm{T}}\rangle$ and the v_2 distributions shows that both observables have a decreasing trend towards large $|\eta_{\mathrm{cm}}|$, but the decrease in $\langle p_{\mathrm{T}}\rangle$ at forward pseudorapidity is smaller. The decrease of v_2 with η_{cm} does not appear to be entirely due to a change in $\langle p_{\mathrm{T}}\rangle$; other physics is likely at play. The value of v_2 decreases by $(20\pm4)\%$ (statistical uncertainty only) from $\eta_{\mathrm{cm}}=0$ to $\eta_{\mathrm{cm}}\approx1.5$.

3.6 Conclusion

In this study, two-particle correlations as functions of $\Delta\phi$ and $\Delta\eta$ are reported in pPb collisions at $\sqrt{s_{NN}}=5.02$ TeV. The trigger particle is restricted to narrow

pseudorapidity windows. In this way, the η dependence of the ridge could be studied. The combinatorial background is assumed to be uniform in $\Delta\phi$ and normalized by the ZYAM procedure as a function of $\Delta\eta$. The near-side jet and ridge is decomposed using a fit function. The near-side jet correlated yield is fitted and found to be greater in high-multiplicity than in low-multiplicity collisions. The ridge yield is studied as a function of $\Delta\phi$ and $\Delta\eta$ and it is found to depend on pseudorapidity as well as the underlying background shape ZYAM($\Delta\eta$). The pseudorapidity dependence differs for trigger particles selected on the proton and the Pb sides.

Furthermore, the Fourier coefficients of the two-particle correlations in high-multiplicity collisions are studied, with and without subtraction of the scaled low-multiplicity data. The pseudorapidity dependence of the single-particle anisotropy parameters, v_2 and v_3, is inferred. Significant pseudorapidity dependence of v_2 is found. The distribution is asymmetric about $\eta_{\rm cm} = 0$ with an approximate $(20 \pm 4)\%$ decrease from $\eta_{\rm cm} = 0$ to $\eta_{\rm cm} \approx 1.5$, and a smaller decrease towards the Pb-beam direction. Finite v_3 is observed, but the uncertainties are presently too large to draw conclusions regarding the pseudorapidity dependence.

The self-normalized $v_2(\eta_{\rm cm})/v_2(\eta_{\rm cm} = -0.465)$ distribution is compared to the $\langle p_{\rm T}\rangle(\eta_{\rm cm})/\langle p_{\rm T}\rangle(\eta_{\rm cm} = 0)$ distribution from minimum bias events as well as from hydrodynamic calculations. The $\langle p_{\rm T}\rangle(\eta_{\rm cm})/\langle p_{\rm T}\rangle(\eta_{\rm cm} = 0)$ distribution shows a decreasing trend towards positive $\eta_{\rm cm}$. The $v_2(\eta_{\rm cm})/v_2(\eta_{\rm cm} = -0.465)$ distribution also shows a decreasing trend towards positive $\eta_{\rm cm}$, but the decrease is more significant in the case of the v_2 measurement. This indicates that physics mechanisms other than the change in the underlying particle spectra, such as event plane decorrelation over pseudorapidity, may influence the anisotropic flow.

4. Away side jet correlation shape analysis

As discussed in section 1.4.1, jets as a probe are a useful tool to study parton and medium interactions. Previously many jet-like correlation analyses were carried using two-particle correlation method [79]. In heavy ion collisions, flow is a large background in two-particle correlations. A commonly used method to subtract flow is to construct the background combing different flow components. However, the disadvantage is obvious. The flow is constructed from v_n coefficients, and the uncertainty from each coefficient contributes to the flow background shape, thus a large uncertainty will be introduced to the flow-subtracted jet result. In this chapter a novel method is described. In this new method two-particle correlations of the selected events are constructed from two different regions, which have same flow background but different away jet contributions. In addition, the near-side jet is not biased by this selection method, thus the near-side jet contribution is the same for the two regions. As a consequence the difference of these two-particle correlation functions contains no flow background but away jet contribution only. In this way the flow background is fully subtracted. It will be shown how the selection of events is processed and how this selection benefits the background subtraction.

4.1 Data sample and event selection

The measurement is processed utilizing minimum-bias Lead-Lead (PbPb) collisions at center of mass energy of 2.76 TeV per nucleon pair over a broad range of pseudorapidity (η) and azimuthal angle (ϕ). The data were collected during CMS PbPb (Lead-Lead) collision in November and December 2011.

CMS uses various triggers to record PbPb collisions. The minimum-bias PbPb data are recorded based on the coincidence signal of scintillator counters (BSC,

$3.23 < |\eta| < 4.65$) or in the steel/quatz-fiber Cherenkov forward hadron calorimeters (HF,$2.9 < |\eta| < 5.2$) from both ends of the detector. In addition, most of them are also detected by coincidence of the ZDC and BRAN scintillators (placed behind ZDC electromagnetic section.) In order to suppress non-collision noise, including cosmics, radioactivity, double firing triggers and beam background, a coincidence of BPTX, i.e. two ion beam bunch crossing coincidence, is requested to all these triggers [80]. The minimum-bias events are selected by L1 triggers, then passed to the HLT trigger.

The offline event selection requires at least 3 hits in the HF calorimeter on both sides, with at least 3 GeV energy in each cluster, and present a primary vertex containing at least 2 tracks. These requirements further reduce the background from single beam interactions, cosmic muons and large impact parameter, ultra-peripheral collisions that lead to the electromagnetic breakup of one or both of the Pb nulei [81].

4.2 Analysis technique

In this section the methodology to select the events of interest is introduced. The events with enhanced away-side jets are selected. The away-side jet correlation shape is extracted from the two-particle correlation functions.

4.2.1 Centrality definition

The region of interest is the mid-rapidity region, $-1.2 < \eta < 1.2$, in which the correlation functions are obtained. The correlation functions are studied for various multiplicity bins, and within each bin the multiplicity in the $-1.2 < \eta < 1.2$ range need to be similar. Thus the multiplicity in this analysis is defined as the number of particles in the region $-1.2 < \eta < 1.2$, denoted as $N_{\mathrm{trk}}^{|\eta|<1.2}$.

4.2.2 P_{x} event selection method

The trigger particle is selected by the $3 < p_{\mathrm{T}} < 10$ GeV/c high p_{T} cut, in order to enhance the leading jet. In addition, to get more control of away-side jet, an event selection is introduced to enrich the probability of finding away-side jet in the so called out-region, defined as $\eta_{\,\mathrm{out}}$, as shown in Fig. 4.1.

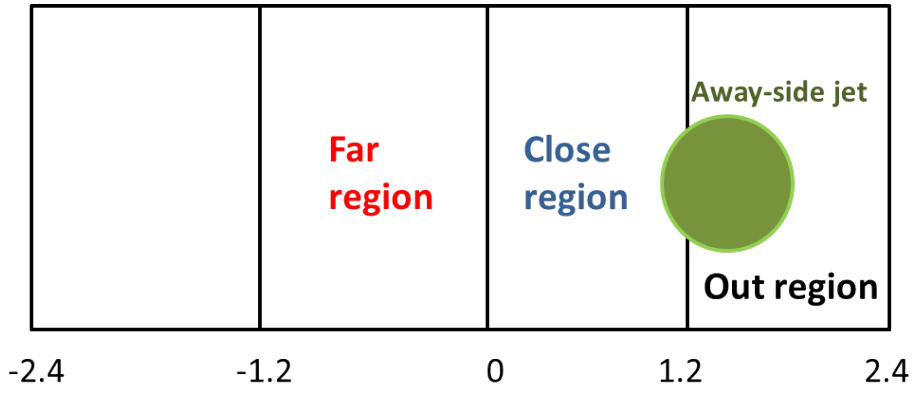

Figure 4.1. A sketch of one event that most part of away-side jet is at the large η region. Different η ranges (close-, far- and out-regions) are shown on the sketch.

The total momentum of recoil particles from the high p_{T} trigger particle, P_x, is defined by:

$$P_x|_{\eta_1<\eta<\eta_2} = \sum_{|\phi-\phi_{trig}|>\pi/2} \cos(\phi - \phi_{trig}) \times p_{\mathrm{T}}/\epsilon \tag{4.1}$$

where the $\eta_1 < \eta < \eta_2$ is the $\eta_{\,\mathrm{out}}$ region, within which the away-side jets are enhanced. ϵ is the acceptance correction factor including the η and ϕ correction. All the particles reconstructed in the range of $0.4 < p_T < 10$ GeV/c are included to calculate the P_{x}. Only particles from the back side of the trigger particle are calculated. In this way, the η of the near-side jet will not affect the P_{x} value.

Figure 4.2 shows the P_{x} distribution of two different centrality bin (after η, ϕ correction, discussed in next section). The distribution is asymmetric because it combines the underlying event and the jet contribution.

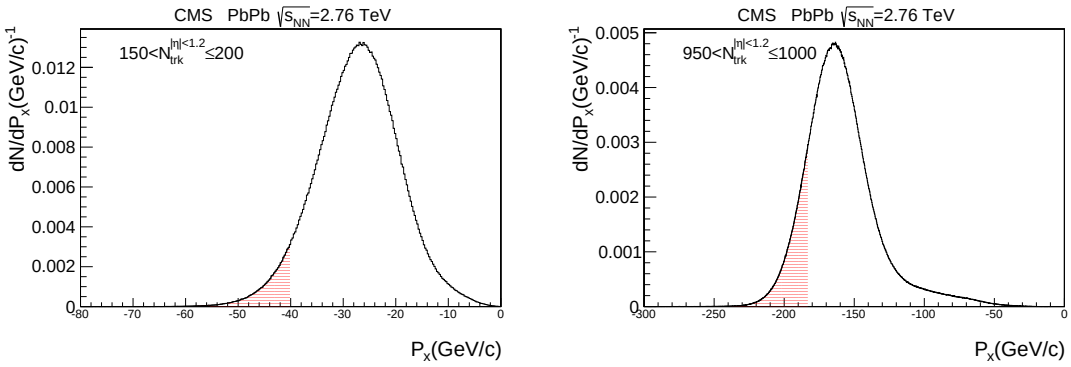

Figure 4.2. The $P_{\rm x}$ distribution of PbPb collision at $\sqrt{s_{_{NN}}} = 2.76GeV$. Left: $150 < N_{\rm trk}^{|\eta|<1.2} < 200$. Right: $950 < N_{\rm trk}^{|\eta|<1.2} < 1000$.

The red shaded region is the lowest 5% of the $P_{\rm x}$ distribution, which will be used for the away-side correlation study in this section. After the selection the events have higher possibility to contain a jet in the $\eta_{\rm\,out}$ region, since the corresponding trigger particle has more particles on its back side.

4.2.3 Corrections

In this analysis both η and ϕ correction is applied. The η distribution of different z_{vtx} (Z-vertex) events is quite different with respect to the $z_{vtx} = 0$ cm events, because of the η limitation of the detector. As shown in Fig. 4.3, the $z_{vtx} = 15$ cm events, for example, have a very asymmetric η distribution. This effect needs to be corrected in the P_x calculation.

The correction table is obtained as a function of η, z_{vtx}, $p_{\rm T}$ and centrality, since the $p_{\rm T}$ and centrality will both influence the η distribution. The $p_{\rm T}$ was divided into 10 bins, while the centrality is divided into 25 bins. One example of how to obtain the correction table is shown in Fig. 4.3 for 1 GeV/c $< p_{\rm T} <$ 1.5 GeV/c and $150 < N_{\rm trk}^{|\eta|<1.2} < 200$. For each centrality and $p_{\rm T}$ bin, the average of $dN/d\eta(|z_{vtx}| < 1$ cm) is symmetrized at first and set to be the default $dN/d\eta$ distribution, as shown on the left side of Fig. 4.3. This is to make sure the default distribution is symmetric

and get rid of any detector non-uniformity. Then $dN/d\eta$ distribution from varies z_{vtx} are divided by the default distribution. The division is then normalized to average unity and the inverse is the correction factor. On right hand of Fig. 4.3, the $dN/d\eta$ distributions for -15 cm $< z_{vtx} < -13$ cm and 13 cm $< z_{vtx} < 15$ cm are shown. The distributions are asymmetric and very different for the two z_{vtx} range on the edge. One of the η correction table is shown in Fig. 4.4.

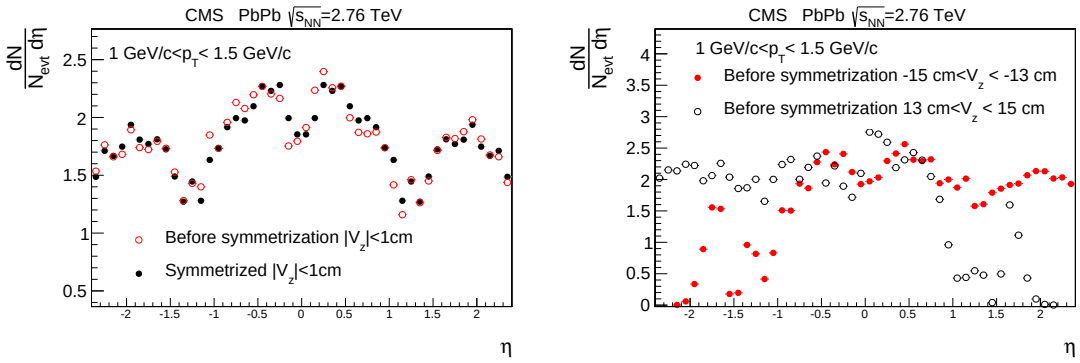

Figure 4.3. The $dN/d\eta$ distribution of different Z-vtx range for 1 GeV/c $< p_{\rm T} <$ 1.5 GeV/c and $150 < N_{\rm trk}^{|\eta|<1.2} < 200$. Left: $|z_{vtx}| < 1$ cm before and after symmetrization. Right: The $dN/d\eta$ distribution of -15 cm $< z_{vtx} < -13$ cm and 13 cm $< z_{vtx} < 15$ cm.

The detector sometimes contains bad segments in the azimuthal direction. A ϕ correction is introduced to correct for this non-uniformity. The correction table is calculated separately for different z_{vtx} and $p_{\rm T}^{\rm assoc}$. The ϕ distribution of each bin is obtained and the average of the distribution is then normalized to unity. The inverse of the distribution is used as the ϕ efficiency table. This correction is applied to the $P_{\rm x}$ calculation as well as the two-particle correlation function.

4.2.4 Two-particle correlation function and away-side jet extraction

As shown in Fig. 4.1, the close- and far- region is defined as:

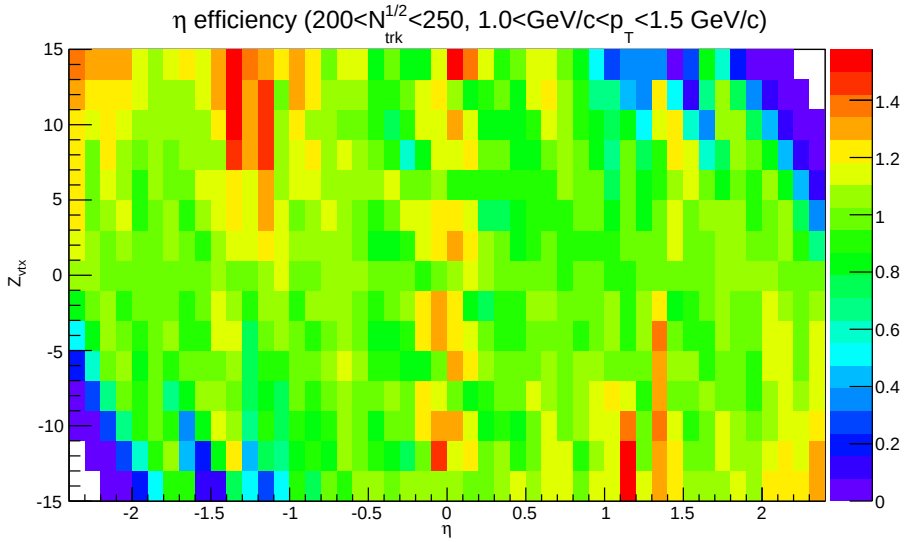

Figure 4.4. The η and Z-vtx correction example for centrality $200 < N_{\rm trk}^{|\eta|<1.2} < 250$ and 1 GeV/c $< p_{\rm T} <$ 1.5 GeV/c.

$$\begin{cases} 0 < \eta_{\text{ close}} < 1.2, -1.2 < \eta_{\text{ far}} < 0 & \text{while } 1.2 < \eta_{\text{ out}} < 2.4; \\ -1.2 < \eta_{\text{ close}} < 0, 0 < \eta_{\text{ far}} < 1.2 & \text{while } -2.4 < \eta_{\text{ out}} < -1.2; \end{cases} \tag{4.2}$$

The correlation function from close- and far- region are calculated separately. The near-side of close- and far- region has slight difference; it could due to the acceptance effect. We use a small correction factor, α to account for this difference. The α value is obtained via a constant fit to the ratio of the close correlation function to the far correlation function, as shown in Fig. 4.5. It is fitted within the near-side region ($|\Delta\phi| < 1$). The constant value α is then applied as a scalar factor to the far region.

After applying the α correction, the close- and far- region correlation function is shown in Fig. 4.6.

To remove the effect of collective flow, the far-region correlation function is subtracted from the close-region correlation function. As discussed above, the near-side jet and flow background is symmetric about mid-rapidity in a AA collision system.

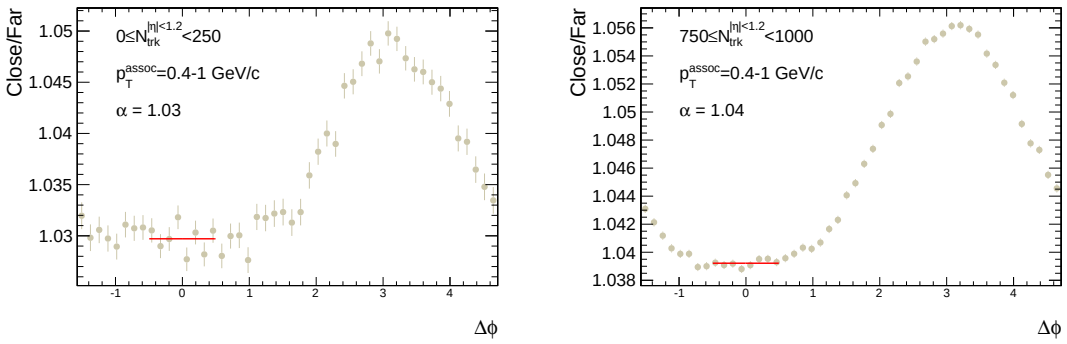

Figure 4.5. The constant value fit for the near-side region ($|\Delta\phi| < 1$) for 0.4 GeV/c < pt < 1.0 GeV/c of PbPb collision at $\sqrt{s_{NN}} = 2.76GeV$. The α correction factor is shown on the figure. Left: $0 < N_{\rm trk}^{|\eta|<1.2} < 250$. Right: $750 < N_{\rm trk}^{|\eta|<1.2} < 1000$.

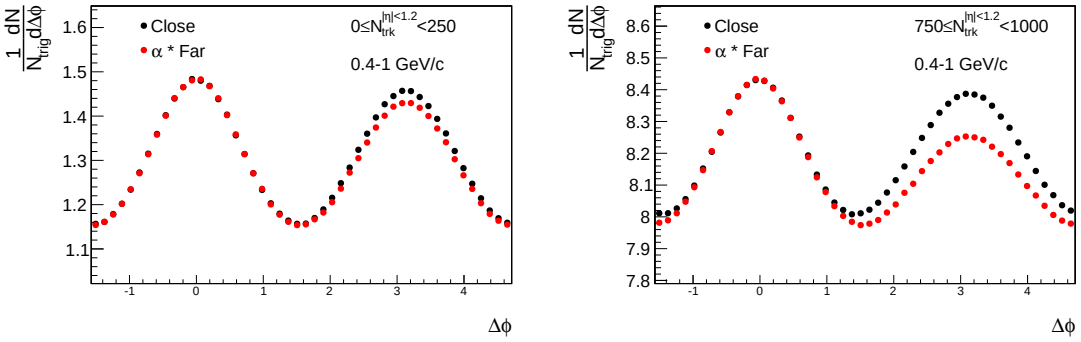

Figure 4.6. The correlation function of close- and far- region for 1 GeV/c < pt < 1.5 GeV/c for 0.4 GeV/c < pt < 1.0 GeV/c of PbPb collision at $\sqrt{s_{NN}} = 2.76$ TeV. The far-region correlation function is scaled by α. Left: $0 < N_{\rm trk}^{|\eta|<1.2} < 250$. Right: $750 < N_{\rm trk}^{|\eta|<1.2} < 1000$.

So ideally the subtraction will remove the background, leaving only the away-side jet shape.

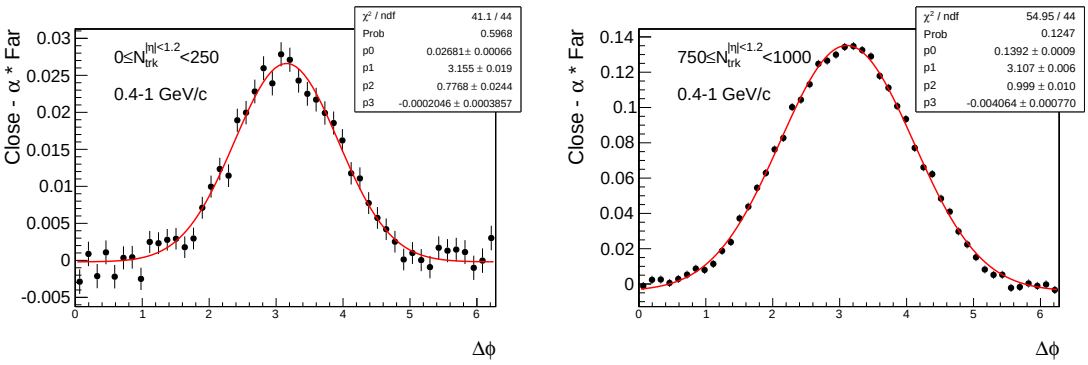

Figure 4.7. The correlation function of close - far region for 0.4 GeV/c < pt < 1.0 GeV/c of PbPb collision at $\sqrt{s_{NN}} = 2.76GeV$. Left: $0 < N_{\rm trk}^{|\eta|<1.2} < 250$. Right: $750 < N_{\rm trk}^{|\eta|<1.2} < 1000$.

After the away-side jet shape is obtained, it is fitted by a Gaussian function plus a constant value,

$$G(\Delta\phi) = N \exp\left[-\frac{(\Delta\phi - b)^2}{2\sigma^2}\right] + const. \tag{4.3}$$

The σ of the Gaussian function represents the jet width. The constant parameter is to account for the uncertainty in near-side region, however it is very close to 0. Similarly, the b parameter represents the center of the Gaussian function, but it is around π.

4.3 systematic study and cross check

The systematic study is divided into the following parts: the $P_{\rm x}$ cut systematic study, by varying the percentage of $P_{\rm x}$ cut; The systematic from track quality cuts, by applying loose and tight track quality cuts; the fit range systematic study, by varying the away-side jet fit range. The total systematic uncertainty is 12% combining the two sources, as shown in Table 4.1.

Table 4.1

Summary of systematic uncertainties of away-side jet width in PbPb collisions at $\sqrt{s_{NN}}$=2.76 TeV.

Source	Away-side jet width systematics
P_{x} cut	3.6%
Track quality cuts	10.0%
Fit range	4%
Total	12%

4.3.1 P_{x} selection systematic study

The default event selection is the lowest 5% P_{x} value. However other percentage of P_{x} cut could be used as well. In this section two different P_{x} cut is used: 2.5% and 10%. They are considered as systematics on the P_{x} selection.

After obtained the jet width result, the value is divided by the default value and the ratio is filled into a histogram as shown in Fig. 4.8 . The RMS of the histogram is regard as the systematic uncertainty. The value is 3.6%.

4.3.2 Track quality cuts systematic study

To estimate the uncertainty of track quality cuts, a set of tighter and looser track quality cuts are tested on the data:

Tight selections:

- $dz/dz_{err} < 2$
- $dxy/dxy_{err} < 2$
- $\sigma(p_T)/p_T < 0.05$.

Loose selections:

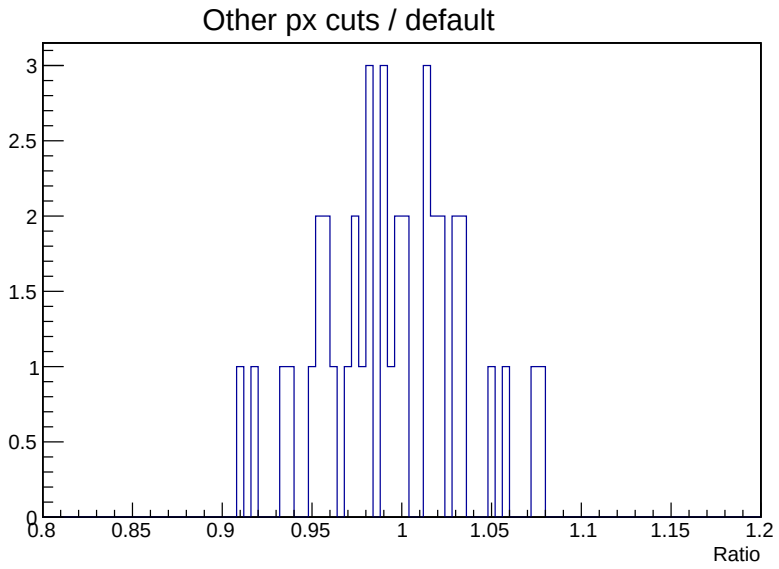

Figure 4.8. The jet width result of other P_{x} cuts (2.5% and 10%) to the default P_{x} cut (5%) ratio. The RMS of this ratio distribution is considered as the systematic uncertainty.

- $dz/dz_{err} < 5$
- $dxy/dxy_{err} < 5$.

The same efficiency table is used for different track quality cuts. After changing the track quality cuts, the definition of event multiplicity remains unchanged. Then the fitted jet widths are compared. The ratios of jet width for loose/tight cuts to the jet width of the default cuts are filled into a histogram. The RMS of this histogram is estimated as the systematic uncertainty. The histogram is shown in Fig. 4.9. The systematic uncertainty from track quality cuts is 10%.

4.3.3 Jet fit method systematic study

The fit function is defined as a Gaussian function. The away-side distribution is fitted by a Gaussian function plus a constant function. We can vary the fit range to

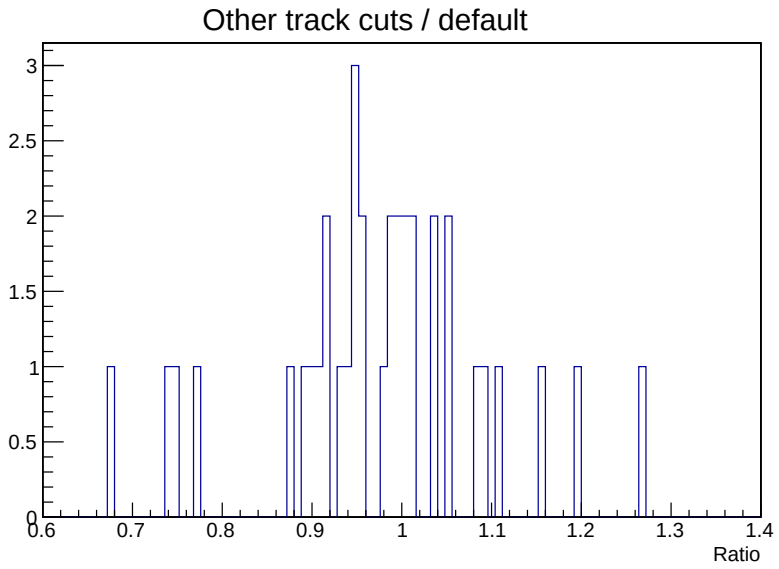

Figure 4.9. The jet width result of other P_{x} cuts (2.5% and 10%) to the default P_{x} cut (5%) ratio. The RMS of this ratio distribution is considered as the systematic uncertainty.

get a slight different jet width. The default fit is on the full $\Delta\phi$ range. Alternatively, a range of $1 < \Delta\phi < 5$ is taken and fitted with the same function. The result is then compared to the default result and the ratio is filled into a histogram. Similarly the RMS of this histogram is regarded as the systematic uncertainty as shown in Fig. 4.10. The value is 4%.

4.4 Results

On Fig. 4.11 the jet width is plotted as a function of centrality for various $p_{\mathrm{T}}^{\mathrm{assoc}}$ with systematic uncertainty. From the figure the jet width shows a increasing trend with multiplicity, which indicates jet broadening and/or event averaging of away-side jet deflected by the medium flow. These medium effects play a more important role in the central events. At same multiplicity, the lower $p_{\mathrm{T}}^{\mathrm{assoc}}$ particle have a larger

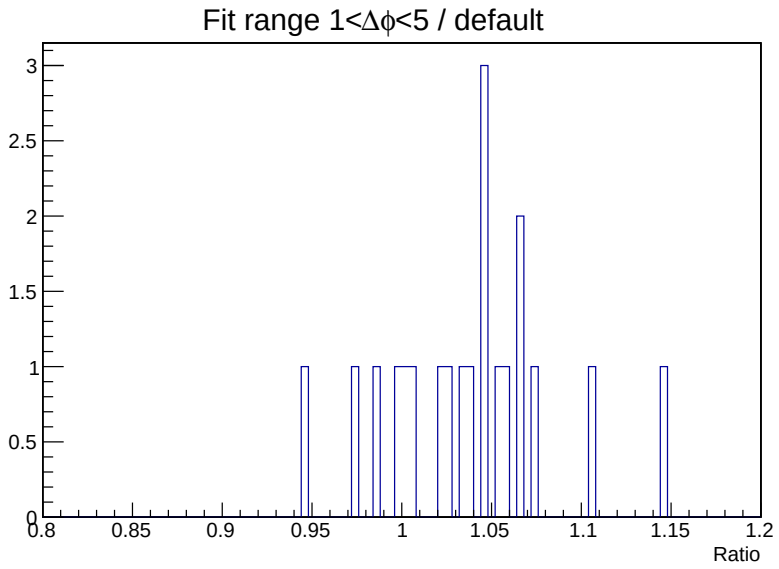

Figure 4.10. The jet width result of tight and loose cuts to the default track cut ratio. The RMS of this ratio distribution is considered as the systematic uncertainty.

away-side jet width. This is expected from jet fragmentation. Possible effects from medium modification beyond in-vacuum fragmentation need further investigation.

4.5 Discussion and future direction

In this chapter, a novel method is introduced to study the away-side jet shape. By using the data itself to subtract the flow background, the flow background is fully subtracted. The method is applied in $\sqrt{s_{NN}} = 2.76$ TeV PbPb collision at LHC, to various multiplicity and p_{T} ranges. The jet width is then studied as a function of both p_{T} and multiplicity, and it is found to increase as a function of multiplicity.

This method could further be applied to three-particle analysis, which may reveal more medium effects in heavy ion collisions, for example the gluon radiation and deflected jets. In some previous studies [61], the flow background of three-particle correlation was calculated via a derived formula, which is constructed by the v_n

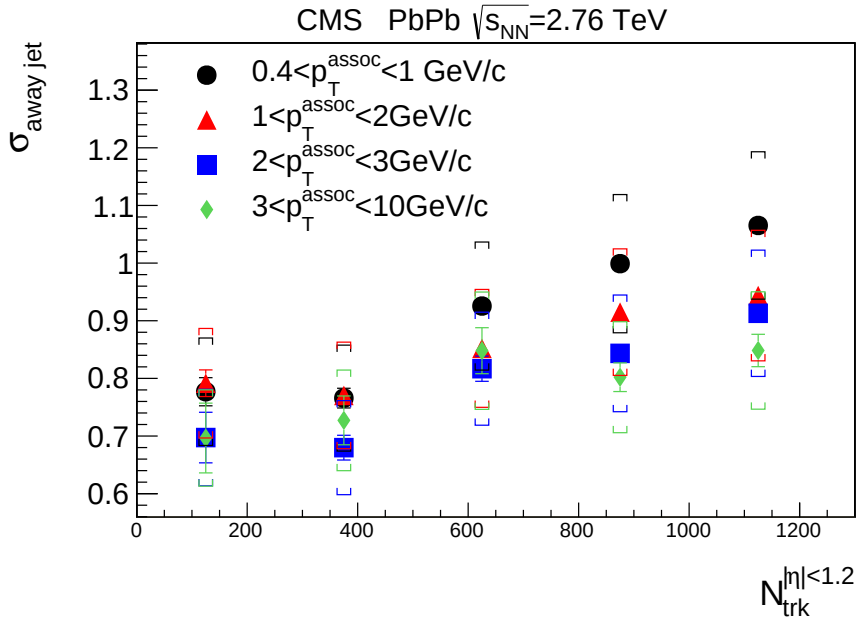

Figure 4.11. The jet width result as a function of $N_{\rm trk}^{|\eta|<1.2}$ with systematic uncertainty of PbPb collision at $\sqrt{s_{NN}}$=2.76 TeV.

harmonics. This will introduce large systematic uncertainties. By subtracting the flow itself instead, the systematic errors from the calculation could be minimized. At the same time a more complicated correlation function needs to be built for the close- and far- region to fully subtract the background.

In this study, all of the particles are from "generalTracks" collection. As a result the trigger particle $p_{\rm T}$ range is limited by the detector. Also some particles that are not from jet are selected. In order to reach higer $p_{\rm T}$, a reconstructed jet could be used, and the correlation between jet-track could be studied. The reconstructed jet $p_{\rm T}$ could reach up to 400 GeV/c in CMS. This will bring additional information of away-side jet modification in heavy ion collisions.

5. Summary

The two-particle correlation method is widely used in heavy ion collision analysis. It is a powerful tool to study the physics of the QGP created in collisions of nuclei and nucleons. In this dissertation, the ridge phenomenon is studied in pPb collision at $\sqrt{s_{_{NN}}}$=5.02 TeV.

In particular, the pseudorapidity dependence of the ridge is studied. The ZYAM method is applied to obtain the ridge yield as a function of pseudorapidity. A linear dependence on the underlying event multiplicity is observed for the ridge yield. In addition, the pseudorapidity dependence of Fourier harmonics V_2 and V_3 is extracted from the two-particle correlation method. The self-normalized single particle v_2 and v_3 are studied as a function of $\eta_{\rm cm}$. The v_2 is found to depend on pseudorapidity, and the dependence is asymmetric about $\eta_{\rm cm}$. The possible physics mechanisms for the observed η-dependence need further investigation.

The two-particle correlation method is also widely used in a jet-like correlation studies. In this dissertational project, a novel method is developed to subtract flow background. Events are selected with a relatively large recoil momentum $P_{\rm x}$ from a high $p_{\rm T}$ trigger particle to enchance the away-side jet population. The correlation functions are constructed from two η regions symmetric about mid-rapidity but with different η distributions from the $P_{\rm x}$ region. The flow backgrounds in the two correlation functions are the same and thus subtracted in the correlation function difference. The away-side jet width is extracted from two-particle correlation function and studied as a function of multiplicity and $p_{\rm T}^{\rm assoc}$. The jet width increases with multiplicity, which indicates jet-medium modification in central collisions.

LIST OF REFERENCES

LIST OF REFERENCES

[1] S. Eidelman and others. Review of particle physics. Particle Data Group. *Phys. Lett. B*, 592:1, 2004.

[2] M. Gell-Mann. A schematic model of baryons and mesons. *Phys. Lett.*, 8(3):214 – 215, 1964.

[3] An SU(3) model for strong interaction symmetry and its breaking. *CERN-TH-401*, Jan 1964.

[4] Jerome Friedman and Henry W Kendall. Deep inelastic electron scattering. *Annu. Rev. Nucl. Sci.*, pages 203–254, 1972.

[5] Frank Wilczek. Asymptotic Freedom: From Paradox to Paradigm. *Proc.Nat.Acad.Sci.*, 102:8403, 2005.

[6] Kenneth G. Wilson. Confinement of quarks. *Phys. Rev. D*, 10:2445–2459, Oct 1974.

[7] M. A. Stephanov. QCD phase diagram: an overview. *PoS LAT2006*, 2006.

[8] DOE/NSF Nuclear Science Advisory Committee. The Frontiers of Nuclear Science: A Long Range Plan. 2007.

[9] S Chakrabarty. On the possibility of nuclear liquid-gas phase transition. *Journal of Physics G: Nuclear and Particle Physics*, 20(3):469, 1994.

[10] G. Baym and C. Pethick. *Landau Fermi-Liquid Theory: Concepts and Applications*. Wiley-VCH, 2004.

[11] J. J. R. M. van Heugten, Shaoyu Yin, and H. T. C. Stoof. Fermi-liquid theory of imbalanced quark matter. *Phys. Rev. D*, 85:125030, Jun 2012.

[12] J. C. Collins and M. J. Perry. Superdense Matter: Neutrons or Asymptotically Free Quarks? *Phys. Rev. Lett.*, 34:1353–1356, May 1975.

[13] T. D. Lee. Abnormal nuclear states and vacuum excitation. *Rev. Mod. Phys.*, 47:267–275, Apr 1975.

[14] The space-time evolution of a heavy-ion collision, which undergoes a phase transition to a QGP. http://www.star.bnl.gov/gorbunov/main/img56.png, 2004.

[15] Wojciech Florkowski. The realistic QCD equation of state in relativistic heavy-ion collisions and the early Universe. *Nuclear Physics A*, 853(1):173 – 188, 2011.

[16] Yasuyuki Akiba and others. The Hot QCD White Paper: Exploring the Phases of QCD at RHIC and the LHC. Feb 2015.

[17] David dEnterria and Barbara Betz. High- Hadron Suppression and Jet Quenching. In *The Physics of the Quark-Gluon Plasma*. Springer, 2010.

[18] K. Adcox and others. Suppression of Hadrons with Large Transverse Momentum in Central Au+Au Collisions at $\sqrt{s_{_{NN}}} = 130$ GeV. *Phys. Rev. Lett.*, page 022301, 2002.

[19] Barbara Betz. Jet Quenching in Heavy-Ion Collisions - The Transition Era from RHIC to LHC. *Eur. Phys. J.*, A48, 2012.

[20] Ulrich Heinz and Raimond Snellings. Collective flow and viscosity in relativistic heavy-ion collisions. *Ann.Rev.Nucl.Part.Sci.*, 63:123–151, 2013.

[21] Jean-Yves Ollitrault. Anisotropy as a signature of transverse collective flow. *Phys.Rev.*, D46:229–245, 1992.

[22] J.-Y. Ollitrault. Anisotropy as a signature of transverse collective. *Phys. Rev. D*, 46:229–245, 1992.

[23] Rajeev S. Bhalerao and Jean-Yves Ollitrault. Eccentricity fluctuations and elliptic flow at RHIC. *Physics Letters B*, 641:260 – 264, 2006.

[24] Marguerite Belt Tonjes et al. Flow in Au+Au collisions at RHIC. *Journal of Physics G: Nuclear and Particle Physics*, 30(8):S1243, 2004.

[25] J. Adams et al. Azimuthal Anisotropy at the Relativistic Heavy Ion Collider: The First and Fourth Harmonics. *Phys. Rev. Lett.*, 92:062301, Feb 2004.

[26] B. Abelev et al. System-size independence of directed flow measured at the bnl relativistic heavy-ion collider. *Phys. Rev. Lett.*, 101:252301, Dec 2008.

[27] B. Abelev et al. Directed flow of charged particles at mid-rapidity relative to the spectator plane in Pb-Pb collisions at $\sqrt{s_{_{NN}}}$=2.76 TeV. *Phys. Rev. Lett.*, 111:232302, 2013.

[28] B. Alver and G. Roland. Collision geometry fluctuations and triangular flow in heavy-ion collisions. *Phys. Rev. C*, 81:054905, 2010. Erratum-ibid. **C82**, 039903 (2010).

[29] H. A. Gustafsson et al. Collective Flow Observed in Relativistic Nuclear Collisions. *Phys. Rev. Lett.*, 52:1590–1593, Apr 1984.

[30] Measurement of the elliptic anisotropy of charged particles produced in PbPb collisions at nucleon-nucleon center-of-mass energy = 2.76 TeV. *Phys. Rev. C*, 87:014902, 2013.

[31] K. Aamodt et al. Elliptic Flow of Charged Particles in Pb-Pb Collisions at $\sqrt{s_{NN}} = 2.76$ TeV. *Phys. Rev. Lett.*, 105:252302, Dec 2010.

[32] K. Aamodt et al. Higher Harmonic Anisotropic Flow Measurements of Charged Particles in Pb-Pb Collisions at $\sqrt{s_{NN}} = 2.76$ TeV. *Phys. Rev. Lett.*, 107:032301, Jul 2011.

[33] A. H. Mueller, editor. *Perturbative Quantum Chromodynamics, Advanced Series on Directions in High Energy Physics Vol. 5*. World Scientific, Singapore, 1989.

[34] Betty Abelev et al. Transverse Momentum Distribution and Nuclear Modification Factor of Charged Particles in p-Pb collisions at $\sqrt{s_{NN}} = 5.02$ TeV. *Phys. Rev. Lett.*, 110:082302, 2013.

[35] Serguei Chatrchyan et al. Multiplicity and transverse momentum dependence of two- and four-particle correlations in pPb and PbPb collisions. *Phys. Lett. B*, 724:213–240, 2013.

[36] Vardan Khachatryan et al. Observation of Long-Range Near-Side Angular Correlations in Proton-Proton Collisions at the LHC. *JHEP*, 1009:091, 2010.

[37] Serguei Chatrchyan et al. Observation of long-range near-side angular correlations in proton-lead collisions at the LHC. *Phys. Lett. B*, 718:795–814, 2013.

[38] Betty Abelev et al. Long-range angular correlations on the near and away side in p-Pb collisions at $\sqrt{s_{NN}} = 5.02$ TeV. *Phys. Lett.*, B719:29–41, 2013.

[39] Georges Aad et al. Observation of Associated Near-side and Away-side Long-range Correlations in $\sqrt{s_{NN}}$=5.02 TeV Proton-lead Collisions with the ATLAS Detector. *Phys. Rev. Lett.*, 110:182302, 2013.

[40] A. Adare et al. Measurement of Long-Range Angular Correlation and Quadrupole Anisotropy of Pions and (Anti)Protons in Central $d+$Au Collisions at $\sqrt{s_{NN}} = 200$ GeV. *Phys. Rev. Lett.*, 114:192301, May 2015.

[41] A. Adare et al. Measurement of Long-Range Angular Correlation and Quadrupole Anisotropy of Pions and (Anti)Protons in Central $d+Au$ Collisions at $\sqrt{s_{NN}} = 200$ GeV. *Phys. Rev. Lett.*, 114:192301, 2015.

[42] L. Adamczyk et al. Long-range pseudorapidity dihadron correlations in d+Au collisions at $\sqrt{s_{NN}} = 200$ GeV. *Phys. Lett. B*, 747:265, 2015.

[43] CMS Collaboration. Evidence for collective multi-particle correlations in pPb collisions. *Phys. Rev. Lett*, 115:012301, 2015.

[44] ATLAS Collaboration. Measurement with the ATLAS detector of multi-particle azimuthal correlations in p+Pb collisions at $\sqrt{s_{NN}} = 5.02$ TeV. *Phys. Lett. B*, 725:60, 2013.

[45] Piotr Bozek. Collective flow in p-Pb and d-Pb collisions at TeV energies. *Phys. Rev. C*, 85:014911, 2012.

[46] Long-range two-particle correlations of strange hadrons with charged particles in pPb and PbPb collisions at LHC energies. *Phys. Lett. B*, 742:200, 2015.

[47] Long-range angular correlations of π K and p in pPb collisions at $\sqrt{s_{NN}} = 5.02$ TeV. *Phys. Lett. B*, 726:164, 2013.

[48] Piotr Bozek. Elliptic flow in proton-proton collisions at $sqrt(S) = 7$ TeV. *Eur. Phys. J.*, C71:1530, 2011.

[49] Piotr Bozek and Wojciech Broniowski. Correlations from hydrodynamic flow in p-Pb collisions. *Phys. Lett. B*, 718:1557–1561, 2013.

[50] Serguei Chatrchyan et al. Long-range and short-range dihadron angular correlations in central PbPb collisions at a nucleon-nucleon center of mass energy of 2.76 TeV. *JHEP*, 1107:076, 2011.

[51] Serguei Chatrchyan et al. Centrality dependence of dihadron correlations and azimuthal anisotropy harmonics in PbPb collisions at $\sqrt{s_{NN}} = 2.76$ TeV. *Eur. Phys. J. C*, 72:2012, 2012.

[52] Ante Bilandzic, Raimond Snellings, and Sergei Voloshin. Flow analysis with cumulants: Direct calculations. *Phys. Rev. C*, 83:044913, 2011.

[53] J. Adams et al. Distributions of charged hadrons associated with high transverse momentum particles in pp and Au + Au collisions at $\sqrt{s_{NN}} = 200$-GeV. *Phys. Rev. Lett.*, 95:152301, 2005.

[54] B. Alver et al. High transverse momentum triggered correlations over a large pseudorapidity acceptance in Au+Au collisions at $\sqrt{s_{NN}} = 200$ GeV. *Phys. Rev. Lett.*, 104:062301, 2010.

[55] B.I. Abelev et al. Long range rapidity correlations and jet production in high energy nuclear collisions. *Phys. Rev. C*, 80:064912, 2009.

[56] Adrian Dumitru, Kevin Dusling, Francois Gelis, Jamal Jalilian-Marian, Tuomas Lappi, et al. The Ridge in proton-proton collisions at the LHC. *Phys. Lett. B*, 697:21–25, 2011.

[57] Kevin Dusling and Raju Venugopalan. Comparison of the Color Glass Condensate to di-hadron correlations in proton-proton and proton-nucleus collisions. *Phys. Rev. D*, 87:094034, 2013.

[58] Yen-Jie Lee. Study of jet quenching using the CMS detector. CMS Collaboration Rencontres Ion Lourds/Heavy Ion Meeting, 2013.

[59] C. Adler et al. Disappearance of back-to-back highpThadron correlations in central Au+Au collisions at$\sqrt{s_{_{NN}}}$= 200 GeV. *Phys. Rev. Lett.*, 90:082302, Feb 2003.

[60] J. Adams et al. Distributions of Charged Hadrons Associated with High Transverse Momentum Particles in *pp* and Au + Au Collisions at $\sqrt{s_{NN}} = 200$ GeV. *Phys. Rev. Lett.*, 95:152301, Oct 2005.

[61] Thorsten Renk and Jörg Ruppert. Three-particle azimuthal correlations and mach shocks. *Phys. Rev. C*, 76:014908, Jul 2007.

[62] S. S. Adler et al. Dense-Medium Modifications to Jet-Induced Hadron Pair Distributions in Au + Au Collisions at $\sqrt{s_{NN}} = 200$ GeV. *Phys. Rev. Lett.*, 97:052301, Aug 2006.

[63] V.P. Konchakovski et al. Jet propagation through a hard string medium. *Phys. Rev. C*, 82, 2010.

[64] Tetsufumi Hirano. In-Plane Elliptic Flow of Resonance Particles in Relativistic Heavy-Ion Collisions. *Phys. Rev. Lett.*, 86:2754–2757, Mar 2001.

[65] N.N. Ajitanand, J.M. Alexander, P. Chung, W.G. Holzmann, M. Issah, et al. Decomposition of harmonic and jet contributions to particle-pair correlations at ultra-relativistic energies. *Phys.Rev.*, C72:011902, 2005.

[66] J. Adams et al. Azimuthal anisotropy and correlations at large transverse momenta in p+p and Au+Au collisions at $\sqrt{s_{NN}}$ = 200-GeV. *Phys. Rev. Lett.*, 93:252301, 2004.

[67] C. Lefevre. LHC: the guide. 2009.

[68] CMS Collaboration. Data Parking and Data Scouting at the CMS Experiment. 2012.

[69] CMS Collaboration. CMS Physics: Technical Design Report Volume 1: DetectorPerformance and Software. Technical Design Report CMS. CERN, Geneva. 2006.

[70] Tommaso Dorigo. Recent CMS Results. *EPJ Web Conf.*, 70:00021, 2014.

[71] Schematic of longitudinal view of CMS detector. . http://www.hephy.at/user/friedl/diss/html/img41.gif.

[72] Serguei Chatrchyan and others. Description and performance of track and primary-vertex reconstruction with the CMS tracker. *JINST*, 10:10009, 2014.

[73] S. Mrenna T. Sjostrand and P. Skands. PYTHIA 6.4 Physics and Manual. *JHEP*, 05:025, 2006.

[74] Kai Xiao, Feng Liu, and Fuqiang Wang. Event-plane decorrelation over pseudorapidity and its effect on azimuthal anisotropy measurements in relativistic heavy-ion collisions. *Phys. Rev. C*, 87:011901, 2013.

[75] Long-Gang Pang, Guang-You Qin, Victor Roy, Xin-Nian Wang, and Guo-Liang Ma. Longitudinal decorrelation of anisotropic flows in heavy-ion collisions at the CERN Large Hadron Collider. *Phys. Rev. C*, 91:044904, 2015.

[76] CMS Collaboration. Evidence for transverse momentum and pseudorapidity dependent event plane fluctuations in PbPb and pPb collisions. *Phys. Rev. C*, 92:034911, 2015.

[77] V. Skokov P. Bozek, A. Bzdak. The rapidity dependence of the average transverse momentum in p+Pb collisions at the LHC: the Color Glass Condensate versus hydrodynamics . *Phys. Lett. B*, 728:662, 2014.

[78] CMS Collaboration. Nuclear effects on the transverse momentum spectra of charged particles in pPb collisions at a nucleon-nucleon center-of-mass energy of 5.02 TeV. *Eur. Phys. J. C*, 75:237, 2015.

[79] M. M. Aggarwal et al. Azimuthal di-hadron correlations in d+ Au and Au + Au collisions at $\sqrt{s_{NN}}$ = 200 GeV measured at the STAR detector. *Phys. Rev. C*, 82:024912, Aug 2010.

[80] CMS Collaboration. Azimuthal anisotropy of charged particles at high transverse momenta in PbPb collisions at $\sqrt{s_{NN}}$ = 2.76 TeV. *Phys.Rev. Lett.*, 109:022301, 2012.

[81] Øystein Djuvsland and Joakim Nystrand. Single and double photonuclear excitations in Pb+Pb collisions at $\sqrt{s_{NN}} = 2.76$ TeV at the CERN Large Hadron Collider. *Phys. Rev. C*, 83:041901, Apr 2011.

VITA

VITA

Lingshan Xu graduated from Zhejiang University in July 2009 with a Bachelor of Science degree in Physics. She pursued her graduate study at Purdue University from 2009 to 2016. Lingshan Xu joined CMS experiment of Large Hadron Collider in 2012. She mainly worked on the collective flow and jet correlation measurements using particle correlation method in pPb and PbPb collisions.